N° D'ordre : 88.

Ecole Doctorale ''Sciences pour l'Ingénieur Microtechnique''

Université de Franche-Comté

Université de Technologie de Belfort-Montbéliard

THESE

Présentée pour obtenir le grade de

Docteur de l'Université de Technologie de Belfort-Montbéliard et de l'Université de Jiaotong de Xi'an en Sciences pour l'Ingénieur

Par

Chao ZHANG

Etude des la perméation de gaz et de la conductivité ionique des revêtements de zircone stabilisée à l'yttrium réalisés par projection plasma pour piles à combustible à oxyde solide (thèse en anglais)

Soutenue le 13 Juin 2008 devant le jury composé de :

Rapporteurs

Monsieur **G. CABOCHE**, Professeur, Université de Bourgogne.

Monsieur **G. MONTAVON**, Professeur, Université de Limoges.

Examinateurs

Monsieur **M. CASSIR,** Professeur, École Nationale Supérieure de Chimie de Paris.

Monsieur **C. CODDET**, Professeur, Université de Technologie de Belfort-Montbéliard.

Monsieur **C.-J. LI**, Professeur, Université de Jiaotong de Xi'an.

Monsieur **H. LIAO,** Professeur, Université de Technologie de Belfort-Montbéliard.

N° D'ordre : 88

Ecole Doctorale ''Sciences pour l'Ingénieur Microtechnique''

Université de Franche-Comté

Université de Technologie de Belfort-Montbéliard

THESE

Présentée pour obtenir le grade de

Docteur de l'Université de Technologie de Belfort-Montbéliard et de l'Université de Jiaotong de Xi'an en Sciences pour l'Ingénieur

Par

Chao ZHANG

Study on the gas permeation and ionic conductivity of plasma-sprayed yttria stabilized zirconia deposit for solid oxide fuel cells

Soutenue le 13 Juin 2008 devant le jury composé de :

Rapporteurs

Monsieur **G. CABOCHE**, Professeur, Université de Bourgogne.

Monsieur **G. MONTAVON**, Professeur, Université de Limoges.

Examinateurs

Monsieur **M. CASSIR,** Professeur, École Nationale Supérieure de Chimie de Paris.

Monsieur **C. CODDET**, Professeur, Université de Technologie de Belfort-Montbéliard.

Monsieur **C.-J. LI**, Professeur, Université de Jiaotong de Xi'an.

Monsieur **H. LIAO,** Professeur, Université de Technologie de Belfort-Montbéliard.

Acknowledgements

The work presented in this thesis has been made in *Labortroite d'Etudes et Recherches sur les Matériqux et les Propriétés de Surface* (LERMPS) of *Université de Technologie de Belfort-Mobtbéliard*(UTBM) and *Thermal Spray Laboratory*(TSL) of *Xi'an Jiaotong University*(XJTU) under the co-direction of *Prof. Hanlin Liao* and *Prof. Chang-Jiu Li*.

Prof. Christain Coddet, director of LERMPS is gratefully acknowledged for not only welcome me to his laboratory, but also for being a co-examiner of this thesis.

I wish to express my deep gratitude to my supervisors *Prof. Hanlin Liao* and *Prof. Chang-Jiu Li* for giving me the opportunity to realize this thesis as a co-tutor Ph.D. student in France and in China. They encouraged and supported me with much kindness throughout this work. By working with them, I learned a lot of scientific and legal knowledge, which are very important for my future projects. I am very grateful for the help that they made for me, not only technical guidance but also kind help in everyday life.

I would like also to thank the thesis committee members, *Prof. Ghislain Montavon, Prof. Gilles Caboche, Prof. Michel Cassir*, whose help, time and advice were indispensable for this work.

I would like to extend a special thanks to *Dr. Marie-Pierre Planche* and *Ms. Pascale Hoog* for their corrections of my manuscript.

Many group members, present and past have contributed greatly to my research efforts. Special thanks were given to *Dr. Cheng-Xin Li* and *Dr. Xian-Jin Ning* for their helpful suggestion throughout this endeavor. I wish to express my appreciation to my officemates, *Dr. Ga Zhang, who* provided useful advices in this thesis and gave many helps in everyday life. *Dr. Wen-Ya Li* and *Dr. Guan-Jun Yang* are also thanked for their suggestions in this work.

I also had the pleasure of becoming friends with *Xueping Guo, Wei Gao, Zhi-Guo Zhang, Olivier Marchand, Othmane Hatim, Yoann Danlos, Guillaume Douchy, Dimitry Sokolov* and many other colleagues during this period.

Lastly, my highest appreciation is addressed to my family and to *Xiaohui* who constantly listened carefully to all of my problems, who shared my sorrow, and who motivated me in all circumstances.

This thesis was supported by the co-tutors scholarship of French Government (Bourse du Gouvernement Français, N°:20042516).

Table of Contents

Chapter 3:
Electrical Property of Plasma-sprayed YSZ Electrolyte (as-sprayed and microwave sintered coating)

Chapter 4:
Gas Tightness of Plasma-sprayed YSZ Coating and Gas Permeation Behavior through Coating

Chapter 5:
Integrated Thermal Spraying Process and Electrical Performance of Tubular Solid Oxide Fuel Cells

Introduction

The desire to develop alternative energy sources, along with the ever-diminishing fossil fuel supply results in a present push for fuel cell technology. Fuel cells are direct chemical to electrical energy conversion devices that operate via an electrochemical reaction involving a fuel source (e.g. any hydrogen containing gas such as gasified coal and various hydrocarbons) and an oxygen source (e.g. oxygen and air).

Solid oxide fuel cell (SOFC) is one type of the fuel cell and known as ceramic fuel cells because its main components are made of ceramics which can eliminate corrosion or leakage problems common to the other liquid electrolyte fuel cells. SOFC operating temperatures are typically in the range of 800–1000°C. The high temperature leads to several advantages, such as internal reforming, the use of carbon monoxide as a fuel, the possibility of realizing combined heat and power plant solutions. Amongst the various fuel cell schemes, SOFC holds great promise of meeting the commercial needs.

At present, the commercialization efforts on SOFC systems are oriented to the cost reduction effort, in order to compete more effectively with other traditional power generating methods. In such a context, electrolyte deposition attracts particular attention. Plasma spraying process is a promising technique, providing such advantages as high deposition rate and easy masking for deposition of patterned structures, compared with other film formation processes. 8 mol% yttria doped zirconia (YSZ), is the most commonly used electrolyte material for its thermal stability, high ionic conductivity at elevated temperature and good thermal expansion compatibility with the other two electrodes materials. Low pressure plasma sprayed (LPPS) YSZ is more feasible for SOFC than atmospheric plasma sprayed (APS) YSZ. However, low costs of APS compared to LPPS makes it more competitive.

The main goal of the present work focuses on the measurement and understanding of the ionic conductivity and gas permeability of APS YSZ electrolyte as well as SOFC cell fabrication by thermal spraying processes.

Chapter 1 gives a review on SOFC component materials, especially electrolyte materials as well as the advanced process techniques. In particular, the main literature with regard to electrolyte layer deposited by plasma spraying is listed. Concerning plasma spraying, the main attention is focused on relatively low cost APS process. The perspective of plasma-sprayed electrolyte and the post treatment techniques on as-sprayed electrolyte coatings are also reviewed. All these information and discussions cumulate then in a summary of the aim of this thesis.

Chapter 2 presents the optimization process of APS spraying parameters via measuring in-flight particle characteristics versus particle size distribution. The influences of particle velocity and surface temperature on the microstructure of APS YSZ coating are studied. LPPS YSZ coatings and APS PSZ (4.5 mol% yttria stabilized zirconia) coatings are also deposited to make a comparison to APS YSZ coatings.

Chapter 3 is composed with two parts. In the first part, the ionic conductivity of APS YSZ coatings is measured and the features of ionic conductivity of plasma-sprayed coatings are studied. Then, the temperature dependence of ionic conductivity of YSZ coatings is observed and discussed. In the second part, microwave sintering is used to sinter the as-sprayed coatings. The modification of microstructure and ionic conductivity of APS YSZ coatings is investigated.

Chapter 4 evaluates the gas tightness of APS YSZ coatings via measuring coating gas permeability. The gas permeability of the APS YSZ coatings is estimated by oxygen, nitrogen or hydrogen. The effect of powder size, particle temperature and velocity on coating gas tightness is studied. Gas permeation behaviour through APS YSZ coatings is examined based on the gas permeation theory in porous materials. The bottle-neck to improve the tightness of APS coating is pointed out and a method to improve gas-tightness is proposed.

Chapter 5 shows the fabrication process of tubular Ni-YSZ/YSZ/LSM ($La_{0.8}Sr_{0.2}MnO_3$) solid oxide fuel cells prepared by the integrated thermal spray process. The as-sprayed cells are post-treated with a densification process to improve the gas-tightness of electrolyte and to enhance the performance of the cell. The output circuit voltage and power density of the cells are measured.

Chapter 1

SOFC Electrolyte and Plasma Spraying

This chapter gives a review on solid oxide fuel cell (SOFC) component materials, especially electrolyte materials as well as the advanced process techniques. In particular, the main literature with regard to electrolyte layer deposited by plasma spraying is listed. Concerning plasma spraying, the main attention is focused on low cost atmospheric plasma spraying. The perspective of plasma-sprayed electrolyte and the post treatment techniques on as-sprayed electrolyte coatings are also reviewed. All this information and discussions cumulate then in a summary of the aim of this thesis.

1.1 Introduction to Solid Oxide Fuel Cells (SOFC)

1.1.1 Principle of SOFC

Fuel cells provide an exciting option for the conversion of the chemical energy of fuel gas (e.g., hydrogen or natural gas) to electricity. The basic principle of a fuel cell is similar to those of the well-known electrochemical batteries, which are involved in many activities of everyday life. In the case of traditional batteries, the chemical energy is stored in substances located inside them and is limited. Concerning a fuel cell, a gaseous fuel (i.e., hydrogen) is continuously fed to the anode and an oxidant (i.e., oxygen from air) is continuously fed to the cathode. As long as the cell is fed with fuel and oxidant, electrical power can be provided.

Compared with conventional methods of power generation, fuel cells offer several advantages such as high conversion efficiency, modular construction, and much lower production of pollutants [1]. Amongst the various fuel cell schemes, solid oxide fuel cells (SOFCs) hold great promise of meeting the commercial needs, and have been extensity studied during the past years [2].

SOFCs are often known as ceramic fuel cells because their main components are made of ceramics which can eliminate corrosion or leakage problems common to the liquid electrolyte fuel cells. The SOFC consists of primarily three components: the cathode, the electrolyte and the anode besides the interconnector. At the cathode, oxygen molecules (O_2) from air are reduced to oxygen ions (O^{-2}) by accepting electrons.

$$O^2 + 4e^- \rightarrow 2O^{2-} \qquad (1)$$

Oxygen ions (O^{-2}) can transport through oxygen ionic conductive electrolyte, fully dense ceramic, toward the anode side where the fuel, usually hydrogen (H_2) or carbon

monoxide (CO) is oxidized to form water vapor (H_2O) or carbon dioxide (CO_2), and electrons are released.

$$2O^{2-} + 2H_2 \rightarrow 2H_2O + 4e^- \qquad (2)$$

$$2O^{2-} + 2CO \rightarrow 2CO_2 + 4e^- \qquad (3)$$

These electrons transport through the external circuit, generating electricity, and return back to the cathode thus completing the loop. The overall chemical reaction is carried out electrochemically without direct combustion.

$$2H_2 + O_2 \rightarrow 2H_2O \qquad (4)$$

$$2CO + O_2 \rightarrow 2CO_2 \qquad (5)$$

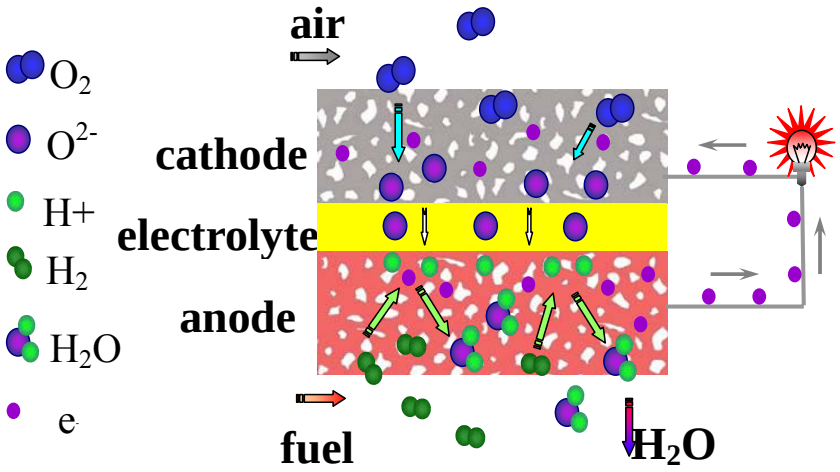

Figure 1 : a schematic principle of a SOFC with oxygen ion conductor as electrolyte.

The oxidation of H_2 to H_2O and CO to CO_2 is the mechanism of energy conversion of solid oxide fuel cell. Figure1 presents a schematic showing the principle of SOFC operation. According to the Nernst equation, the electromotive force of the single cell

could be calculated by:：

$$E_0 = -\Delta G/nF = (RT/nF)\ln P_{O_2}(c)/P_{O_2}(a) \qquad (6)$$

Where R is gas constant (8.314472 J/K mol)； T is absolute temperature； F is Faraday constant (96485.3415 s A/mol)； $p_{O_2(c)}$ is oxygen partial pressure of cathode； $p_{O_2(a)}$ is the oxygen partial pressure of anode. The electromotive force of the single cell is approximately 1 V, depending on temperature and oxygen pressure as showing by Eq.(6). In the practical operation, there is a voltage loss caused by different polarizations including Ohmic resistances. The voltage loss is called over-voltage. It is important to decrease the over-voltage in order to enhance the efficiency and output power density of the cell.

Beside a feature of all-solid-structure, the SOFCs are viable for generating electricity from hydrocarbon fuels. The operation at a high operating temperature from 600 to 1000°C allows the internal reforming, promotes rapid kinetics with non-precious materials, and produces high quality by-product heat for cogeneration. On the other hand, the high operation temperature of the SOFC places stringent requirements on its materials. The development of suitable low-cost materials and low-cost fabrication process for ceramic structures is presently the key technical challenge facing SOFCs commercialization.

1.1.2 Structure of SOFC

As aforementioned, the voltage obtained from a single cell is about 1V. Therefore, it is necessary to arrange the cells in series and parallel to each other in order to obtain the voltage and output power suitable for commercial use. SOFCs have greater flexibility in its cell design compared to other type of fuel cells because the components are all solid. Today, many developers have proposed various cell designs. Here, some typical cell designs are introduced.

(1) Tubular-type

The tubular cell was first developed by the American electric company, Westinghouse Electronic Corporation (present Siemens-Westinghouse Power Corporation) [2]

Figure 2(a) shows a scheme of a single cell. This type of cell has several advantages such as easy-sealing and high mechanical strength due to its structure. On the other hand, the current flow in the lateral direction at the electrode causes a large Ohmic loss. In order to reduce the internal losses and increase the power density, new cell geometries, e.g., High Power Density (HPD) tubes are also under development to replace the classic tubes as shown in Figure 2(b) [2].

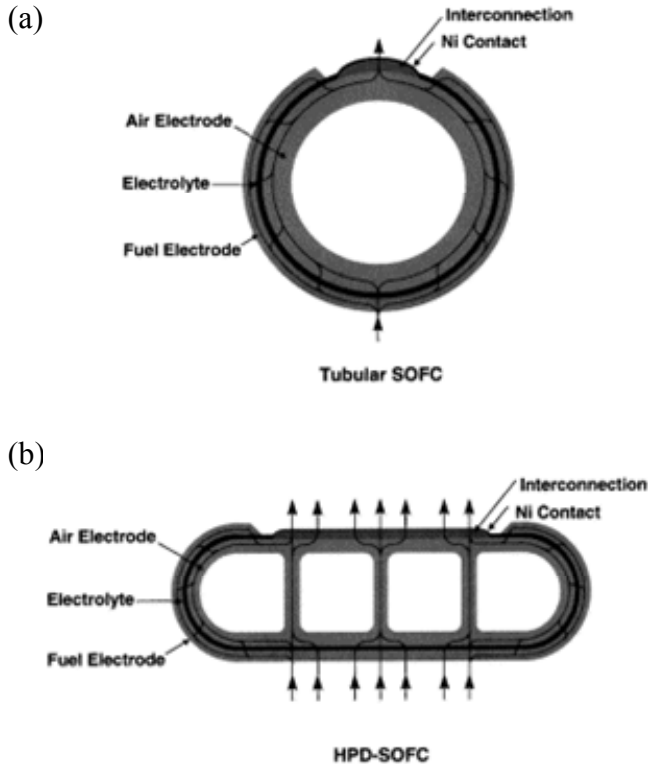

Figure 2: a comparison of the current path in a tubular cell (a) and in an HPD-cell (b) [2].

Another example of tubular-type cell is the transverse stripe type tubular cell, which was developed by Mitsubishi Heavy Industries Ltd. (MHI). It is schematically shown in Figure 3 [3]. In this type of cell, single cells are arranged in series on one tube. Therefore, each tube can be regarded as a small stack.

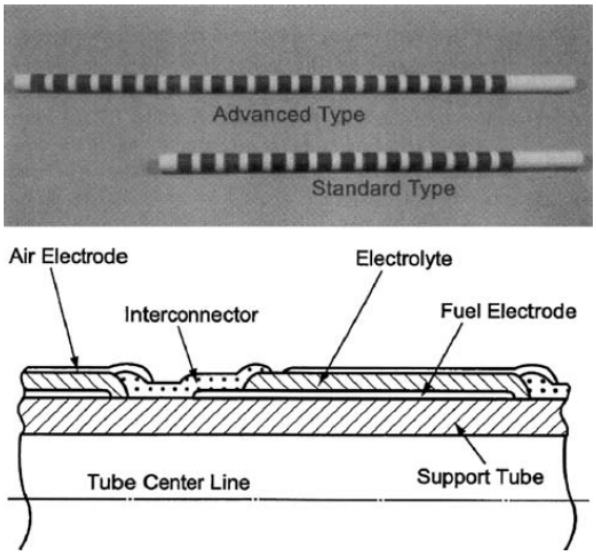

Figure 3: photograph and scheme of transverse stripe type tubular cell [3].

(2) Planar-type

There are several kinds of planar-type cells. Figure 4 shows a single cell, which consists of porous cathode, dense electrolyte and porous anode, and a dense interconnector. The merits of the planar-type cell are the relative ease in controlling Ohm loss by changing the thickness of materials, flexibility in the shape of the cell, and easy-manufacturing.

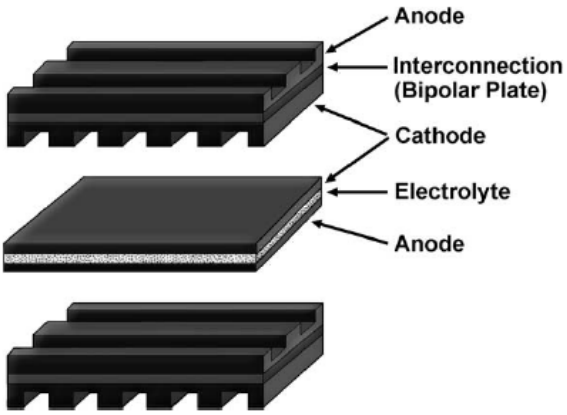

Figure 4: schematic of the planar design [4].

However, the problems with this type of design are as follows:

1. The temperature becomes nonuniform, which causes thermal stress and eventually the mechanical breakdown of the cell. The thermal coefficient mismatch between different components in the stack, which causes the thermal stress, becomes severe with the increase in the cell's numbers integrated in the stack.
2. It is difficult to seal the cell operating at high temperature.
3. There is relatively high contact resistance between cells.
4. It is necessary to have high mechanical strength because the cell at the bottom of the stack has to support the weight of the stacked cells.

1.1.3 SOFC Materials

SOFC main components include the anode, the cathode and the electrolyte. Fuel cell stacks contain an interconnector which links individual cells together in series or parallel.

(1) Electrolyte Materials

SOFC electrolyte should have the following characteristics: thermodynamic stability from room temperature to working temperature; chemical stability in both reducing and oxidizing atmospheres; high ionic conductivity and low electronic conductivity. In addition to these properties, the followings are also important: sufficient mechanical strength, chemical compatibility with electrode materials and matching of the thermal expansion coefficient with electrode materials. Of course, low cost of raw materials, ease in processing, low toxicity and sufficient quantity of natural resources are important in the practical context. The latter three requirements are also valid for electrode and interconnector materials described in the following sections.

Fluorite-structured oxide materials such as yttria or scandium stabilized zirconia, rare earth doped ceria, and rare earth doped bismuth oxide have been widely investigated as electrolytes for a solid oxide fuel cell [5]. Among these materials, yttria stabilized zirconia has been most successfully employed [6,7,8]. The yttria dopant serves dual roles: it stabilizes the high temperature cubic phase in zirconia and also generates oxygen

vacancies through the defect reaction. The conductivity increases with increasing dopant concentration up to a maximum value at 8 mol% and then decreases sharply. A more detailed introduction of yttria stabilized zirconia will be given in the following section.

Similarly to ZrO_2 based electrolyte, Ceria based electrolyte were also widely investigated. In the case of ceria, the doping of Samarium (Sm) [9] and gadolinium (Gd) [10] give the highest values of ionic conductivity when dopant concentrations are 10-20%. The strong dependence of ionic conductivity on dopant type and concentration has been explained in terms of the lattice distortions introduced by the dopant, with those that produce the least amount of strain causing the smallest variation in the potential energy landscape. Overall, the ionic conductivity of ceria is approximately an order of magnitude greater than that of stabilized zirconia for comparable doping conditions. This is a result of the larger ionic radius of Ce^{4+} (0.87 Å) than Zr^{4+} (0.72 Å), which produces a more open structure through which oxygen ions can easily migrate. Despite its favorable ion transport properties, ceria had not, until quite recently, been considered as a realistic candidate for SOFC applications because of its high electronic conductivity.

The ABO_3 perovskite structure has appeared as a high conductivity candidate electrolyte material in the past ten years. A large variety and concentration of dopants can be accommodated in a wide range of host compounds. Introduction of divalent dopant ions, typically Sr and Mg, onto the La and Ga sites, respectively, produces a material with a high concentration of mobile oxygen vacancies and thereby high oxygen ionic conductivity. The conductivity of the particular composition $La_{0.9}Sr_{0.1}Ga_{0.8}Mg_{0.2}O_{3-\delta}$ (LSGM) was reported [11,12]. The conduction is entirely ionic over an extremely wide oxygen partial pressure range at temperatures as high as 1000 °C, but its conductivity is not as high as that of suitably doped ceria. However, the long term stability due to Ga-evaporation in a reducing atmosphere as well as the compatibility to Ni (NiO) seems to be a severe problem at high operating temperatures. The use of LSGM-electrolyte-substrate contains problems due to the low mechanical stability of LSGM and the high costs of gallium. To avoid the reaction of LSGM and Ni,

(non-reactive) ceria buffer layers was incorporated between the electrolyte and the anode [13]. Nevertheless, intensive research efforts to develop SOFCs incorporating lanthanum gallate continue, and recent work suggests that the ionic conductivity can be increased by further adjustments to the stoichiometry, in particular, via the addition of small concentrations of Ni or Co [14].

The ion transport properties of bismuth oxide have received significant academic attention as a result of a rather spectacular phase transition at about 700°C which leads to an increase in conductivity by almost three orders of magnitude [15, 16]. The key limitations of bismuth based compounds are their very high electronic conductivities, and tendencies to become reduced to bismuth metal in hydrogen or fuel containing atmospheres.

(2) Anode Materials

SOFC anode materials should satisfy the following characteristics: thermodynamic stability from room temperature to working temperature; stability in the operating atmosphere at working temperature; high electronic conductivity; high electrocatalytic activity for the electrode reaction and sufficient mechanical strength.

The reducing conditions presenting on the fuel side permit the use of a metal such as nickel (alternately cobalt or ruthenium) as the anode. However, the thermal expansion of nickel is considerably larger than that of YSZ. Nickel can also sinter at the cell operating temperature resulting in a decrease of the anode porosity. These problems are usually circumvented by forming a skeleton of YSZ around the nickel particles. The YSZ skeleton prevents the nickel particles from sintering, decreases the anode thermal expansion coefficient bringing it closer to that of the electrolyte, and provides a better adhesion of the anode with the electrolyte. In addition to YSZ, the electrochemically active layer may also contain doped ceria for a better ionic conductivity and improve kinetics of the anode reaction. Samarium-doped ceria (SDC) is one of the most promising materials as an oxygen conductor in a SOFC anode because SDC has a high ionic conductivity larger

than 3×10^{-2} S/cm at 700^{o}C depending on samarium composition. SDC also has oxidation-catalytic properties and might exert high anodic activities due to rapid electrochemical oxidation of hydrocarbon gas. Therefore, cermets composed of Ni and SDC would be one of the most promising candidates as an intermediate temperature (IT) SOFC anode.

The micro or nano-structure can enlarge contact areas between Ni and oxygen conductor and suppress the Ni sintering. Nickel (Nickel oxide)/ YSZ (SDC) composite anode layer with nano microstructure were deposited using different process techniques, e.g. spray pyrolysis [17], plasma spraying [18], aerosol flame deposition [19], etc..

(3) Cathode Materials

SOFC cathode should meet the following requirements: thermodynamic stability from room temperature to working temperature; high electronic conductivity; high electrocatalytic activity for the electrode reaction and sufficient mechanical strength.

The most commonly used cathode material is lanthanum manganite ($LaMnO_3$), a p-type perovskite. Typically, it is doped with rare earth elements (e.g., Sr, Ce, Pr) to enhance its conductivity. Most often it is doped with strontium and referred to LSM ($La_{1-x}Sr_xMnO_3$). The conduction of these perovskites is all electronic (no ionic conductivity). The fabrication process of LSM depends on cell design. For example, in the tubular cell developed by Siemens Westinghouse Ltd., the cell was constructed by extruding a cathode tube and building the rest of the cell on it. At some research groups, where planar cell designs are being investigated, the cathode was fabricated by screen printing or tape casting techniques using nanoscale particles [20,21]. In both cases, the challenge is to sinter the cathode adequately, often by co-sintering with the other components, while maintaining sufficient interconnected porosity.

At high temperature, YSZ was often incorporated to LSM to form an YSZ/LSM composite cathode functional layer between YSZ electrolyte and conventional LSM cathode. For reduced-temperature SOFCs, the reduction of the system operating

temperature requires cathode materials with high electrochemically catalytic activity for oxygen reduction. The oxygen reduction rates of conventional LSM cathodes are significantly reduced below 800^{o}C, YSZ was also adopted to form composite layer to enhance the cathode vacancy concentration [22]. The search for new cathode material focused on related transition metal perovskites, in which a variable valence element resides at the octahedral site. It has been known lanthanum cobaltites have higher electronic conductivities than lanthanum manganites [21], but they are not suitable for YSZ based SOFCs because they become reduced at very high temperature. At reduced temperatures and significant Fe incorporation, they show excellent promise. In particular, $La_{1-x}Sr_xCo_{1-y}Fe_yO_{3-\delta}$ (LSCF) has emerged as a viable candidate. Recently, $Sm_{0.5}Sr_{0.5}CoO_3$ and its composite were also reported to exhibit excellent cathode activity [23,24,25]. As these various materials are developed, chemical and thermomechanical compatibility of cathode materials with the electrolyte will require attention.

(4) Interconnection Materials

An interconnection material can be either a metallic or ceramic layer that sits between each individual cell. For both the planar and the tubular cell configuration, the role of interconnection is literally two folds: (1) providing electrical connection between anode of an individual cell to the cathode of neighboring one; (2) acting as a physical barrier to protect the air cathode material from the reducing environment of the fuel on the anode side, and equally to prevent the anode material from contacting with oxidizing atmosphere of the cathode side [26]. Obviously, the interconnection is required to have the features of thermodynamic stability in both reducing and oxidizing atmospheres at working temperature, high electronic and low ionic conductivities. Moreover, interconnection should display low gas permeability to minimize the direct combination of oxidant and fuel during cell operation. Being exposed to both the oxidizing and reducing atmosphere at the high temperature, it must be extremely stable. For this reason, ceramics have been more successful than metals in the long term operation as interconnection materials for high temperature SOFCs. However, these ceramic interconnection materials are extremely

expensive. Doped lanthanum chromite is usually used as the interconnection material. Lanthanum chromite is a p-type conductor and its conduction is due to small polaron hopping from room temperature to 1400°C at an oxygen pressure as low as 10^{-18} atm. [27]. The conductivity is enhanced as lower valence ions (e.g. Ca, Mg, Sr, etc.) are substituted on either the La^{3+} or the Cr^{3+} sites. For the Siemens Westinghouse tubular SOFC, the doped lanthanum chromite interconnection is deposited in the form of an about 85-μm thick, 9-mm wide strip along the air electrode tube length direction by plasma spraying [28].

Inexpensive metallic materials are becoming more promising for reduced temperature (600-800°C) SOFCs. Chromium-based alloys [29], are favored as interconnection materials owing to their moderate oxidation resistance and fairly good corrosion resistance. More importantly, Cr_2O_3 have comparatively low electrical resistivity at elevated temperatures among metal oxides. Another attractive feature of chromium-based alloys as the interconnector is that they possess a thermal expansion coefficient close to that of ceramic component (e.g., YSZ) in SOFC. Although the metallic interconnector offers many advantages over their ceramic counterparts, high growth rate of oxide and easy volatilization are the two main drawbacks of metallic interconnector. Therefore, the currently developed chromium-bearing metallic interconnectors can only be applied to SOFC operating at a temperature lower than 700°C. In the past several years, iron-based alloys were developed to use as interconnection materials. As compared to chromium-based alloys, iron-based alloys are attractive in terms of high ductility, good workability and low cost. Presently, iron-chromia-based alloys are being explored for possible applications as interconnection materials in SOFC, because of its relatively low CTE. [30].

1.2 Yttria-stabilized Zirconia Electrolyte

1.2.1 Properties

As aforementioned, today, most advanced SOFCs employ zirconia-based electrolyte,

specifically yttria-stabilized zirconia as the electrolyte, nickel/ stabilized zirconia cermet as the anode, strontium doped lanthanum manganite (LSM) as the cathode, and doped lanthanum chromite for the interconnector. The ionic conductivity of yttria stabilized zirconia requires that the operating temperature remains from 800 to 1000^{o}C.

Zirconia (ZrO_2) is a well-known polymorphic material and has three different crystal structures. At room temperature the structure of zirconia is monoclinic (*m*), it transforms to tetragonal (*t*) at temperature of 1170^{o}C, and then to cubic (c) at 2370^{o}C. At cooling process, such transformations are reversed. The *t* to *m* transformation is accompanied with a large volume change of about 3% to 5% with constriction while heating and expansion upon cooling. The large volume change has made it impossible to produce ceramics parts from pure zirconia. However, this effect can be delayed or eliminated by doping the zirconia with lower valency oxide such CaO, MgO, or Y_2O_3. The doping allows for a desired structure to be maintained at a temperature range from room temperature to high temperature, hence named as stabilized zirconia. Depending on the amount of dopant the *t* or *c* phase can be obtained. Solid solutions containing 2-6% of yttria retain the tetragonal structure (partially stabilized zirconia, and was referred to PSZ in this thesis) and have excellent mechanical properties. Increasing the yttria concentration to around 8-10% will stabilize the zirconia to the cubic structure, which is referred to as fully stabilized zirconia (YSZ is referred to 8 mol.% yttria stabilized zirconia in this thesis).

YSZ is widely used as electrolyte because of high ionic conductivity (about 0.14-0.18 S cm^{-1} at 1000°C) and stability under oxidizing and reducing atmosphere [31,32]. The doping of ZrO_2 with Y_2O_3 results in the substitution incorporation of Y^{3+} on the Zr^{4+} cation sublattice with the concomitant formation of oxygen vacancies as charge compensating defects. The defect formation reaction can be written in Kroger and Vink notation as:

$$Y_2O_3 + 2Zr_{Zr}^{\times} + O_o^{\times} \longrightarrow 2Y_{Zr}^{'} + V_o^{\bullet\bullet} + 2ZrO_2 \qquad (6)$$

The high oxygen ionic conductivity in YSZ is attributed to these oxygen vacancies.

The ionic conductivity is independent of oxygen partial pressure under different temperatures, implying that the ionic transport is nearly uniform. The thermal expansion coefficient of YSZ bulk is about $10\times10^{-6}/\ ^{o}C$ [32], which is similar to those of the other SOFC cell components. For the optimization of SOFC performance, the YSZ electrolyte must be free of porosity so as not to allow gases to permeate from one side of the electrolyte to the other.

1.2.2 Process Technique

Solid oxide fuel cells based on YSZ have been developed for high operating temperature ranging from 900 to 1000°C. The operation at such high operating temperature is advantageous as it is beneficial for the internal reforming of fuels such as natural gas, rapid electrocatalysis without precious metals, and produces high quality byproduct (heat) for cogeneration. However, traditionally YSZ electrolyte-supported solid oxide fuel cell has a thick YSZ electrolyte and has a large Ohmic resistance, which will reduce the cell output performance. The electrolyte resistance (i.e., Ohmic losses across the electrolyte) should be minimized by decreasing the electrolyte thickness or with alternative materials of higher ionic conductivity. Although it has been proposed elsewhere that ScSZ (more expensive than YSZ) [33,34] exhibits a high oxygen ion conductivity to be useful as electrolytes in high temperature SOFCs, the low cost fabrication techniques of YSZ thin electrolyte layer are still important for the development of commercial SOFCs.

YSZ electrolyte layer can be fabricated by different routes [35] to make thin electrolyte layer. Electrochemical Vapor Deposition (EVD) is a well developed method to fabricate YSZ coating. EVD is a modified Chemical Vapor Deposition (CVD) process, originally developed by Westinghouse Ltd [36]. In the EVD process, a porous ceramic substrate divides a reactor into two chambers, of which one is filled with a metal compound reactant and the other with an oxygen source reactant. Firstly, the pore will be closed by a normal CVD type reaction between the reactant metal chloride vapors and water vapor (or oxygen). Film grows due to the presence of an electrochemical potential

gradient across the deposited film. Then, oxygen ions formed on the water vapor side of the substrate diffuse through the thin metal oxide layer to the metal chloride side. The oxygen ions react with the metal resulted from chloride vapors to form the metal oxide product.

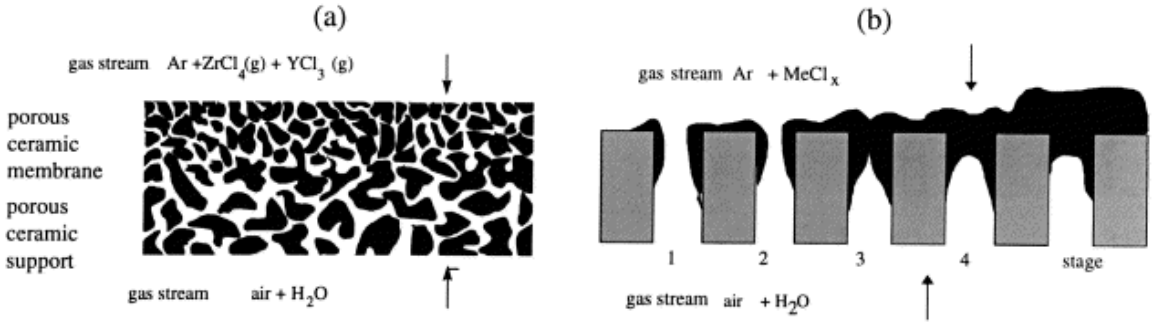

Figure 5: (a) a scheme of the basic principles of the CVD/EVD processes. (b) detailed view of the different stages during the CVD/EVD processes in which the solid product is mainly deposited at the chloride side [35].

A schematic diagram of the basic principles of the CVD/EVD process is given in Figure 5. A tubular SOFC with a zirconia-based electrolyte layer deposited by EVD process has exhibited superior output performance [37]. Although EVD is a well developed technique for depositing uniform and gas tight layers of YSZ and interconnection materials, there are some disadvantages. The shortcomings of EVD process are the high reaction temperature, the presence of corrosive gases, the high cost and relatively low deposition rates. Many traditionally wet ceramic processes, such as tape casting, screen printing, and co-sintering techniques have also been extensively used for preparing YSZ electrolytes. Although satisfactory results with SOFC prepared with the techniques have been obtained at high temperatures (>950°C) [38,39], the large scale fabrication of components still remained as a major problem due to cell cost. Traditional wet ceramic techniques face several problems that included but are not limited to the following items [40]:

(1) multiple separate equipment, such as an extruder or tape-caster, screen-printer, and one or more furnaces are required for the multiple steps of the wet ceramic technique;

(2) high-temperature firing leads to a substantial and rapid increase in capital costs;

(3) size enlargement of single cells to more than 15 cm × 15 cm creates serious problems resulting from large total shrinkage or thermal expansion coefficient mismatch strain, often leading to macro-cracks, severe warping, or cell fracture during high-temperature firing steps;

(4) high-temperature firing steps lead to inter-reactions between adjacent cell layers.

Some review articles on process techniques of SOFC electrolyte have been given. More details about the processes were introduced in these papers [35,41,42].

As aforementioned, the commercialization efforts on SOFC systems are oriented to the cost reduction effort, in order to compete more effectively with other traditional power generating methods [43]. In such a context, reducing the fabrication cost of the electrolyte layer is a critical challenge for the commercialization of SOFCs [2]. Some pre-commercialization SOFC stacks are also successfully developed by Siemens-Westinghouse Ltd with EVD technique. However, the high cost of EVD or wet-ceramic process makes SOFC difficult to be an available new energy conversion system. Plasma spraying is proposed as a lower cost alternative for producing the electrolyte layer due to its relatively high deposition efficiency, relatively low cost and easy automation.

1.3 Electrolyte Fabricated by Plasma Spraying

Plasma spraying is a thermal spraying method, which is a material processing technique for producing coatings and free-standing parts using a plasma jet. Plasma Spray is the most flexible of all the thermal spray processes as it can develop sufficient energy to melt any materials which exhibit a congruent melting behavior. Figure 6 shows the key components of an atmospheric plasma spray system. Figure 7 shows the schematic

cross-section of a typical mono-cathode plasma spray gun. A high frequency arc is ignited between an anode (nozzle) and a cathode. Process gases (generally mixtures of argon and hydrogen) flowing between two electrodes is partially ionized to become a plume of hot plasma gas with the temperature of 6 600 °C to 16 600 °C (12 000 °F to 30 000 °F) [44]. When the feedstock material is injected into the gas plume, it is melted and simultaneously propelled towards the target substrate.

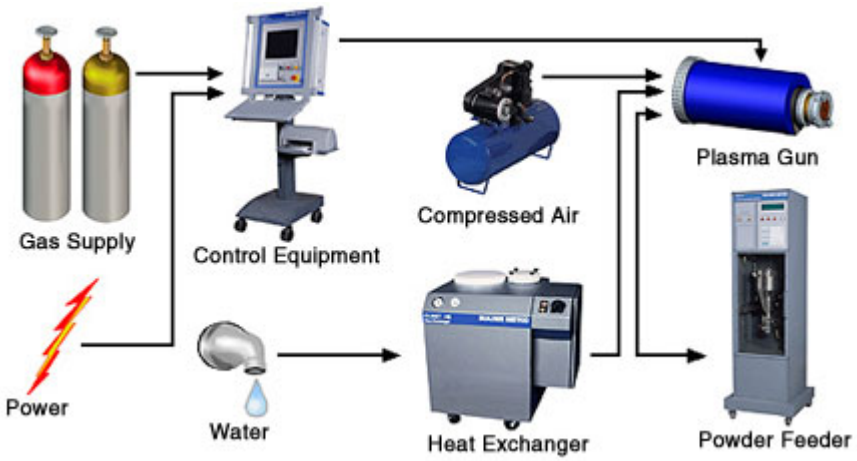

Figure 6: Key components of atmospheric plasma spray system [44].

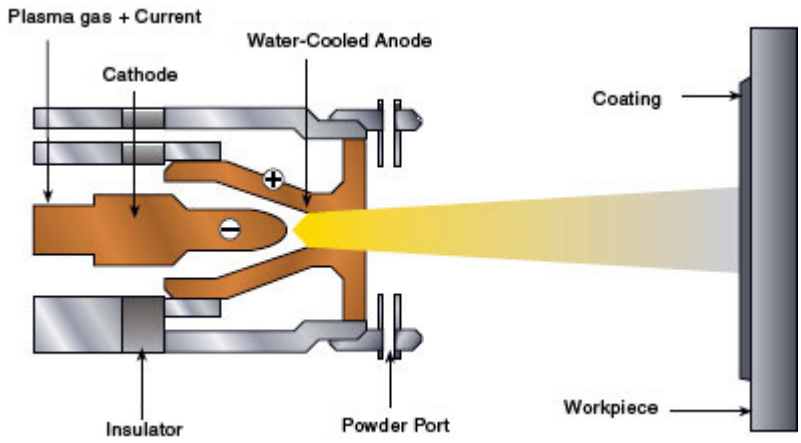

Figure 7: Schematic cross-section of a typical plasma spray gun [44].

The processes gases, in combination with the arc current applied to the electrode control the amount of energy produced by the process. Since the flow of each of the gases

and the applied current can be accurately regulated, repeatable and predictable coating results can be obtained. In addition, the point and angle that the material is injected into the plume, as well as spraying distance (distance of the gun to the target), can also be controlled. This provides a high degree of flexibility to develop appropriate spray parameters for materials with melting temperatures across a very large range.

During spraying, the material to be deposited - typically as a powder, sometimes as a liquid, suspension - is introduced into the plasma jet, emanating from a plasma torch. In the plasma jet, where the temperature is in the order of 10000K, the material is melted and propelled towards a substrate. There, the molten droplets flatten, rapidly solidify and form lamellae, the stacking of which forms a deposit, as shown in Figure 8. There are many technological parameters that influence the interaction of the particles with the plasma jet and the substrate and therefore the deposit properties. These parameters include feedstock type, plasma gas composition and flow rate, arc current, spraying distance, substrate cooling, etc [45].

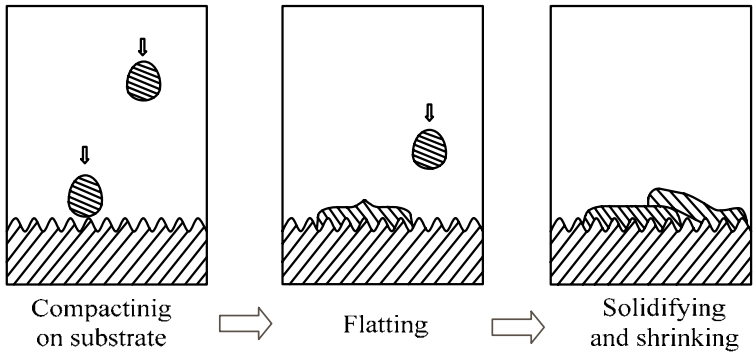

Figure 8: Formation of plasma-sprayed coating [46].

The resulting coatings consist of a multitude of pancake-like lamellae called 'splats', formed by the flattening of liquid droplets. As the feedstock powders typically have sizes from 5 micrometers to about 100 micrometers, the lamellae have a thickness in the micrometer range. Between these lamellae, there are small voids, such as pores, cracks and no bonding interface between lamellae. As a result of this structure, the deposits have properties significantly different from bulk materials. The general features of deposit

mechanical properties compared with the identical bulk counterparts are lower strength and apparent Young's modulus, higher strain tolerance, and lower thermal conductivity [45].

1.3.1 Low Pressure Plasma Spraying

Low pressure plasma spraying (LPPS), also known as vacuum plasma spraying (VPS) is a variation of plasma spraying, which is carried out in an inert gas atmosphere, at a reduced pressure chamber. Figure 9 shows a typical plasma spray system. The spray gun is operated in a chamber within a completely controlled atmospheric environment. Chamber spraying may be used to prevent contamination of the coating material and/or substrate, or because a reaction of the coating material with a specifically introduced substance is desired. Due to the low pressures as low as 20-200 mbar used, the velocity of plasma jet increases and the plasma jet plume became less turbulent in LPPS and particle velocity reduction from nozzle to substrate is less pronounced, but the energy density of plasma is lowered. Generally, the LPPS in-flight particles have higher velocities than those in APS.

As a result, thin-films produced by LPPS typically possess higher density than those manufactured by atmospheric plasma spraying, and exhibit a better substrate adhesion. Hence, LPPS is successfully used for fabricating SOFC electrolytes, where high density, small thickness are primary requirements. Some SOFC cell configurations are developed using LPPS process. Considerable progress has been made on metallic substrate supported planar SOFCs, particularly at the German Aerospace Center (DLR) [47,48,49,50,51]. The DLR has co-operated with various sectors in automotive companies on SOFC development.

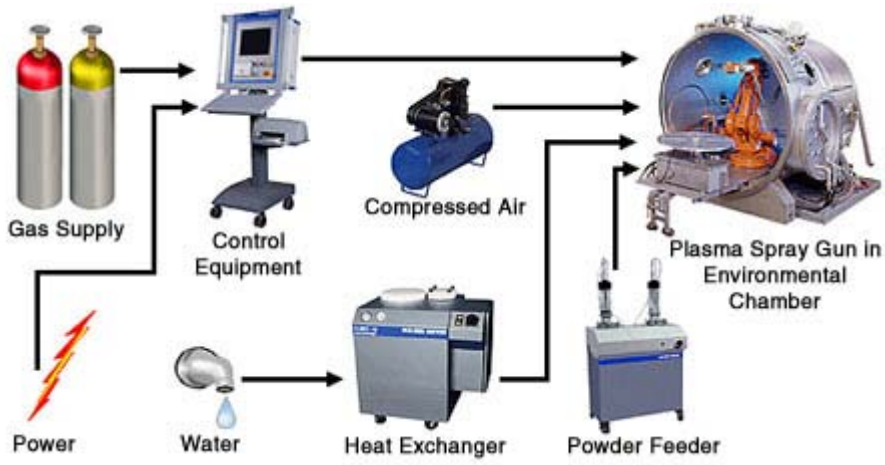

Figure 9: Schematic cross-section of a typical plasma spray gun [45]

As well as to SOFC electrolyte layer, it could be successfully deposited by LPPS process. As inherent features of plasma-sprayed ceramic coatings, there also exist two major concerns in LPPS SOFC electrolyte: anisotropic properties and gas tightness. Strong anisotropy in the ionic conductivity of YSZ fabricated by LPPS process was observed by Van Herle et al. [52]. The ionic conductivities along parallel direction to the deposit surface were several times higher than that along perpendicular direction. On other hand, gas tightness is another primary requirement for the electrolyte used in SOFC, whereas LPPS electrolyte thin films are often incompletely dense.

An advanced plasma torch with a Laval-like nozzle providing a controlled expansion of the plasma jet has been developed at DLR [47]. The new torches can generate a plasma jet with higher velocity under low pressure conditions, which reduces the interaction of melt particles with the surrounding cold gas, thus improving spray conditions. In-flight particles velocities up to 900 m/s with this torch can be achieved [47], which was much higher than the particle velocity of traditional LPPS. Porosity in the range of 1.5-2.5 % was achieved in YSZ layers with a thickness in the range of 30 μm. Figure 10Figure illustrates a typical cross-sectional view of a single cell fabricated from LPPS process [48]. Such thin electrolytes were found to reduce significantly Ohmic resistance of the cell and could be used in reduced temperature SOFC. In DLR's cell, power densities of 500-600 mW/cm^2 at operating temperatures of 800°C have been achieved [47]. Although

presenting some problems, LPPS is of substantial interest in the manufacture of low weight, small volume and low cost SOFC for such applications as auxiliary power units, through the improvement of the materials development and process optimization. The merits offered by LPPS clearly outweigh its drawbacks compared to conventional process. However, capital and operating cost was still too expensive to make large-scale commercialization. Creating vacuum conditions prior to every deposition run and during spraying vacuuming a high-gas flow rate make this batch processing technique less favorable economically. For continuous processing to be achieved, even higher capital investments of pre-vacuum chambers must be installed [51].

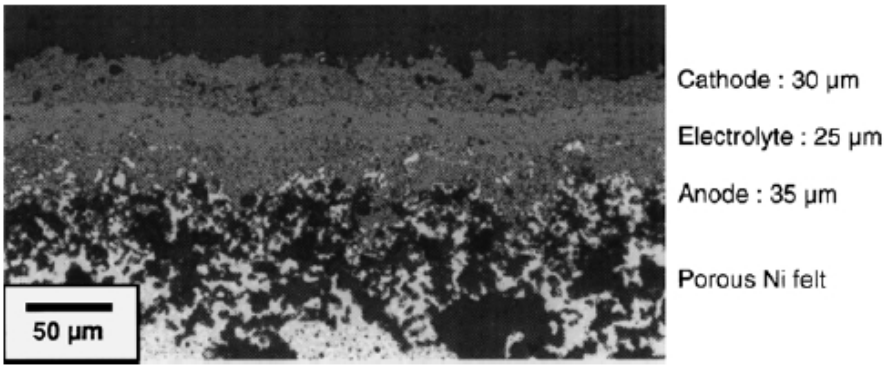

Figure10: SOFC layers deposited on porous metallic substrates by LPPS process [48].

1.3.2 Liquid Plasma Spraying

In the past decade, the technique of liquid plasma spraying was developed to elaborate ceramic materials and fabricate desired ceramic coatings. In liquid plasma spraying, a liquid by the means of a solution or slurry is employed as a feedstock for plasma spraying.

(1) Solution Precursor Plasma Spraying (SPPS)

In SPPS process, the feedstock is a solution containing a metal precursor, such as nitrates, isopropoxides, butoxides, dissolved in a solvent such as ethanol, isopropanol, n-butanol [53]. The solution is generally injected by the means of gas atomization (droplet average size ranging from 20 to 60 µm) [53]. The heat and momentum transfers from the

plasma to these droplets have been modeled [54]. A mechanism has been proposed by Jordan et al. [55] which is depicted in Figure 11. The resulting coatings present relatively dense zones corresponding to the droplets heated in the warm regions of the plasma jet and porous ones probably related to particles treated in cold regions of the plasma jet. The coating pore level and its microstructure can be controlled by the process parameters such as the power, the spray distance, the plasma gases property and their flow rate, and the solution injection parameters. Stabilized zirconia coatings have been well investigated with zirconium and yttrium precursors in an aqueous solution for thermal barrier coating by Inframat Corporation and University of Connecticut (USA) [56,57,58,59,60,61]. SPPS coatings have some unique micro-structural features compared to conventional plasma spraying [58,60], including: (1) ultra fine splats, (2) nanometer and micrometer-sized interconnected porosity, and (3) closely spaced, through-thickness cracks.

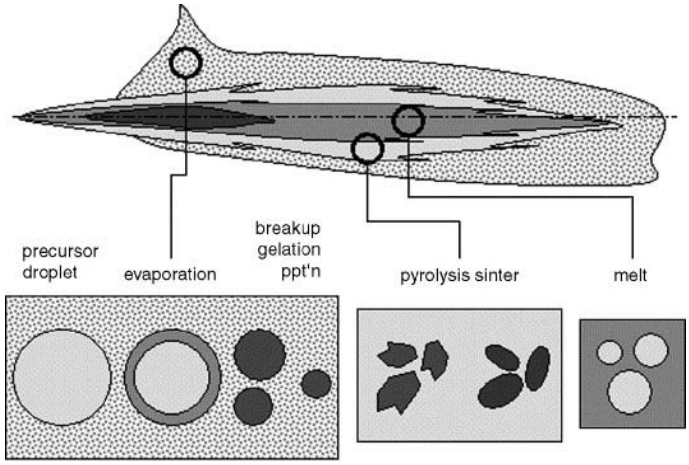

Figure 11: Schematic illustration showing the multiple paths for material being deposited by solution precursor plasma spraying [55].

It seems that the SPPS is a suitable method for depositing thermal barrier coatings (TBCs). The specific micro-structural features of SPPS TBCs provide high thermal cycling life and a bond strength compared to that fabricated by conventional routes. The microstructure of SPPS coating prevents it from being used as a SOFC electrolyte and there are no literatures reported on SPPS electrolyte coating up to now.

(2) Suspension/slurry Plasma Spraying (SPS)

In suspension plasma spraying, the suspension allows the feeding of particles with diameters ranging from several nanometers to 10 micrometers into the plasma plume, which is almost impossible in the traditional plasma spraying processes. With such suspension, the liquid has to be evaporated in the first step within the plasma jet before the melting of the solid particles takes place. The suspension viscosity, the particle size distribution and morphology, the spray distance and the plasma operating torch are the most important parameters to control coating microstructure [62]. Moreover, it is of great importance to optimize the suspension atomization and injection in suspension plasma spraying [63]. The coating microstructure also depends on the particle trajectories and the corresponding velocities upon impact. Regarding the fact that small particles decelerate very fast [64] during spraying, spray distances of suspension plasma spraying vary between 30 and 60 mm, which is much shorter than the conventional plasma spraying from 100 to 150 mm generally.

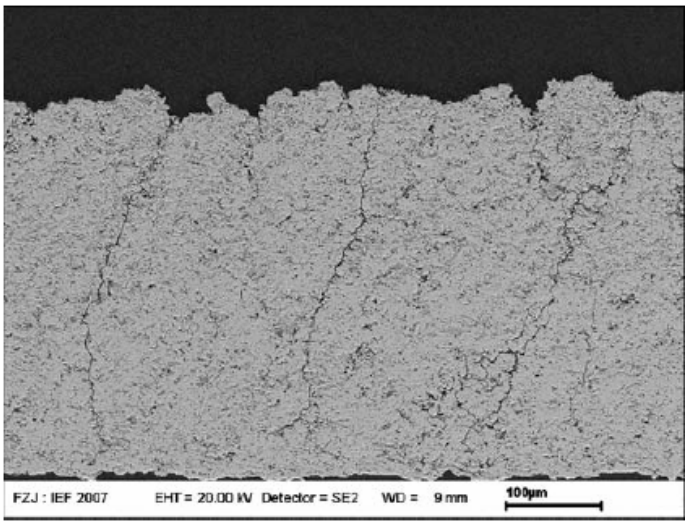

Figure 12: Cross section of suspension plasma-sprayed YSZ coating [65].

In the suspension plasma-sprayed coatings, pores are often generated by poorly treated particles traveling in the jet fringes. Another phenomenon must be taken into consideration is that the relatively short spraying distance results in heat fluxes transmitted to substrate and pre-deposited coating. Such a high flux can modify locally

the micro-structures corresponding to sintered coatings and results in high density of segmentation cracks, as depicted in Figure 12 [65].

Some investigation is attempted to fabricate different SOFC components with suspension plasma spraying process, e.g., anode [66], electrolyte [67,68,69], cathode [70]. With regards to YSZ electrolyte coatings, the suspension plasma spraying uses sub-micron particles with a much lower size than that in conventional spraying processes, the resulted splat size and the splat thickness is much smaller. The different microstructures between suspension plasma spraying and conventional atmospheric plasma spraying coatings are depicted in Figure 13, which shows a high porosity (about 20%) in suspension plasma spraying coating [71]. Moreover, there are more segmentation cracks in the SPS coating due to a short standoff distance. The combination of high segmentation cracks and small and thin splats in SPS coating is ideal for an application as thermal barrier coating as it allows a good thermal insulation due to the high porosity and a strain tolerance [71].

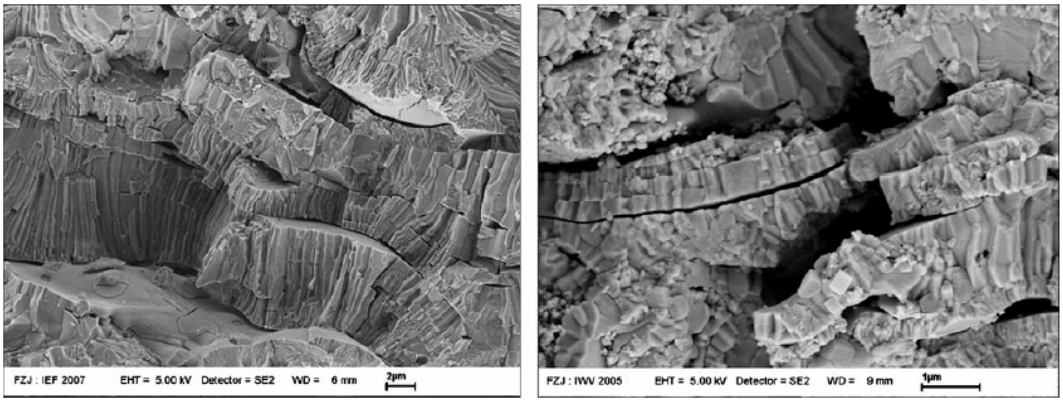

Figure 13: Fractal micro-structure of an APS coating (left) and a SPS coating (right) [65].

1.3.3 Atmospheric Plasma Spraying (APS)

Compared with the LPPS process, APS process does not need nor sophisticated apparatus or controlled atmosphere, which would decrease the fabrication cost of electrolyte layer. Moreover, without using controlled vacuum chamber promises fast cell production with potential automated lines. Therefore, APS has been employed as YSZ

electrolyte fabrication process by leading SOFC developer, Siemens-Westinghouse Power Co. [2], and other enterprises and research institutes [72,73,74,75,76,77,78].

With the aims of making improved electrolytes, the main results achieved by APS together with the post treatment techniques were reviewed.

According to the literature [37], APS was already considered as an electrolyte manufacturing technology in Siemens-Westinghouse Power Co.. APS was expected to replace the former expensive EVD and LPPS process to decrease the cost of the electrolyte. However, at this stage, a post-spray sintering is required for APS electrolyte to get the necessary gas-tightness. Stacks of such tubes are preferably assigned to stationary system in the power range of about 100 to more than 1000 kW. APS was also adopted by Mitsubishi Heavy Industries Ltd. (MHI) where on the 20 mm diameter zirconia support tube with multiple cells were deposited, each comprising the anode, the electrolyte and the cathode [79,80] which was demonstrated in section 1.1.2.

Besides these two main enterprises, there are some other institutes devoted to develop improved SOFC electrolyte by atmospheric plasma spraying. It has been reported [74], a gas tightness and thinner electrolyte layer was prepared by atmospheric plasma spraying-sintering process. A tubular single cell with a 60 μm electrolyte, using porous lanthanun doped manganite as substrates, was successfully fabricated by thermal spraying-sintering process. As a result of an operating test using O_2 and humidified H_2 at 1000°C, a power density of 0.73 W/cm^2 was obtained [74]. It was demonstrated that the thermal spraying-sintering technology is effective for the fabrication of a thin gas tight layer for SOFCs. An intermediate temperature SOFC (IT-SOFC) based on 80 μm YSZ electrolyte, $La_{0.6}Sr_{0.4}CoO_{3-\delta}$ (LSCo) cathode and Ni-YSZ anode coating were consecutively deposited on a porous Ni-plate substrate by APS process. The output power density of the sprayed cell achieved 260 mW/cm^2 at 800°C [75]. In the work of Stöver et al. [81], a Triplex II plasma spraying gun was used to produce thin (<=40 μm) YSZ layers on tape-casted ferritic steel sheet substrates. The anode was also sprayed by APS using a separate injection of NiO and YSZ powder. Electrochemical performance was measured

after applying a LSCF cathode layer by wet-chemical method. The values of the measured open circuit voltage (OCV) were 0.95V and the power density was 500 mW/cm^2 at 800°C. Although these progresses were achieved by APS process, the attention should be paid to the OCV of these cells. According to the theory calculation, the theoretical OCV of the cells was about 1.1V at 800 °C, which was much higher than obtained OCV in the above literature. This fact means that the electrolyte deposited by APS process was not sufficiently gas-tight. As a matter of fact, many researchers have noticed this problem and some post treatments were proposed.

1.3.4 Pre and Post-spray Techniques of As-sprayed Coating

Plasma-sprayed coating is formed by a stream of molten droplets impacting on the substrate. The individual molten droplets spread to thin lamella. The stacking of lamellae constitutes the coating. A plasma-sprayed coating is generally of lamellar structure. Pores are always present in the obtained coating. A fraction of voids from several percent up to 20% can be formed in the deposit [82]. Some of voids result from insufficient filling and incomplete wetting of molten liquid to previously formed rough deposit surfaces. The microcracks can be formed easily in the splat of ceramic materials because of quenching stress that occurs in the splats. Such microcracks are also a kind of void that appears in the deposits and constitutes a fraction of porosity. The voids in the deposits can generally be divided into three types on the basis of the dimension of voids, i.e., three dimensional type, two-dimensional type, and micro-cracks in ceramic deposits [83]. Three-dimensional type voids are similar in morphology to those in the materials processed by powder metallurgical method, and coarse voids in a size from sub-micrometer to more than 10 micrometer. Two-dimensional type voids correspond to the inter-lamellar gap (non-bonded interface between lamellae), and are in the sub-micrometer dimension at direction perpendicular to splat plane, but they are in the size comparable with the size of splat in the other two directions. Therefore, such voids present typically the "coin"-shape morphology. The third type void was the vertical cracks in the individual flattened lamellae, which was also called intra-lamella crack, due to the quenching stress that

occurs in the splats.

Because of the numerous coarse pores, inter-lamellae gaps and intra-lamellae cracks introduced to the YSZ electrolyte by plasma spray process, the electrolyte is not sufficiently gas tight and consequently the OCV and energy conversion efficiency of the subsequent cell is severely curtailed. Porosity in plasma-sprayed YSZ electrolyte exists in two levels. Pores ranging from 1 to 10 μm that arise from entrapped gas, unmelted particles, cracking or premature solidification by some particles, while pores in a size less than 0.5 μm are formed as a result of non-bonded interface and vertical cracks in individual lamellae [84,85]. The latter type of pore is rather predominant in plasma-spayed YSZ electrolyte coating, and it causes pores in the electrolyte to be inter-connected, which is the main factor that lowers the cell OCV by allowing the reacting gases to pass through the electrolyte. Also, poor contact amongst the lamellae decrease the mechanical and electrical property of the electrolyte, and cause increase of Ohmic polarization. In order to improve the performance of the cell, effective post treatment methods were proposed to bring the as-sprayed YSZ electrolyte to a higher performance.

In order to get a dense microstructure, the APS as-sprayed YSZ coatings were heated by a post sintering process. Small amounts of transition metal oxides were added to the feedstock for plasma spraying in order to reduce the sintering temperature of as-sprayed coating [71,74]. It is demonstrated in the last section 1.3.3 that the post sintering technology is effective for the fabrication of a single cell with a high power density. Khor et al. reported a success spark plasma sintering method to densify APS YSZ coating [77]. With this method, it could be possible to transform the lamellar structure of as-sprayed coating to a granular microstructure in only 3 minutes. The value of porosity could be changed from 10% to above 1%.

In the work of Li et al. [78,86,87], a successful chemical solution densification was developed for APS YSZ electrolytes by repeated infiltration of the zirconium and yttrium nitrate solutions followed by a baking process at 400°C for complete decomposition of the

nitrates. After densification, the results revealed a significant effect of densification on gas permeability. The measurement of the test cell revealed that the open circuit voltage (OCV) equal to the theoretical value can even be achieved through the post densification [78], which implies that the connected pores in the deposit can be effectively filled out. However, the electrical conductivity of post-treated coating was improved by only about 25% compared with that of as-sprayed coatings. The TEM microstructure of YSZ coating microstructure revealed that the YSZ resulting form the decomposition of nitrate mainly exists in non-bonded interface, but not in vertical cracks of splat. The non-bonded interface area was evenly filled by nano-porous YSZ decomposed by nitrate and the only isolated nano-pores were distributed in those areas. The low gas permeability of the densified APS coatings could be attributed to YSZ in the non-bonded interface which broke the interconnected pore in the as-sprayed coating. On the other hand, the nano-porous microstructure of the YSZ brings out the high contact resistance and limits the improvement of the ionic conductivity.

As well known, due to the fact that the surface temperature of the previously deposited splat upon which the subsequent molten droplets spread cannot be significantly increased by the spreading melt, and the wetting of the spreading melt to the splat surface is insufficient to create chemical bonding at the interface, it is difficult to improve the bonding ratio between the lamellae and to improve the electrical performance of plasma-sprayed ceramic coating. The short heating duration in plasma means that most particles attain a temperature of around the melting point of the materials involved [88]. Then it is believable that the splat surface temperature can be increased significantly by keeping the substrate at a high temperature during deposition. In this way it may be possible to increase the lamellar interface bonding. In the last year, some interesting research works have been conducted on this subject [89,90]. In the work of Xing et al. [89], prior to spraying, the substrates were pre-heated to a high temperature (about 800°C) by a flame spray torch and kept at high temperature during spraying. In such conditions, the columnar grains can grow continuously from underlying splat surface, which was not the same to the lamella structure of the conventional APS as-sprayed coating. This

microstructure change led to significant improvements of the ionic conductivity of plasma-sprayed YSZ coating, which could be comparable to that of the sintered coating. In the mean time, Vaßen et al. [90] applied this method to fabricate YSZ electrolytes for metal supported SOFCs. The cells with YSZ electrolyte deposited under pre-heated condition show an OCV above 1V and an output density of 500 mW/cm^2 at 800°C. The use of metallic rather than ceramic substrates makes it favorable to avoid cracks for the electrolyte deposition on high temperature substrate.

1.4 Objective of the Thesis

The discussions above clearly indicate that research on low cost fabrication of SOFC electrolyte is still a major as well as a challenging area in the field of solid oxide fuel cells. Plasma spraying, especially APS, is a promising means to prepare low cost and high performance YSZ electrolyte. However, the APS as-sprayed YSZ electrolyte was blamed for its inherent coating microstructure. The APS YSZ coating shows anisotropic electrical properties and insufficient gas tightness, which was not favorable for SOFC operation. In particular, the spraying parameters on the plasma-sprayed electrolyte performance demands special attention, since there was no system study in the literature and was not clearly understood. This is mainly due to the complicated plasma spraying process where there are many factors influencing the coating microstructure. In this study, a diagnostatic analyzer was used to investigate the influence of in-flight particle features (particle temperature, velocity and size) on coating microstructure and ionic conductivity. The electrical and gas-tightness performance of plasma-sprayed YSZ electrolyte was deeply studied as they are two important aspects to determine the performance of YSZ electrolyte in SOFC operation. The main goal of the present work focuses on the characterization and understanding of the ionic conductivity and gas permeability of plasma-sprayed YSZ electrolyte as well as SOFC cell fabrication by thermal spray processes.

1.5 References

[1]K. Trimble and R. Woods, Fuel cell applications and market opportunities, *J. Power Sources* **29**(1-2) (1990), p. 37-45.

[2] S.C. Singhal, Advances in solid oxide fuel cell technology, *Solid State Ionics*, **135**(1-4) (2000), p. 305-313.

[3] H. Tsukuda, A. Notomi and N. Hisatome. Application of plasma spraying to tubular-type solid oxide fuel cells production. J. Therm. Spray Technol., 9 (2000), p. 364-368.

[4] S.C. Singhal, Solid oxide fuel cells for stationary, mobile, and military applications, *Solid State Ionics*, **152-153** (2002), p. 405-410.

[5] R.M. Dell and A. Hooper. In: P. Hagenmuller and W. Van Gool (Eds.), Solid Electrolytes, Academic Press, New York, 1978, p. 291.

[6] P.H. Hofmann, A. Schweiger, L. Fryda, K.D. Panopoulos, U. Hohenwarter, J.D. Bentzen, J.P. Ouweltjes, J. Ahrenfeldt, U. Henriksen and E. Kakaras, High temperature electrolyte supported Ni-GDC/YSZ/LSM SOFC operation on two-stage Viking gasifier product gas, *J. Power Sources*, **173**(1) (2007), p. 357-366.

[7] Y. Du, N. M. Sammes and G. A. Tompsett, Optimisation parameters for the extrusion of thin YSZ tubes for SOFC electrolytes, *J. Euro. Ceram. Soc.*, **20**(7) (2000), p. 959-965.

[8] S.-G. Kim, S.P. Yoon, S.W. Nam, S.-H. Hyun and S.-A. Hong, Fabrication and characterization of a YSZ/YDC composite electrolyte by a sol-gel coating method, *J. Power Sources*, **110**(1) (2002), p. 222-228.

[9] K. Eguchi, T. Setoguchi, T. Inoue and H. Arai, Electrical properties of ceria-based oxides and their application to solid oxide fuel cells, *Solid State Ionics*, **52**(1-3) (1992), p. 165-172.

[10] B.C.H. Steele. Appraisal of $Ce_{1-y}Gd_yO_{2-y/2}$ electrolytes for IT-SOFC operation at 500°C, *Solid State Ionics*, **129**(1-4) (2000), p. 95-110.

[11] T. Ishihara, H. Matsuda and Y. Takita, Doped LaGaO3 perovskite type oxide as a new oxide ionic conductor, *J. Am. Chem. Soc.*, **116**(9) (1994) p. 3801-3803.

[12] M. Feng and J.B. Goodenough, A superior oxide ion electrolyte, *Eur. J. Solid State Inorg. Chem.*, **31**(1994), p. 663-672.

[13] K.Q. Huang, J.H. Wan and J.B. Goodenough, Increasing Power Density of LSGM-Based Solid Oxide Fuel Cells Using New Anode Materials, *J. Electrochem. Soc.*, **A148** (2001), p.788-794.

[14] T. Ishihara, T. Shibayama, H. Nishiguchi, Y. Takita, Oxide ion conductivity in $La_{0.8}Sr_{0.2}Ga_{0.8}Mg_{0.2-X}Ni_XO_3$ perovskite oxide and application for the electrolyte of solid oxide fuel cells, *J. Mater. Sci.*, **36**(5) (2001), p. 1125-1131.

[15] Sammes NM, Tompsett GA, Nafe H, Aldinger F, Bismuth based oxide electrolytes-structure and ionic conductivity, *J. Eur. Ceram. Soc.*, **19**(10) (1999), p. 1801-1826.

[16] Shuk P, Weimhofer HD, Gush U, Gopel W and Greenblatt M, Oxide ion conducting solid electrolytes based on Bi_2O_3, *Solid State Ionics*, **89**(3-4) (1996), p.179-196.

[17] S. Sudaw and K. Kawahara, Preparation of Matrix-Type Nickel Oxide/Samarium-Doped Ceria Composite Particles by Spray Pyrolysis, *J. Am. Ceram. Soc.*, **90**(4) (2007), p. 1094-1100.

[18] C. Hwang and C.-H. Yu, Formation of nanostructured YSZ/Ni anode with pore channels by plasma spraying, *Surf. Coat. Technol.*, **201**(12) (2007), p. 5954-5959.

[19] Y.S. Yoon, J.M. Im and D.W. Shin, Microstructure and electrical conductivity of NiO–YSZ nano-powder synthesized by aerosol flame deposition, *Ceram. Int.*, 2007 (In Press).

[20] D. Rotureau, J.-P. Viricelle, C. Pijolat, N. Caillol and M. Pijolat, Development of a planar SOFC device using screen-printing technology, *J. Euro. Ceram. Soc.*, **25**(12) (2005), p. 2633-2636.

[21] D. Montinaro, V.M. Sglavo, M. Bertoldi, T. Zandonella, A. Aricò, M. Lo Faro and V. Antonucci, Tape casting fabrication and co-sintering of solid oxide "half cells" with a cathode–electrolyte porous interface, *Solid State Ionics*, **177**(19-25) (2006), p. 2093-2097.

[22] B.C.H. Steele, K.M. Hori, S. Uchino, Kinetic Parameters Influencing the Performance of IT-SOFC Composite Electrodes, Solid State Ionics, **135** (2000), p. 445-450.

[23] C. Xia, W. Rauch, F. Chen and M. Liu, $Sm_{0.5}Sr_{0.5}CoO_3$ cathodes for low-temperature SOFCs, *Solid State Ionics*, **149**(1-2) (2002), p. 11-19.

[24] S.M. Choi, K.T. Lee, S. Kim, M.C. Chun and H.L. Lee, Oxygen ion conductivity and cell performance of $La_{0.9}Ba_{0.1}Ga_{1-x}Mg_xO_{3-\delta}$ electrolyte, *Solid State Ionics*, **131**(3-4) (2000), p. 221-228.

[25] Y. Liu, W. Rauch, S. Zha and M. Liu, Fabrication of $Sm_{0.5}Sr_{0.5}CoO_{3-\delta}$-$Sm_{0.1}Ce_{0.9}O_{2-\delta}$ cathodes for solid oxide fuel cells using combustion CVD, *Solid State Ionics*, **166**(3-4) (2004), p. 261-268.

[26] W. Z. Zhu and S. C. Deevi, Development of interconnect materials for solid oxide fuel cells, *Mater. Sci. Eng. A*, **348**(1-2) (2003), p. 227-243.

[27] T. Nakamura, G. Petzow and L.J. Gauckler, Stability of the perovskite phase $LaBO_3$ (B=V, Cr, Mn, Fe, Co, Ni) in reducing atmosphere: I. Experimental results. *Mater. Res. Bull.*, **14**(5) (1979), p. 649–659.

[28] L.J.H. Kuo, S.D. Vora and S.C. Singhal, Plasma spraying of lanthanum chromite films for solid oxide fuel cell interconnection application, *J. Am. Ceram. Soc.*, 80(3) (1997), p. 589-593.

[29] Z. Yang, G.-G. Xia and J.W. Stevenson, Evaluation of Ni–Cr-base alloys for SOFC interconnect applications, *J. Power Sources*, **160**(2) (2006), p. 1104-1110.

[30]T. Brylewski, M. Nanko, T. Maruyama and K. Przybylski, Application of Fe–16Cr ferritic alloy to interconnector for a solid oxide fuel cell, Solid State Ionics, **143**(2) (2001), p.131-150.

[31]. Yamamoto, Solid Oxide Fuel Cells: Fundamental aspects and prospects, *Electrochim. Acta,* 45(2000), p 2423-2435.

[32]. E. Ivers-Tiffee, A. Weber, and D. Herbstritt, Materials and technologies for SOFC-components, *J. Eur. Ceram. Soc.*, **21**(2001), p 1805-1811.

[33] F. Tietz, W. Fischer, Th. Hauber and G. Mariottoc, Structural evolution of Sc-containing zirconia electrolytes, *Solid State Ionics*, **100**(3-4) (1997), p. 289-295.

[34] Y. Mizutani, M. Kawai and Y. Nakamur, O. Yamamoto, Y. Aratia, Y. Takedaa, N. Imanishia, Electrical conductivity of stabilized zirconia with ytterbia and scandia, *Solid State Ionics*, **79** (1995), p. 137-142.

[35] J. Will, A. Mitterdorfer, C. Kleinlogel, D. Perednis and L. J. Gauckler, Fabrication of thin electrolytes for second-generation solid oxide fuel cells, *Solid State Ionics*, **131**(1-2) (2000), p. 79-96.

[36] U. B. Pal and S. C. Singhal, Electrochemical vapor deposition of yttria-stabilized zirconia films, *J. Electrochem. Soc.*, **137**(9) (1990), p. 2937-2941.

[37] M.C. Williams, J.P. Strakey and S.C. Singhal, U.S. distributed generation fuel cell program, *J. Power Sources*, **131**(1-2) (2004), p. 79-85.

[38] P. Timakul, S. Jinawath and P. Aungkavattana, Fabrication of electrolyte materials for solid oxide fuel cells by tape-casting, *Ceram. Int.*, (In Press) 2007.

[39] D. Rotureau, J.-P. Viricelle, C. Pijolat, N. Caillol and M. Pijolat, Development of a planar SOFC device using screen-printing technology, *J. Eur. Ceram. Soc.*, **25**(12) (2005), p. 2633-2636.

[40] R. Hui, Z. Wang, O. Kesler, L. Rose, J. Jankovic, S. Yick, R. Maric and D. Ghosh, Thermal plasma spraying for SOFCs: Applications, potential advantages, and challenges, *J. Power Sources*, **170**(2) (2007), p. 308-323.

[41] N.Q. Minh. Solid oxide fuel cell technology-features and applications, *Solid State Ionics*, **174**(1-4) (2004), p. 271-277.

[42] L.R. Pederson, P. Singh and X.-D. Zhou, Application of vacuum deposition methods to solid oxide fuel cells, *Vacuum*, **80**(10) (2006), p. 1066-1083.

[43] B.C.H. Steele, Materials science and engineering: The enabling technology for the commercialisation of fuel cell systems. *J. Mater. Sci.*, **36** (2001), p. 1053-1068.

[44] http://www.sulzermetco.com/desktopdefault.aspx/tabid-1741//3381_read-5289.

[45] Mcpherson R. A review of microstructure and properties of plasma sprayed ceramic coatings, *Surf. Coat. Technol.*, **39-40** (1989), p. 173-181.

[46] W.-Z. Wang, Quantitative characterization of lamellar microstructure of plasma sprayed coatings and relationship between lamellar microstructure and properties of coatings, Ph. D. Thesis, Xi'an Jiaotong University, 2004, p. 14 (In Chinese).

[47] G. Schiller, R. Henne, M. Lang, R. Ruckdaschel and S. Schaper, Development of vacuum plasma sprayed thin-film SOFC for reduced operating temperature, *Fuel Cell Bull.* **3** (2000), p. 7-12.

[48] M. Lang, T. Franco, G. Schiller and N. Wagner, Electrochemical characterisation of

vacuum plasma sprayed thin-film solid oxide fuel cells (SOFC) for reduced operating temperatures, *J. Appl. Electrochem.*, **32**(8) (2002), p. 871–874.

[49] G. Schiller, R. Henne and R. Ruckdaschel, Selective area laser deposition (SALD) joining of monolithic silicon carbide structures using dual lasers, *J. Adv. Mater.*, **32** (2000), p. 3-8.

[50] M. Lang, A. Dresel, T. Franco, Z. Ilhan, A. Nestle and G. Schiller, High temperature tensile Testing Method for Monofilament Ceramic Fibers, *Ceram. Eng. Sci. Proc.*, **26** (2005), p. 67–74.

[51] M. Lang, R. Henne, S. Schaper and G. Schiller, Development and characterization of vacuum plasma sprayed thin film SOFC, *J. Therm. Spray Technol.*, **10**(4) (2001), pp. 618-625.

[52] J. Van Herle, A.J. McEvoy and K.R. Thampi, Conductivity measurements of various yttria-stabilized zirconia samples, *J. Mater. Sci.* **29**(14) (1994), p. 3691-3701.

[53] P. Fauchais, G. Montavon, M. Vardelle and J. Cedelle, Developments in direct current plasma spraying, *Surf. Coat. Technol.*, **201**(5) (2006), p. 1908-1921.

[54] A. Ozturk and B. M. Cetegen, Modeling of plasma assisted formation of precipitates in zirconium containing liquid precursor droplets, *Mater. Sci. Eng. A*, **384**(1-2) (2004), p. 331-351.

[55] E.H. Jordan, L. Xie, X. Ma, M. Gell, N.P. Padture, B.M. Cetegen, A. Ozturk, J. Roth, T.D. Xiao and P.E.L. Bryant, Superior thermal barrier coatings using solution precursor plasma spray, *J. Therm. Spray Technol.*, **13**(1) (2004), p. 57-65.

[56] L. Xie, E.H. Jordan, N.P. Padture and M. Gell, Phase and microstructural stability of solution precursor plasma sprayed thermal barrier coatings, *Mater. Sci. Eng. A*, **381**(1-2) (2004), p. 189-195.

[57] M. Gell, L. Xie, X. Ma, E.H. Jordan and N.P. Padture, Highly durable thermal barrier coatings made by the solution precursor plasma spray process, *Surf. Coat. Technol.*, **177-178** (2004), p. 97-102.

[58] X.Q. Ma, T.D. Xiao, J. Roth, L.D. Xie, E.H. Jordan, N.P. Padture and M. Gell In: D. von Hofe, Editor, Thick TBCs with Controlled Microstructure Using Solution Precursor Plasma Spray Process, *Thermal Spray 2004: Advances in Technology and Applications*, ASM International, Materials Park, 2004, p. 1103-1109.

[59] F. Wu, E.H. Jordan, X. Ma and M. Gell, Thermally grown oxide growth behavior and spallation lives of solution precursor plasma spray thermal barrier coatings, *Surf. Coat. Technol.*, **202**(9) (2008), p. 1628-1635.

[60] X.Q. Ma, F. Wu, J. Roth, M. Gell and E.H. Jordan, Low thermal conductivity thermal barrier coating deposited by the solution plasma spray process, *Surf. Coat. Technol.*, **201**(7) (2006), p. 4447-4452.

[61] A. Jadhav, N.P. Padture, F. Wu, E.H. Jordan and M. Gell, Thick ceramic thermal barrier coatings with high durability deposited using solution-precursor plasma spray, *Mater. Sci. Eng. A*, **405**(1-2) (2005), p. 313-320.

[62] K. Wittmann, F. Blein, J.F. Coudert and P. Fauchais, Control of the injection of an alumina suspension containing nanograins in a DC-plasma, *New Surfaces for a New*

Millennium, C.C. Berndt, K.A. Khor and E. Lugscheider, Ed., ASM International, 2001, p. 375-382.

[63] J. Oberste Berghaus, S. Bouaricha, J.-G. Legoux, and C. Moreau, Injection Conditions and In-Flight States in Suspension Plasma Spraying of Alumina and Zirconia Nano-Ceramics, *Thermal Spray 2005: Explore its Surface Potential!*, E. Lugscheider, Ed., May 2-4, 2005 (Basel, Switzerland), ASM International, 2005, p. 512-518.

[64] P. Fauchais, V. Rat; C. Delbos; J.F. Coudert, T. Chartier and L. Bianchi, Understanding of suspension DC plasma spraying of finely structured coatings for SOFC, *IEEE Trans. Plasma Sci.*, **33**(2) (2005), p. 920-930.

[65] H. Kassner, R. Siegert, D. Hathiramani, R. Vassen, and D. Stöever, Application of suspension plasma spraying (SPS) for manufacture of ceramic coatings, *J. Therm. Spray Technol.* **17**(1) (2008), p. 115-123.

[66] Z. Wang, J.O. Berghaus, S. Yick, C. Decès-Petit, W. Qu, R. Hui, R. Maric and D. Ghosh, Dynamic evaluation of low-temperature metal-supported solid oxide fuel cell oriented to auxiliary power units, *J. Power Sources*, **176**(1) (2008), p. 90-95.

[67] R. Rampon, F.L. Toma, G. Betrand, C. Coddet, Liquid plasma sprayed coatings of yttria-stabilized zirconia for SOFC electrolytes, *J. Therm. Spray Technol.* **15**(4) (2006), p. 682-688.

[68] R. Rampon, C. Filiatre, G. Bertrand, Suspension plasma spraying of YPSZ coatings: suspension atomization and injection, *J. Therm. Spray Technol.* **17**(1) (2007) p. 105-114.

[69] M. Bonneau, F. Gitzhofer, and M. Boulos, SOFC/CeO2 Doped Electrolyte Deposition, Using Suspension Plasma Spraying, *Thermal Spray 2000: Surface Engineering via Applied Research*, C.C. Berndt, Ed., ASM International, Materials Park, OH, USA, 2000, p. 929-934.

[70] C. Monterrubio-Badillo, H. Ageorges, T. Chartier, J.F. Coudert and P. Fauchais. Preparation of $LaMnO_3$ perovskite thin films by suspension plasma spraying for SOFC cathodes, *Surf. Coat. Technol.* **200**(12-13) (2006), p. 3743-3756.

[71] R. Henne, Solid oxide fuel cells: a challenge for plasma deposition processes, *J. Therm. Spray Technol.* **16**(3) (2007), p. 381-483.

[72] C.-J. Li, C.-X. Li, Y.-Z. Xing, M. Gao and G.-J. Yang, Influence of YSZ electrolyte thickness on the characteristics of plasma-sprayed cermet supported tubular SOFC, *Solid State Ionics*, **177**(19-25) (2006), p. 2065-2069.

[73] Shunji Takenoiri, Naruaki Kadokawa and Kazuo Koseki, Development of Metallic Substrate Supported Planar Solid Oxide Fuel Cells Fabricated by Atmospheric Plasma Spraying. *J. Therm. Spray Technol.*, **9**(3) (2000), p. 360-363.

[74] K. Okumura, Y. Aihara, S. Ito and S. Kawasaki, Development of Thermal Spraying-Sintering Technology for Solid Oxide Fuel Cells, *J. Therm. Spray Technol.*, **9**(3) (2000) 354-359.

[75] R. Zheng, X.M. Zhou, S.R. Wang, T.-L. Wen, C.X. Ding, A study of Ni + 8YSZ/8YSZ/ $La_{0.6}Sr_{0.4}CoO_{3-\alpha}$ ITSOFC fabricated by atmospheric plasma spraying, *J. Power Sources*, **140**(2) (2005), p. 217-225.

[76] R. Vaßen, D. Hathiramani, J. Mertens, V.A.C. Haanappel and I.C. Vinke, Manufacturing of high performance solid oxide fuel cells (SOFCs) with atmospheric plasma spraying (APS), *Surf. Coat. Technol.*, **202**(3) (2007), p. 499-508.

[77] K.A. Khor, L.-G. Yu, S.H. Chan and X.J. Chen, Densification of plasma sprayed YSZ electrolytes by spark plasma sintering (SPS), *J. Eur. Ceram. Soc.*, **23**(11) (2003), p.1855-1863.

[78]C.-J. Li, X.-J. Ning, C.-X. Li, Effect of densification processes on the properties of plasma-sprayed YSZ electrolyte coatings for solid oxide fuel cells, *Surf. Coat. Technol.*, **190** (2005), p. 60-64.

[79] H. Tsukuda, A. Notomi and N. Hisatome. Application of plasma spraying to tubular-type solid oxide fuel cells production. *J. Therm. Spray Technol.*, **9** (2000), p. 364-368.

[80] A. Notomi and N. Histome, Application of plasma spraying to solid oxide fuel cell production, *Pure Applied Chem*., **68** (1996), p. 1101-1106.

[81] D. Stöver, D. Hathiramani, R. Vaßen and R.J. Damani, Plasma-sprayed components for SOFC applications, *Surf. Coat. Technol.*, **201**(5) (2006), p. 2002-2005.

[82] C.-J. Li, A. Ohmori, and R. McPherson, The relationship between microstructure and Young's modulus of thermally sprayed ceramic coatings, *J. Mater. Sci.* **32**(1997), p.997-1004.

[83] S. Kuroda, Properties and characterization of thermal sprayed coatings-A review of recent research progress, *Thermal Spray 1998: Meeting the Challenges of the 21st century*, C. Coddet (Ed.), ASM International, Materials Park, OH, 1998, p.539-550.

[84] K.A. Khor and Y.W. Gu, Hot isostatic pressing of plasma sprayed yttria-stabilized zirconia, *Mater. Lett.*, **34**(3-6) (1998), p. 263-268.

[85] C.-J. Li and A. Ohmori, Relationship between the structure and properties of thermally sprayed coatings, *J. Therm. Spray Technol.*, **11**(3) (2002), p. 365-374.

[86] X.-J. Ning, C.-X. Li, C.-J. Li and G.-J. Yang, Modification of microstructure and electrical conductivity of plasma-sprayed YSZ deposit through post-densification process, *Mater. Sci. Eng. A*, **428**(1-2) (2006), p. 98-105.

[87] C.-J. Li, C.-X. Li and X.-J. Ning, Performance of YSZ electrolyte layer deposited by atmospheric plasma spraying for cermet-supported tubular SOFC, *Vacuum*, **73**(3-4) (2004), p. 699-703.

[88] P. Fauchais, M. Vardelle, A. Vardelle and J.F. Coudert, *Metall. Trans.* **20B** (1989), p. 263-276.

[89] Y.-Z. Xing, C.-J. Li, C.-X. Li and G.-J. Yang, Influence of through-lamella grain growth on ionic conductivity of plasma-sprayed yttria-stabilized zirconia as an electrolyte in solid oxide fuel cells, *J. Power Sources*, **176**(1) (2008), p. 31-38.

[90] R. Vaßen, D. Hathiramani, J. Mertens, V.A.C. Haanappel and I.C. Vinke, Manufacturing of high performance solid oxide fuel cells (SOFCs) with atmospheric plasma spraying (APS), *Surf. Coat. Technol.*, **202**(3) (2007), p. 499-508.

Chapter 2

Optimization of Process and Microstructure of Atmospheric Plasma-sprayed Yttria Stabilized Zirconia Electrolyte

The velocity and surface temperature of in-flight YSZ particle were measured by a diagnostic analyzer. The optimization of spraying parameters via measured in-flight particle features as well as powder size was conducted. The influences of particle velocity and surface temperature on the microstructure of APS YSZ coating were studied. Low pressure plasma-sprayed YSZ coating and APS PSZ (4.5 mol% yttria stabilized zirconia) were also deposited to make a comparison to APS YSZ coating.

2.1 Introduction

At present, the challenges on the development of SOFC systems are oriented to the cost reduction effort, in order to compete more effectively with other traditional power generating methods [1,2]. In such a context, electrolyte deposition has attracted particular attention. As introduced in Chapter 1, plasma spray process is a promising technique, providing some advantages such as high deposition rate and easy masking for the deposition of patterned structures [3-8], compared with other film formation processes [9]. It has been pointed out that Low Pressure Plasma Spraying (LPPS) and Atmospheric Plasma Spraying (APS) were two variations of plasma spraying for yttria stabilized zirconia (YSZ) electrolyte fabrication [10]. Low cost of APS compared to LPPS make it more competitive. Therefore, APS has been considered as the promising method for YSZ electrolyte fabrication.

Plasma spray process is relatively straightforward in concept but rather complex in function [11]. The plasma torch operates on direct current, which sustains a stable, non-transferred electrical arc between a tungsten cathode and an annular water-cooled copper anode. A plasma forming gases (generally, inert gas, with an enthalpy enhancing gas, such as hydrogen) are introduced into interior of the torch, and the gas becomes partially ionized, and exiting from the nozzle as a plasma jet of high temperature (~10000°C). The ion-electron recombination occurs, releasing considerable enthalpy which is sufficient to melt and accelerate powder to a high velocity. The feedstock powder is fed into a plasma jet, where it is melted and accelerated to high velocities, before it impinges onto a substrate. The inherent feature of plasma spray process determines the coating microstructure differently from the YSZ electrolyte fabricated by other processes.

Although the investigation on YSZ electrolyte has been conducted for a long time, most of the previous investigations were carried out on bulk materials prepared by sintering method and many coating formation processes [12-14]. The electrical properties of APS YSZ coatings were less investigated [15-17]. In this chapter, YSZ coatings were

prepared by APS, using three different powders, under different spray conditions. The effect of spray conditions on in-flight particle parameters was measured. The plasma spray parameters were optimized and the microstructure of YSZ coating was studied.

2.2 Experimental Procedure

2.2.1 Material Feedstock and Coating Preparation

Three commercially available 8 mol% YSZ powders (small size; medium size; large size) were used as feedstock material for plasma spraying. Figure 1 shows the morphology of these three powders. The size distributions of these powders were characterized by a laser diffraction apparatus (MASTERSIZER 2000, Malvern Instruments Ltd., UK) as shown in Figure 2. The details of these three powders are given in Table 1.

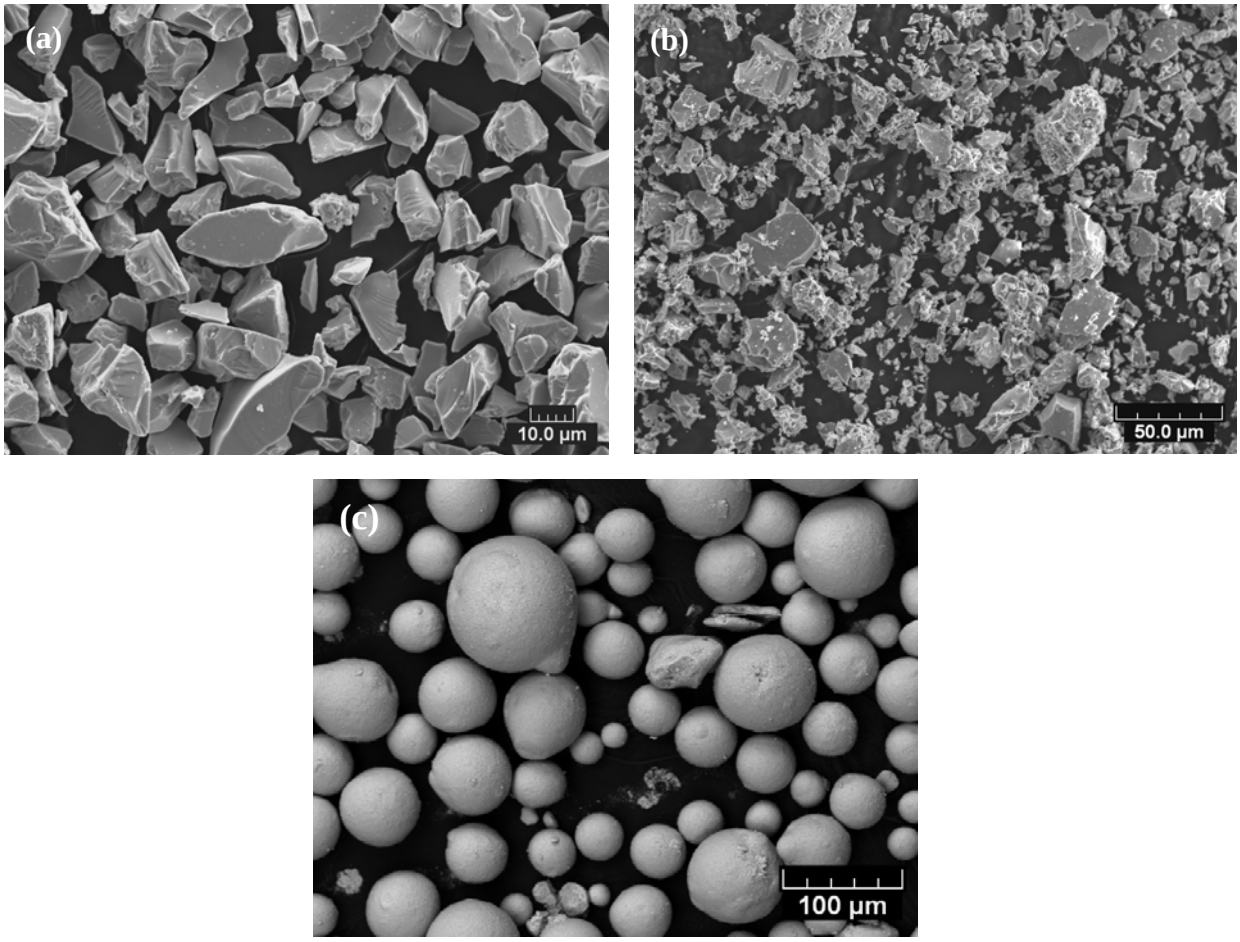

Figure 1: SEM morphology of YSZ powders: (a) small size powders, (b) medium size powders, (c) large size powders.

Table 1: Powders used for plasma spraying

Powder	Supplier	Fabrication method	Size distribution (μm)		
			d(0.1)	d(0.5)	d(0.9)
Small powder	Fujimi, Japan	Fused-crushed	6.1	15.0	25.9
Medium powder	Marion, France	Fused-crushed	4.9	25.6	58.7
Large powder	Tosoh, Japan	Agglomerated-sintered	1.6	31.5	178.2

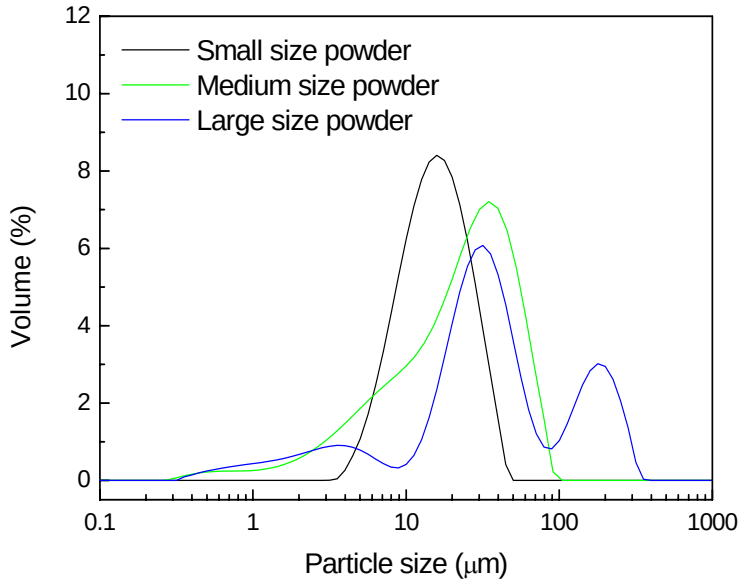

Figure 2: Size distribution of the used YSZ powders.

A Metco PT-3000 atmospheric plasma spraying system with F4MB plasma gun (Sulzer Metco AG, Switzerland) was used to deposit YSZ coatings as shown in Figure 3. The spray parameters are listed in Table 2. During spraying, powders were fed into plasma stream by 10-Twin-systems (Plasma-Technik AG, Switzerland). The coatings were deposited on aluminum plates of dimensions 5 × 7 × 0.3 cm. Prior to spraying, the substrate was grit-blasted with alumina. A robot (ABB, Sweden) was employed to move the spray torch for uniform and reproducible deposition of YSZ layer. The thickness of the as-sprayed coatings was adjusted to 600-1000 μm in different trials. After deposition, the

substrates were dissolved by sodium hydroxide solution to obtain freestanding specimens. After deposition, the substrates were dissolved by sodium hydroxide solution to obtain the freestanding specimens.

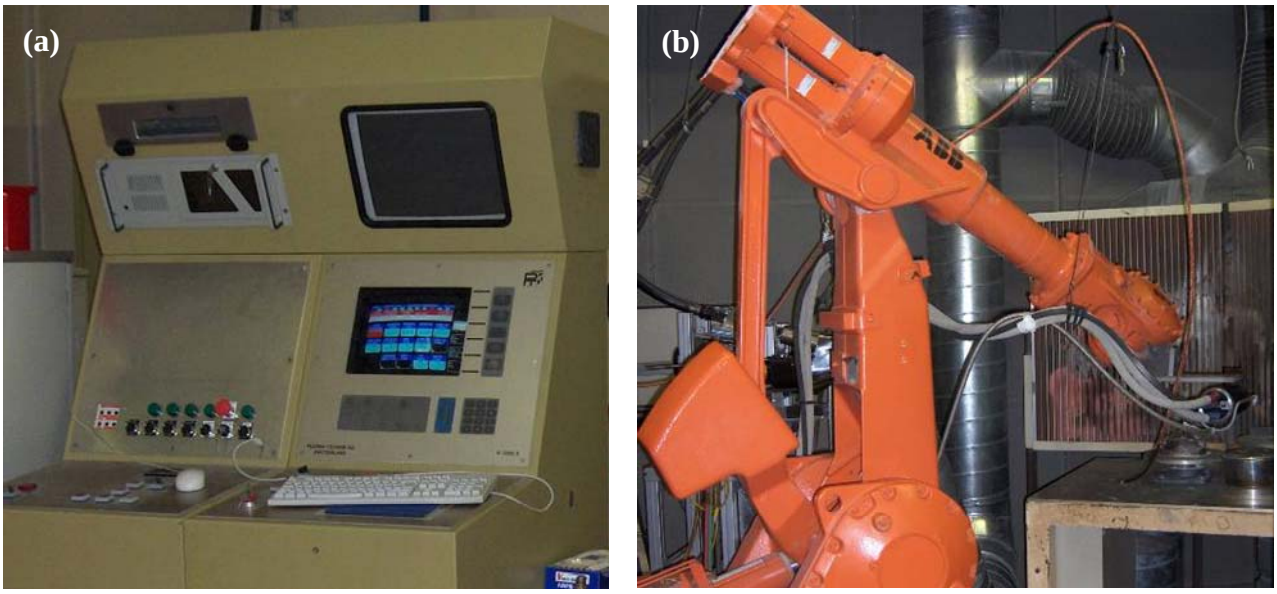

Figure 3: APS equipment: control unit (a) and spray torch with robot (b).

Table 2: Spray parameters used for YSZ coatings.

Arc current (A)	600
Standoff distance (mm)	80-110
Argon ($l \cdot min^{-1}$)	35
Hydrogen ($l \cdot min^{-1}$)	6-13
Helium ($l \cdot min^{-1}$)	0-50
Argon powder carrier gas ($l \cdot min^{-1}$)	3.4-3.8
Gun traverse speed ($mm \cdot s^{-1}$)	400

2.2.2 Microstructure Characterization

To preserve coating microstructure, the obtained YSZ coatings were sawed by a cutter in a feeding velocity of 10-15μm/s and infiltrated by epoxy resin under a low pressure.

The samples were ground with sand paper and polished with diamond paste down to 0.25 μm. The microstructures of the YSZ coatings were examined by scanning electron microscopy (SEM) (JSM5800LV (JEOL, Japan) and Quanta200 (FEI, USA)). For an increased contrast between YSZ and pores, the coating microstructure was examined under both the backscattered electron image (BEI) mode and second electron image (SEI) mode.

The BEI images of the polished coating cross-section taken at a magnification of 200 were employed to estimate coating porosity by the software of scion image (NIH, USA). For obtaining an accurate estimation of coating porosity, 5 images in the random area were used for each coating and an average value was obtained. SEI images at high magnification of 2000 and 5000 were used to examine the defects of the microstructure of YSZ coatings. The phase constitutions of both the powders and the deposited coatings were characterized by X-ray diffraction analyzer (XRD) (D/max2400, RIGAKU, Japan) using a CuKα radiation. A 2θ scanning rate of 10° min^{-1} was used during test.

2.2.3 In-flight Particle Characterization

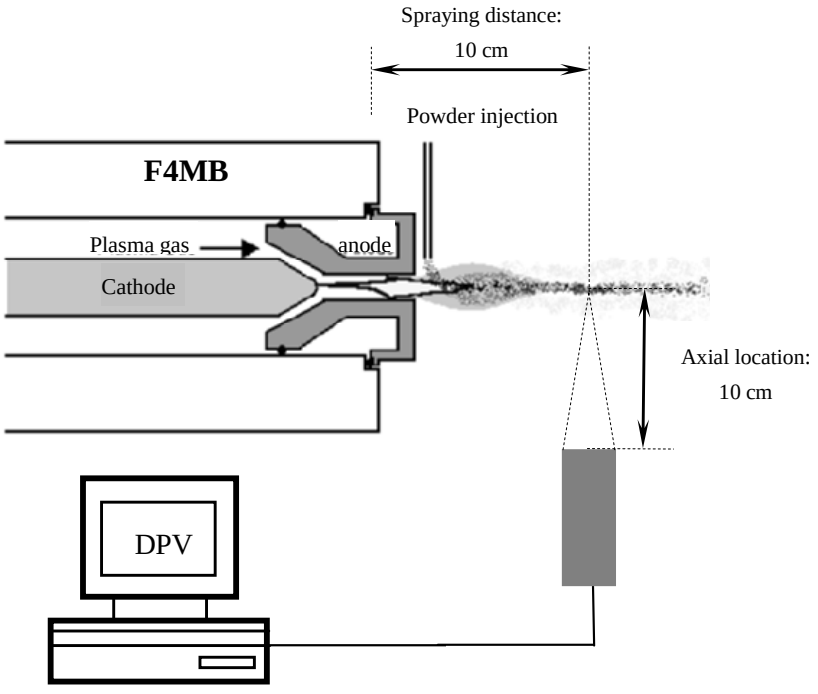

Figure 4: Experimental setup for in-flight particle detection.

The DPV 2000 particle diagnostics system (Tecnar Automation Ltd, Canada) helps to determine the characteristics of spray particles during the flight phase in a specific area of the spray jet [18]. The surface temperature (two-wavelength pyrometry), the speed of the spray particles (light barrier principle) and the diameter (iterative, manual adjustment of the emission coefficients) can all be measured simultaneously. The measuring volume of the sensor head is 0.5 mm^3, which means that only a small area of the spray jet is analyzed per measurement position. The sensor has an XY positioning unit which allows a cross section of the jet to be scanned perpendicularly to the spray axis. In this way, a two-dimensional distribution of the particle characteristics and a formation of the spray jet can be determined.

In this work, the surface temperature and velocity of in-flight particles were measured using the DPV 2000 system as shown in Figure 4. The axial location for the measurement was 100 mm. The spray parameters for in-flight particle measurements were the same as those used for the coating preparation process except the powder feed rate which was lower. In-flight particle parameters were measured at different radial positions from the center of plasma jet. The detection was carried on until the counts of detected particles reached at least 1000 for each set of spray parameters.

2.3 Process Optimization and Coating Microstructure

2.3.1 Process Optimization of Particle Velocity and Temperature

(1) Influence of Powder Size

YSZ particle parameters were measured with DPV2000 at different radial positions for the three powders (H_2:35 l/min; Ar:12 l/min; Current:600 A; Spray distance:100mm). It could be clearly observed in Figure 5(a) that particle velocity depends on the particle diameter as well as on the location of the measurement point. Indeed, particle velocity significantly increases of more than 200 m/s when the measurement point changes from

-1.5 cm under the jet axis to 1 cm above the axis. That corresponds also to the distribution size of the particle into the jet. The largest particles were localized under the jet axis as the smallest were above preferentially.

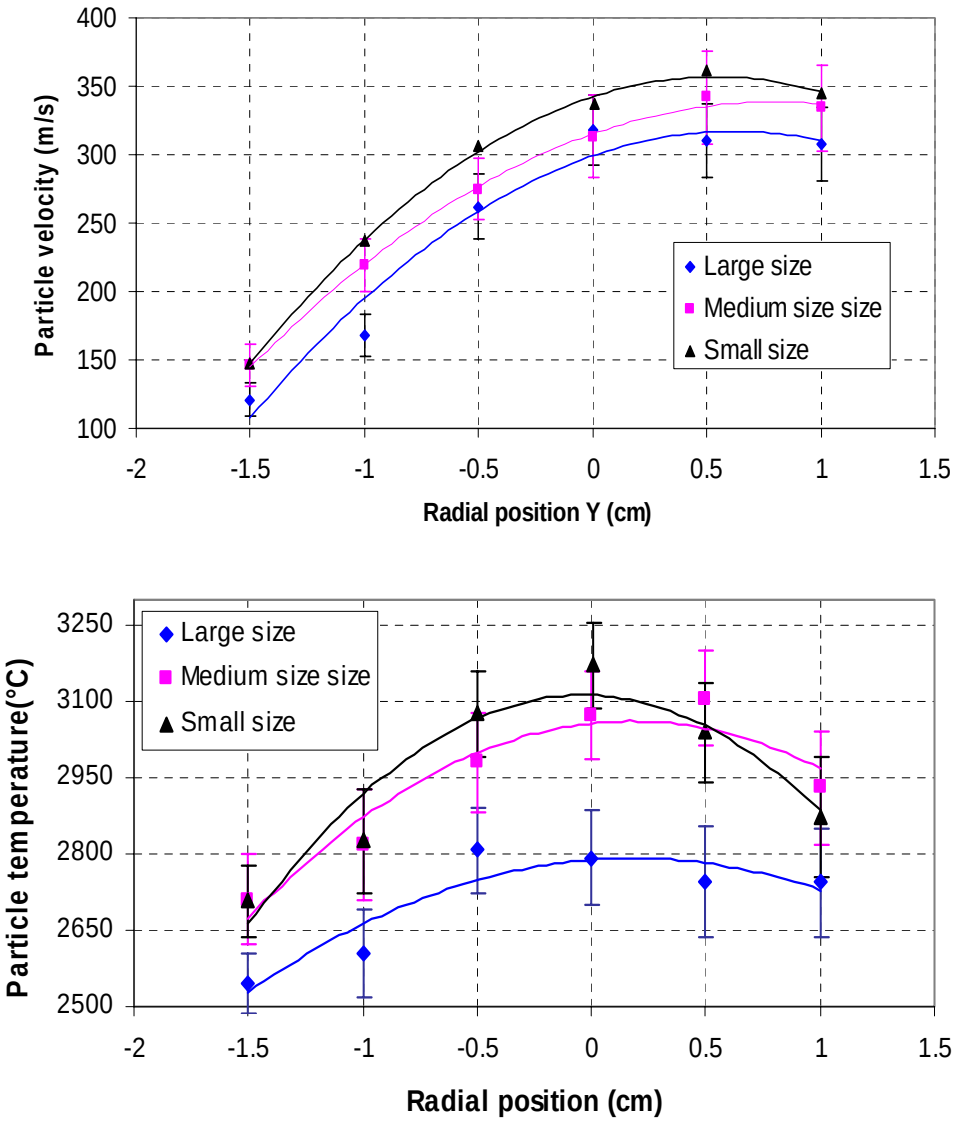

Figure 5: Effect of powder size on the velocity (a) and temperature (b) of YSZ particles.

Comparing the velocity evolutions of different powders, the velocity of the small powder is about 50m/s higher than the larger size powder whatever the measurement locations. For example, at 0.5 cm above the jet axis, the highest velocity of 361 m/s was obtained for the small powder as 310 m/s was obtained for the large powder size at the same location. Once the other spray parameters were fixed, a smaller size particle is much easily accelerated to a higher velocity and it should be easier to heat to a higher

temperature compared with large size particles.

Figure 5(b) shows the effect of powder size on surface temperature at different radial positions, which was similar to the evolution observed on particle velocity. The particle temperature increases with a decrease in powder size and with a measurement locations changing from -1.5 cm to 1 cm relatively to the jet axis. The surface temperature of the small size powders is about 300°C higher than that of the big size powder for the measurement point localized on the jet center that corresponds to the most important difference in temperature. At other radial positions, the temperature differences are smaller than those in the centre, but, the differences of temperature are obvious. These temperatures range from 2500°C for the lowest ones to 3150°C for the highest ones. Then, it must be specified that the particle surface temperatures are higher than the melting point of the YSZ powders (2730°C) in the most radial positions (from -1 cm to 1 cm above the jet axis).

(2) Influence of Spraying Distance

In the last part, the effect of powder size on particle velocity and temperature was examined. The results showed that the highest particle temperature and velocity could be obtained when a small powder is used. In this part, the small size powder (FUJIMI, Japan) was used as a feedstock to investigate the influence of the spraying distance on in-flight particle features (H_2: 35 l/min; Ar: 12 l/min; Current: 600 A; Spray distance: 80-110 mm). Figure 6(a) shows the evolution of in-flight particle velocity at different radial positions when spray distances change from 80 to 110 mm. It could be found that the particle velocity changes in a range of about 200 m/s when measuring at different radial positions, which was similar to the results in the section 2.3.1(1). When the spray distance is 100mm, the velocity reaches the highest value of 360 m/s and then decreases when the spray distance further increases. Figure 6(a) also showed that the particle velocity at 100 mm spray distance is higher than that at other spraying distances in all radial positions. Comparing the velocity evolutions under different spray distances, a difference from 5 to 50 m/s is measured depending on the measurement location.

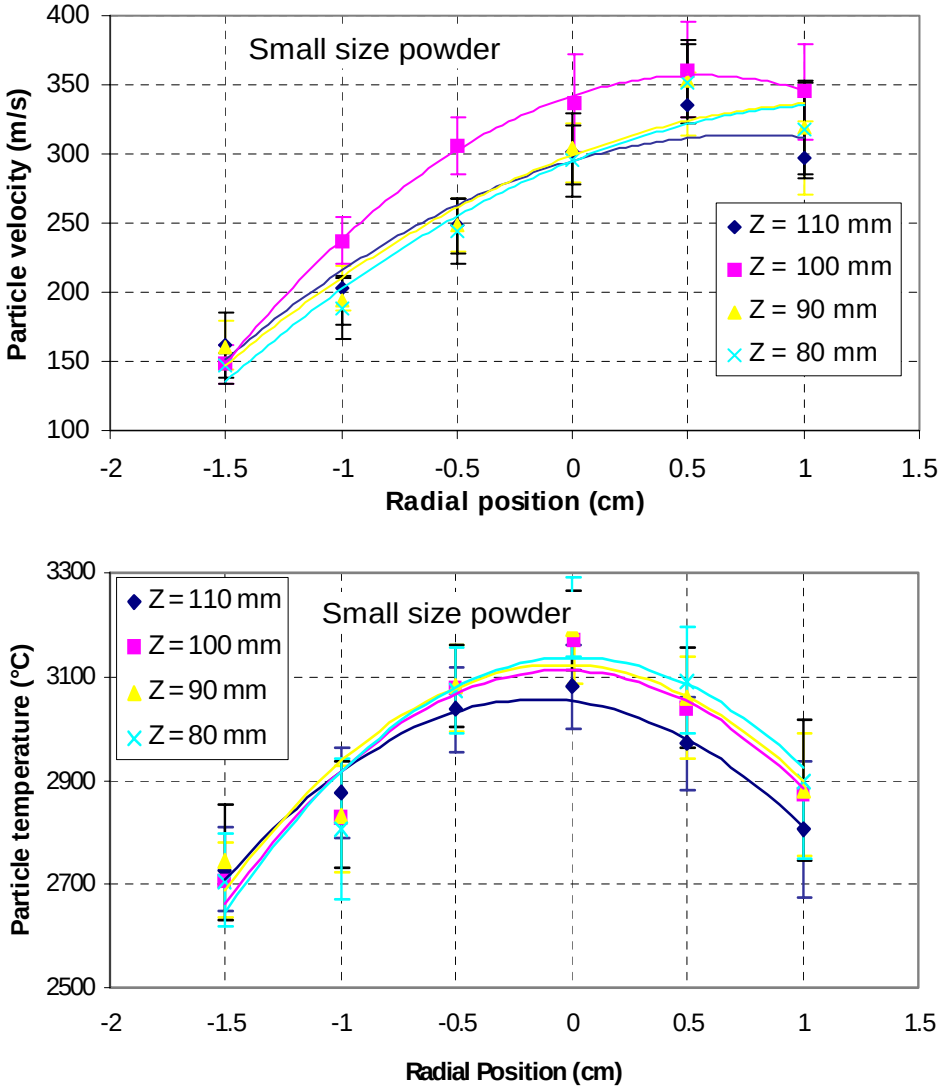

Figure 6: Effect of spraying distance on the velocity (a) and temperature (b) of YSZ particles.

Figure 6(b) shows the effect of spray distance on particle surface temperature. It should be noted that there is no significant difference on surface temperature when the spray distance changes from 80 to 100 mm. When further increasing the spraying distance to 110 mm, the decrease of particle temperature becomes distinct. To obtain an improved plasma-sprayed YSZ electrolyte coating, the high velocity and temperature of in-flight particles are needed. Considering the evolution of particle velocity and surface temperature under different spray distances, it could be concluded that 100 mm is an optimized spray distance for small size YSZ powders.

(3) Influence of Hydrogen Flow Rate

From Figure 7(a), an increase of the velocity of in-flight particles could be observed when increasing H_2 flow rate from 6 to 13 l/min. The most important difference in velocity is obtained for the 0.5 cm radial position leading to an increase of about 60 m/s.

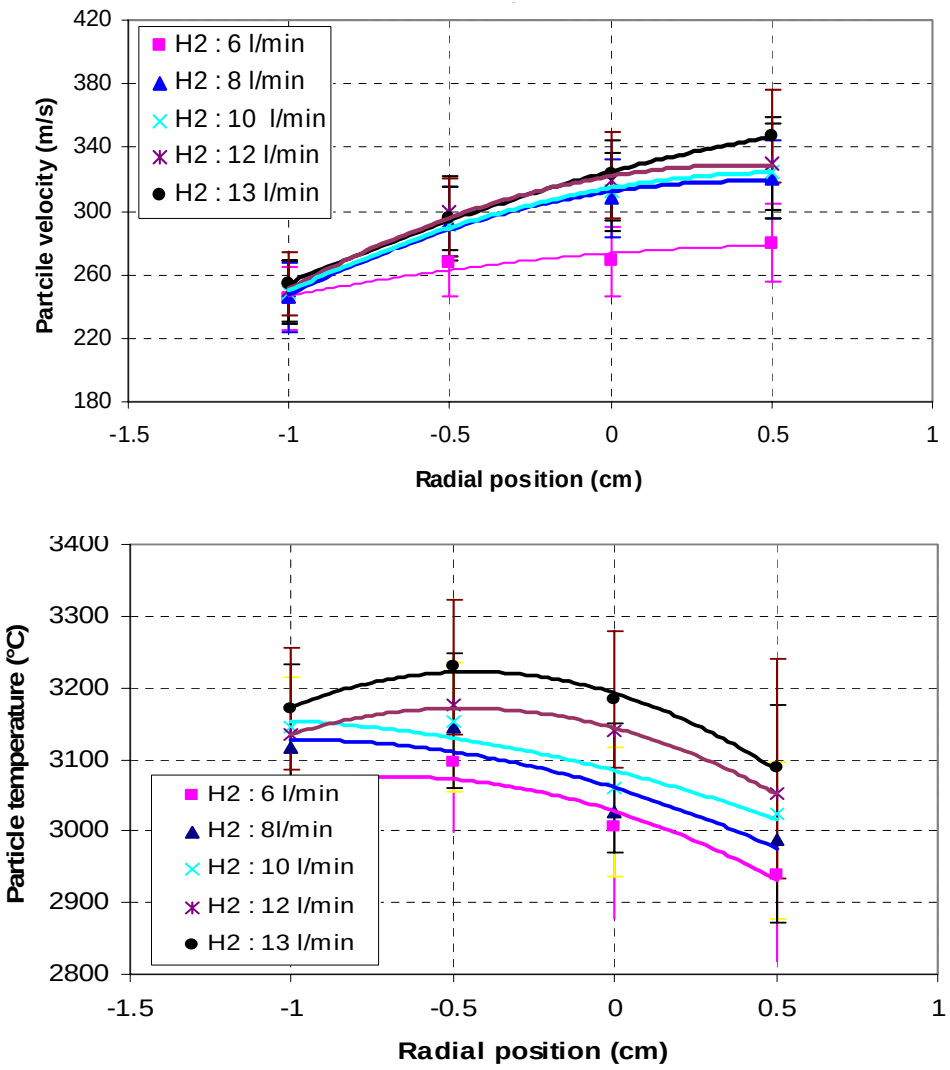

Figure 7: Effect of hydrogen flow rate on the velocity (a) and temperature (b) of YSZ particles (small size powder).

It must be also specified that the most important evolution of the particle velocity vs. the radial measurement position obtained for the highest H_2 flow rate is about 100 m/s increase. The same tendencies could be observed for all H_2 flow rates. From Figure 7(b), it could be observed that the surface temperature of in-flight particles increases when H_2 flow rate increases. Although the difference of particle temperature was not too much, the trend of the effect of hydrogen on the particle temperature was very obvious. It should be

specified that the surface temperature of particles was always above 2900°C whatever the measurement location position or H_2 flow rate. It indicates that the quantity of H_2 in the plasma gas was sufficient to provide the heat enthalpy to heat the small size powder.

Figure 8(a) and (b) show the effect of H_2 flow rate on the velocity and temperature of in-flight particles of the medium size powder. Similar to the small size powder, the increase of H_2 flow rate increases the particle velocity and the particle temperature. The results also show that the particle velocity of medium size powder was lower than that of small size powder when other spray parameters were set to the same, which was exhibited in the 2.3.1(1).

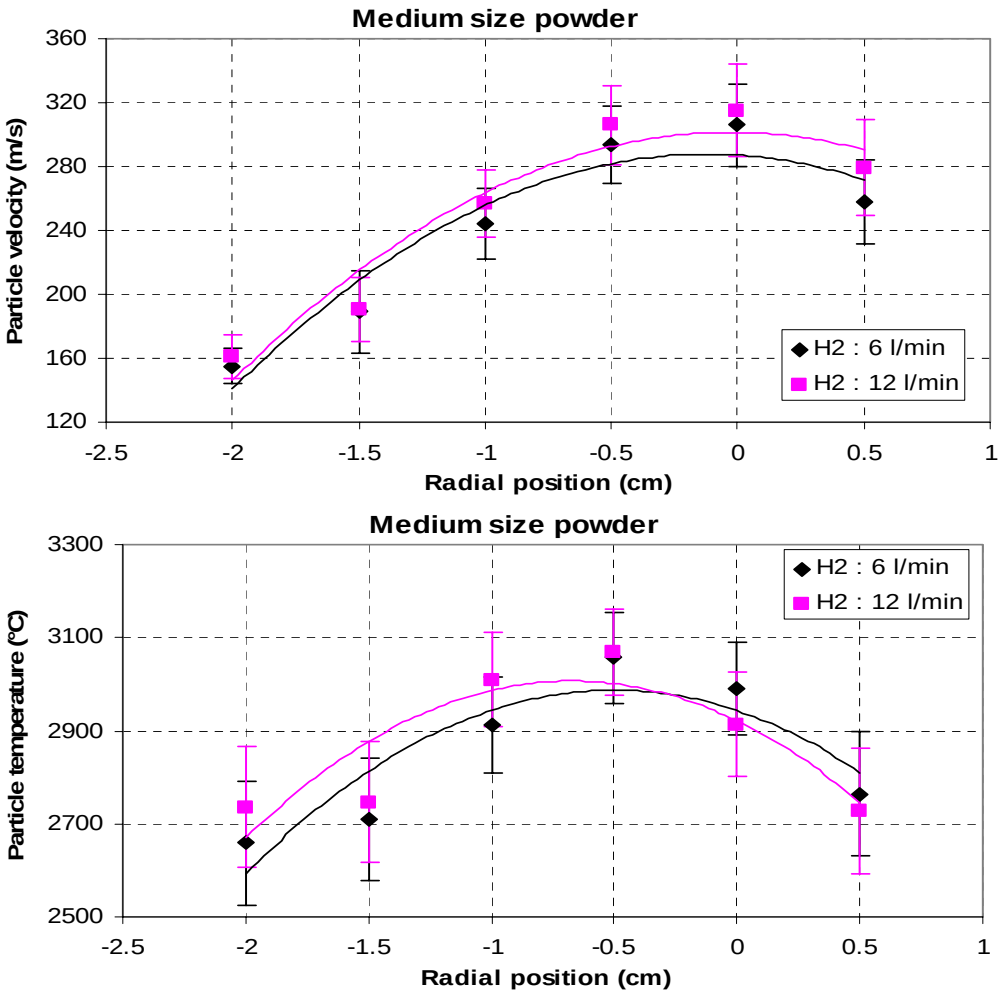

Figure 8: Effect of hydrogen flow rate on the velocity (a) and temperature (b) of YSZ in-flight particles (Medium size powder).

Figure 8(b) shows the influence of H_2 flow rate on particle temperature for medium

size powder. It could be seen that the change of H_2 flow rate has less influence on the particle temperature of medium size powder compared to that of small size powder. This fact indicated that the H_2 flow rate has less influence on particle temperature when the size distribution of powder increases. It should be specified that the surface temperature of medium size particles were less than the melting point of YSZ at the location of 2 cm below the jet center whatever the H_2 flow rate used. That means that some particles were partially molten when deposited with the medium size powder.

(4) Influence of Helium Flow Rate

In this part, Ar-H_2-He plasma was used under different helium flow rates to obtain different mixed gas viscosities, consequently different in-flight particle velocities. Large amount of H_2 is also adaptable to get adequate enthalpy and higher thermal conductivity of the plasma to melt the YSZ particles (Ar: 35 l/min; H_2: 12 l/min; spraying distance: 100 mm; He: 0-50 l/min; feedstock: small size powder). Figure 9(a) and 9(b) give, respectively, the evolution of the particle velocity and particle surface temperature at different radial positions deposited with different helium flow rates. The particle velocity increased with the increases in helium flow rate and with the location of the measurement volume close to the jet axis. The increase in particle velocity is about 40 m/s, when the He flow rate increases from 0 to 50 l/min in the same measurement location. However, the highest particle velocity of APS particles obtained in this study is still lower than that in the LPPS process [8, 19-21]. For example, in the study of Salhi et al. [21], the particle velocity of YSZ powder with a size distribution of 60±21 μm reaches at 335 m/s when sprayed at a chamber pressure of 15 kPa.

Figure 9(b) shows the evolution of the surface temperature of in-flight YSZ particles under different helium flow rates. It could be observed that the particle temperature slightly increases from 50 to 100^{o}C at different radial positions when the auxiliary helium flow rate increases from 0 to 50 l/min. The temperature variation was

about 2-3% in this study. Regarding a precision of ±10% for the temperature measurements with the DPV2000, the differences for the measured temperatures are not significant. Therefore, the obtained results give only a temperature increase trend with the increase of He flow rate.

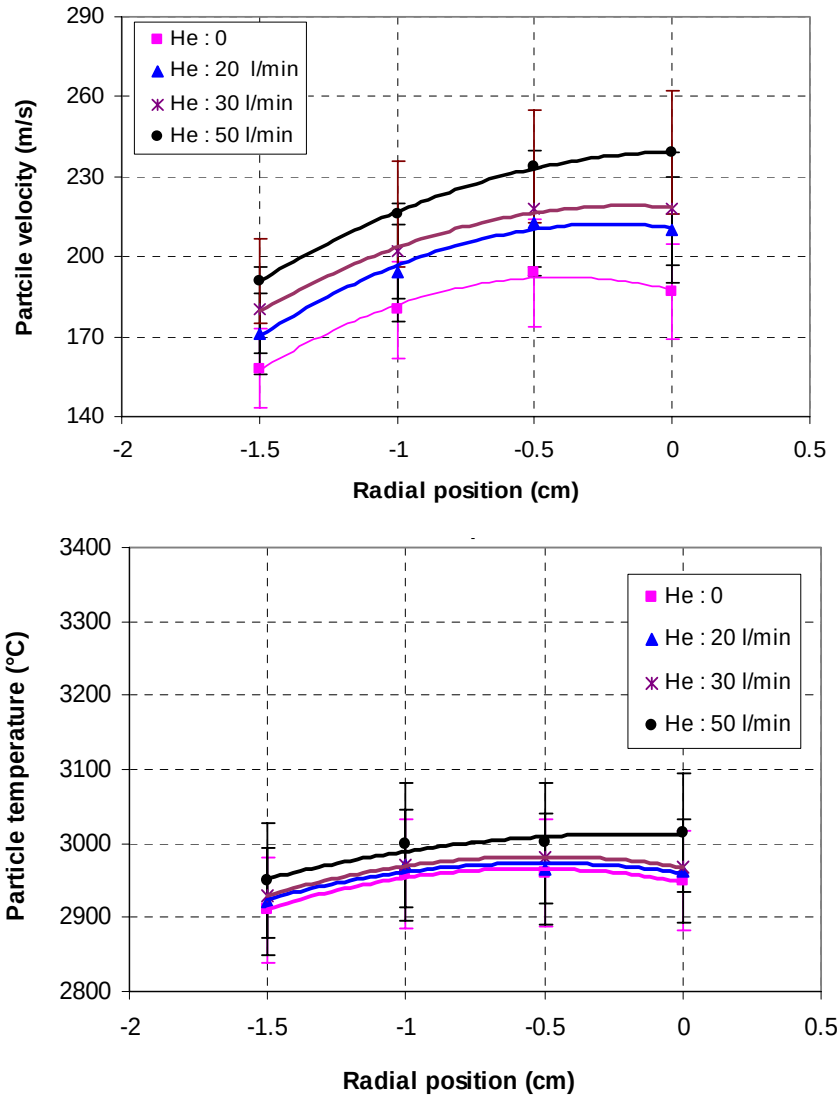

Figure 9: Effect of helium flow rate on the velocity (a) and temperature (b) of YSZ particles. (Medium size powder)

As aforementioned, the obtained results showed that the particle velocity could be elevated by increasing helium flow rate. During spraying process, the acceleration of particles is linked to the flow momentum (ρv^2) [22,23]. The addition of helium increases the plasma flame velocity owing to the fact that helium was light and easily to accelerate.

Meanwhile, helium will increase the plasma viscosity and enhance the acceleration effect of powder. As a result, the particle velocity increases. On the other hand, the addition of helium into Ar-H_2 plasma could slightly increase plasma heat enthalpy. As a result, the particle temperature increases less significantly due to the opposite effect of plasma enthalpy increase and particle dwelling time reduction with increasing He flow rate.

2.3.2 Microstructure of Plasma-sprayed Coating

(1) XRD Results

Figure 10 shows the XRD patterns of the three coatings compared to their starting powders. XRD patterns indicated that all the YSZ coatings consist of well-crystallized single cubic zirconia phase as the same as their feedstock powders. All the obtained coatings were composed of pure cubic zirconia and the difference of impurity on coating microstructure could be eliminated.

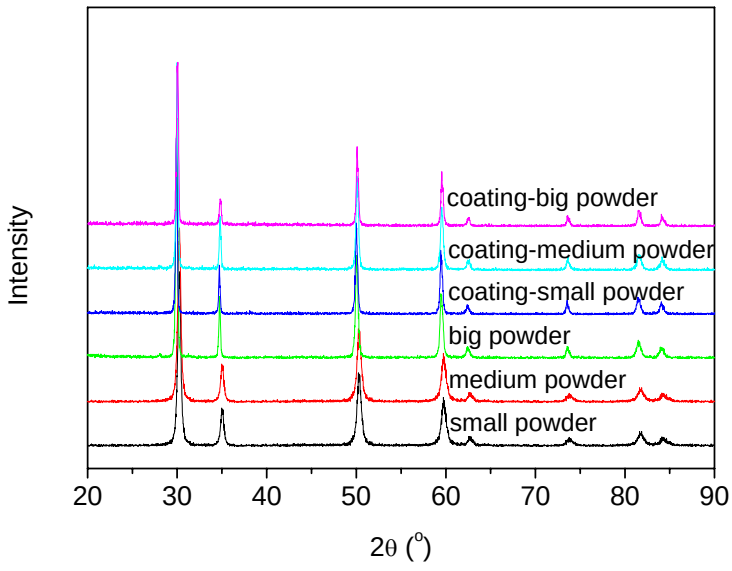

Figure 10: XRD patterns of the plasma-sprayed YSZ coatings in comparison with the starting powders.

(2) SEM Results

Plasma-sprayed coating is formed by a stream of molten or partially molten droplets

impacting on a substrate. The individual molten droplets spread to thin lamellae, stacking of which constitutes the deposit. As a result, a plasma-sprayed coating generally presents a lamellar structure.

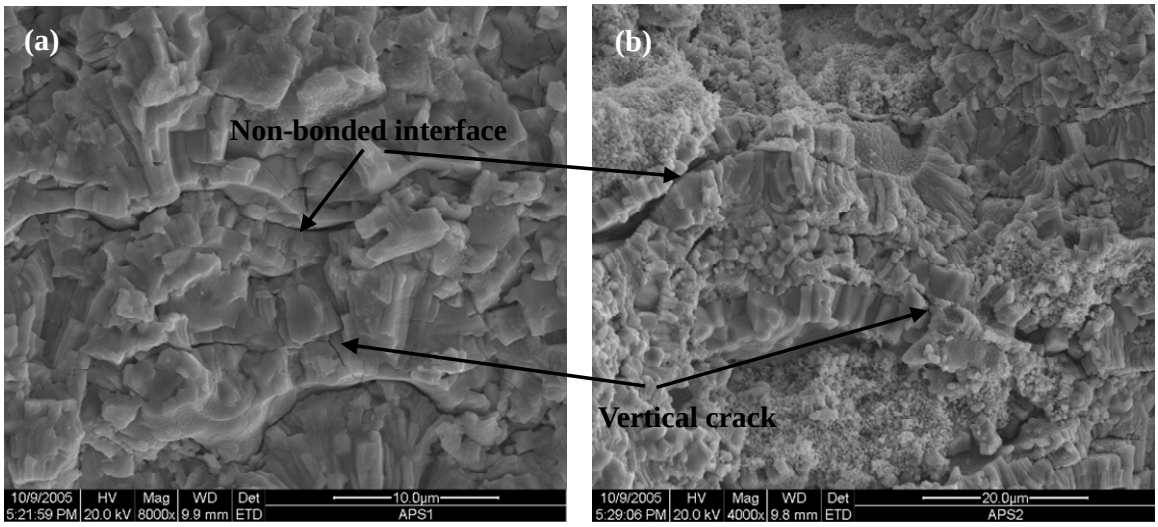

Figure11: Morphology of a cross-section of the fractured plasma-sprayed YSZ coatings deposited with (a) molten and (b) partially molten droplets.

Figure 11 shows the fractured cross-sectional morphology of the fractured plasma-sprayed YSZ coating deposited with molten and partially molten droplets. Lamellar microstructure was present in the obtained YSZ coatings. Pores were always present in the plasma-sprayed ceramic coating. As aforementioned, these pores could be divided into two kinds: large pores (1-10 µm) and small pores (<0.1 µm). With regards to the small pores, they could be also classified as two types: non-bonded interfaces and vertical cracks (intra-lamellae crack) in individual lamellae [24] as shown by arrows in Figure 11.

(i) Influence of Particle Velocity

The influence of particle velocity on YSZ coating microstructure was studied through varying He flow rate. Figure 12 shows the backscattered electron images (BEI) of the polished cross-sectional microstructure of APS YSZ coating deposited with the medium size powder under different He flow rates. The YSZ coating deposited with particles of the highest velocity (He flow rate: 50 l/min) presents the densest microstructure among

the three coatings. It seems that high particle velocity is favorable to deposit coating with a low porosity.

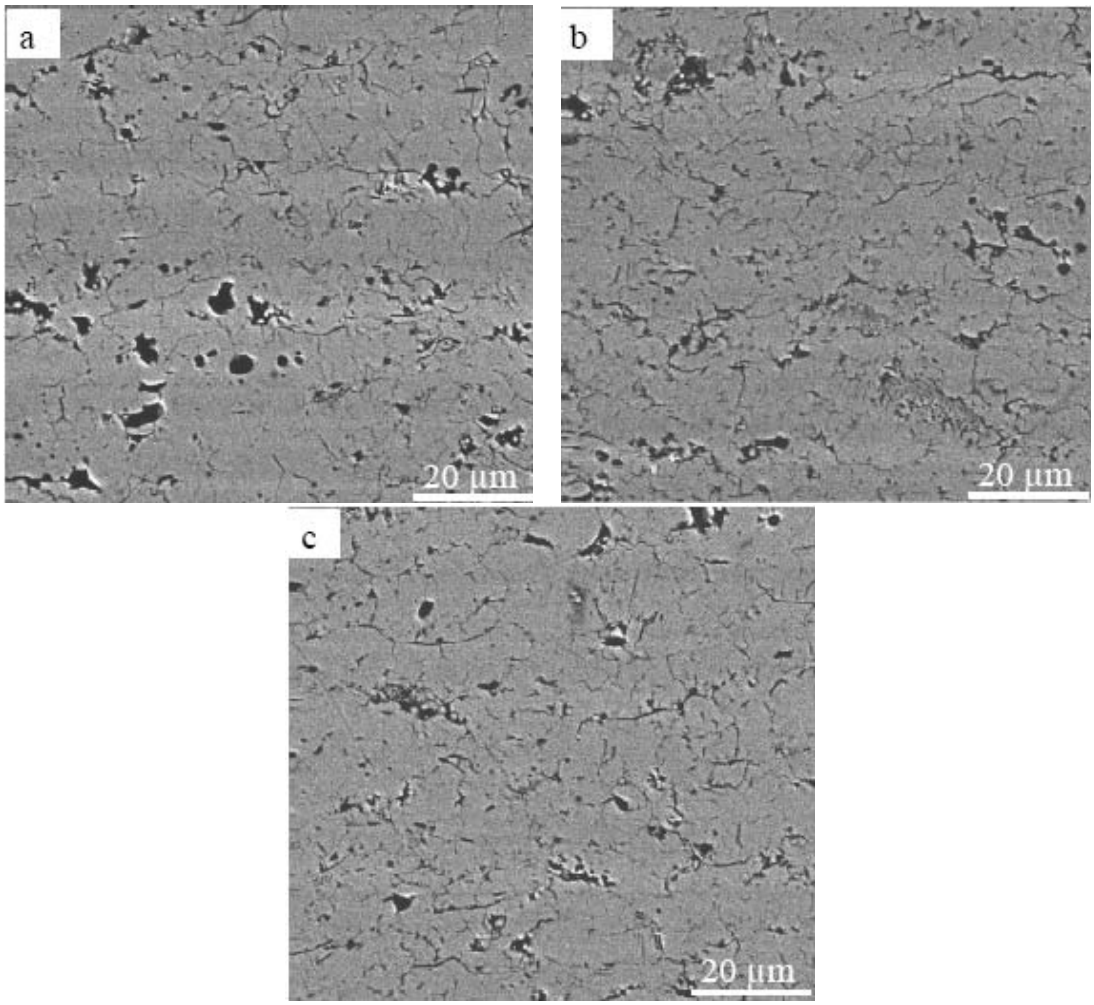

Figure 12: Cross-sectional microstructure of the YSZ coatings deposited with different He additions to plasma gas: (a) without He, (b) He: 30 l/min, (c) He: 50 l/min.

(ii) Influence of Particle Temperature

Figure 13 shows the polished cross-sectional microstructure of the APS YSZ coating deposited with small size powder under different H_2 flow rates. It could be found that many large pores are present in the coating sprayed with low H_2 flow rate. Although it is difficult to recognize whether these pores are present in the as-sprayed coating or caused by the sample preparation, it could be deduced that the coating deposited with high H_2

flow rate presents a dense coating microstructure. The results indicated that a high particle temperature is favorable to achieve a dense coating. However, it should be considered that the too high percentage of H_2 in the plasma gas is harmful to torch cathode due to high thermal conductivity of plasma and therefore high-temperature corrosion of the tungsten. In this thesis, a H_2 flow rate of 12 l/min with an argon flow rate of 35 l/min was regarded as an optimized plasma gas for the deposition of YSZ coatings.

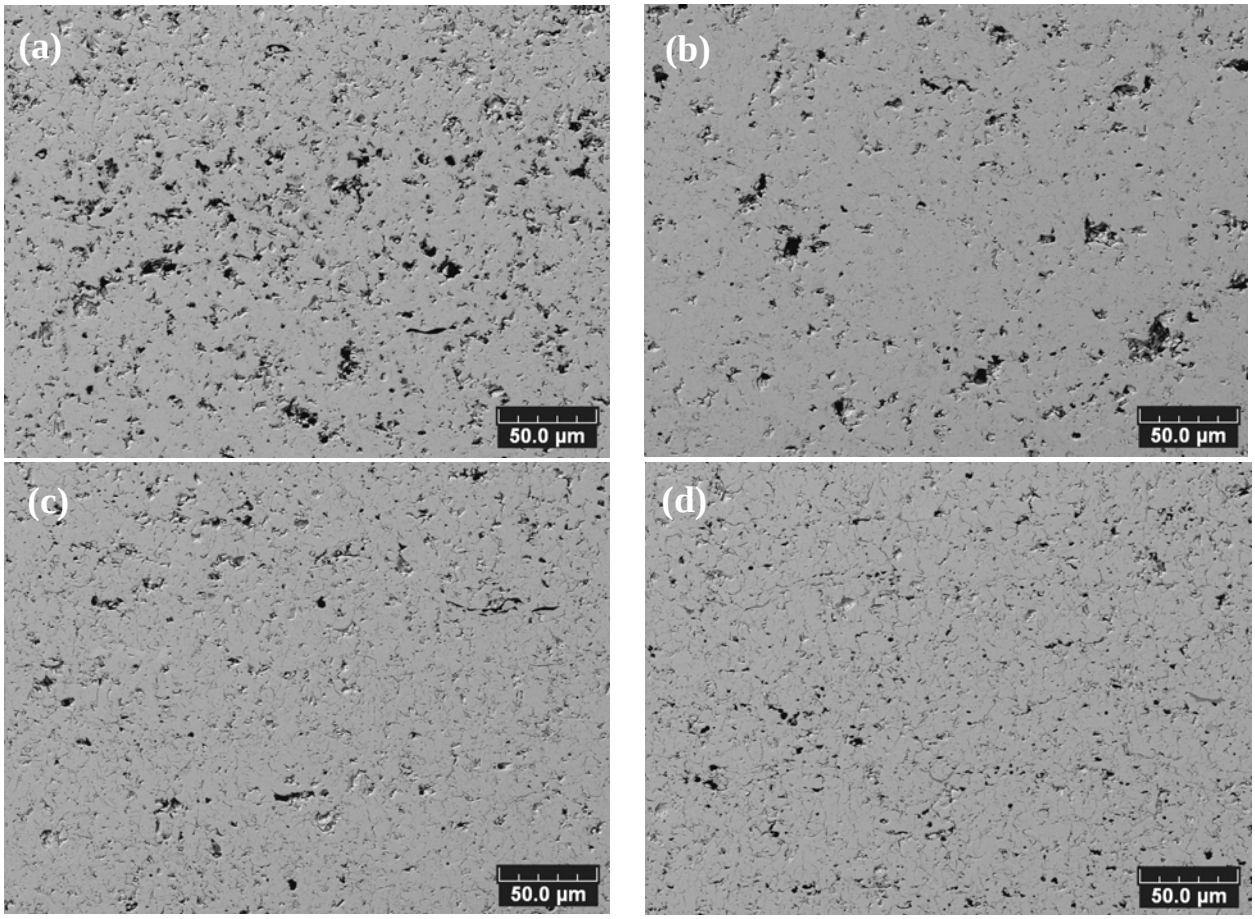

Figure 13: Cross-sectional microstructure of YSZ coatings deposited under different H_2 flow rates: (a): 6 l/min; (b): 8 l/min; (c): 10 l/min (d): 12 l/min.

(3) Low Pressure Plasma-sprayed Coating

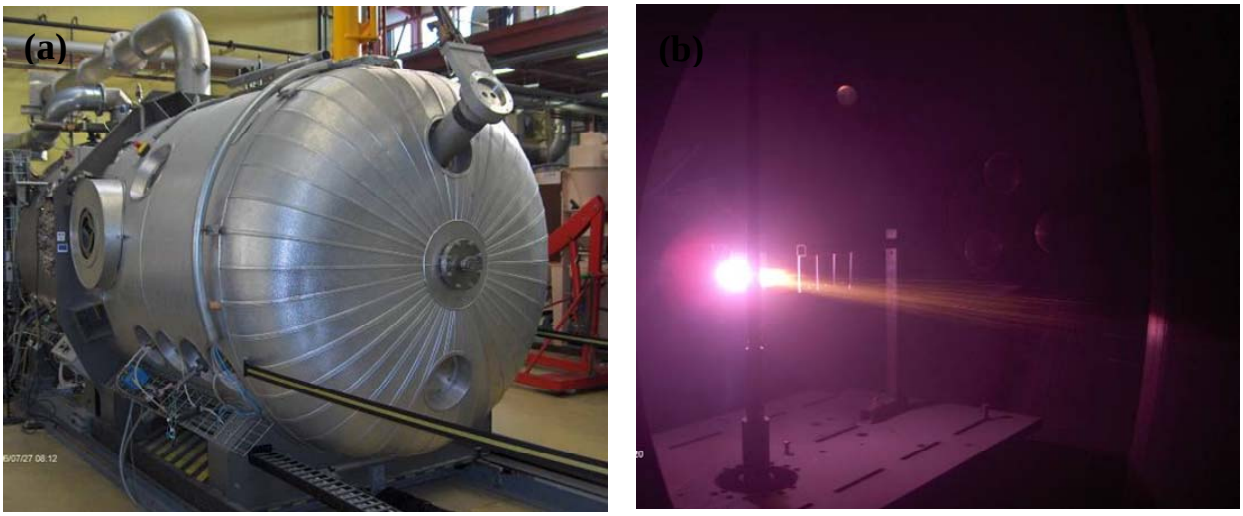

Figure 14: (a) LPPS equipment and (b) spraying process.

The low pressure plasma-sprayed (LPPS) YSZ coatings were also fabricated to make a comparison with APS coatings. The plasma spraying was carried out using the LPPS system (PT-2000) with F4VB torch in an argon gas atmosphere under low-pressure conditions as shown in Figure 14. Spray parameters are listed in Table 3. The small size powders were used as feedstock materials. The coatings were deposited on 5 ×7 ×0.3 cm copper plates. Prior to spraying, the substrate was grit-blasted with alumina at a pressure of about 0.2 MPa.

Arc current (A)	700
Plasma arc power (kW)	45
Chamber pressure (MPa)	0.02
Standoff distance (mm)	260
Argon ($l \cdot min^{-1}$)	45
Hydrogen ($l \cdot min^{-1}$)	14
Powder carrier gas ($l \cdot min^{-1}$)	3.7

Table 3: Low pressure plasma spray parameters used.

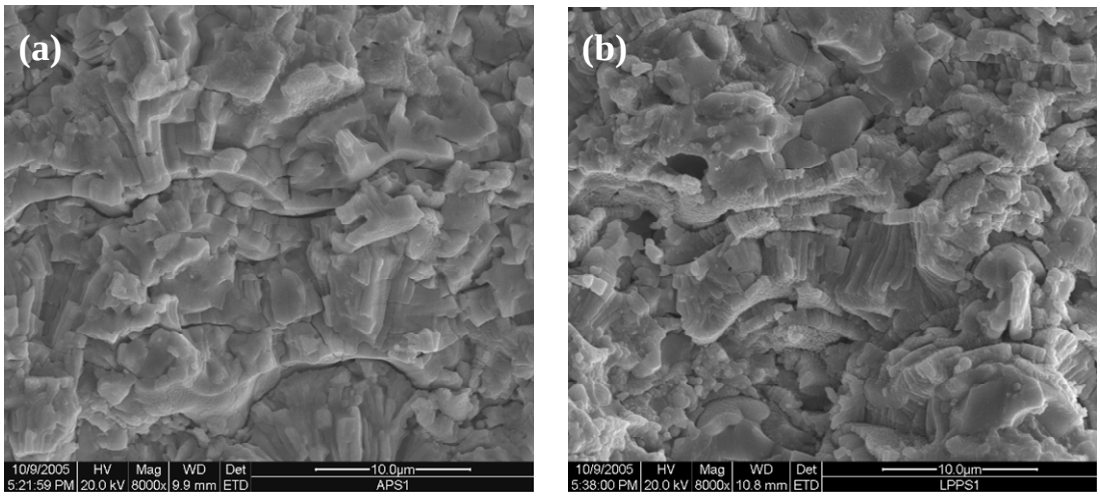

Figure 15: SEM surface morphologies of YSZ coatings: (a) APS, (b) LPPS.

The preheating of the substrate was also performed using plasma transferred arc just before deposition. The substrate temperature was measured with an infrared pyrometer. When the surface temperature reached 600°C, the powder was fed and the spraying started. A robot (ABB, Sweden) was employed to move the spray torch for uniform and reproducible deposition of YSZ layer. After deposition, the substrates were dissolved by nitric acid to obtain the freestanding specimens.

Figure 15 shows the cross-sectional morphology of the fractured LPPS YSZ coatings compared to APS coating. The figures reveal a presence of the non-bonded interface between lamellas resulting from poor adhesion between the splats, and vertical cracks resulting from stress relaxation along the direction perpendicular to splat boundaries, which were inherent characteristics of plasma-sprayed ceramic coating. It seems that there are more vertical cracks in the APS coating and the width of non-bonded interface of APS coating was bigger than that of LPPS coating.

It could be observed that there are less microcracks on the surface of LPPS (Figure 16a) deposit than that of APS (Figure 16b) although it is difficult to indicate which coating has more porosity (Figure 17a and 17b). There may be two reasons for this phenomenon. On one hand, the LPPS deposit is maintained at much a higher temperature than in the APS deposit due to the increased interaction between the plasma jet and the

substrate (caused by a longer plasma jet), coupled with the absence of convective cooling of the substrate. On the other hand, LPPS can produce higher particle velocity than APS and increased particle velocity causes enhanced flattening and spreading of the droplet. Although it was hard to conclude that LPPS coating is denser than APS coating microstructure than APS coating according to the cross-sectional microstructure, the LPPS coating presents a better performance than that of APS coating, which will be reflected in the measured coating properties presented in the following chapter.

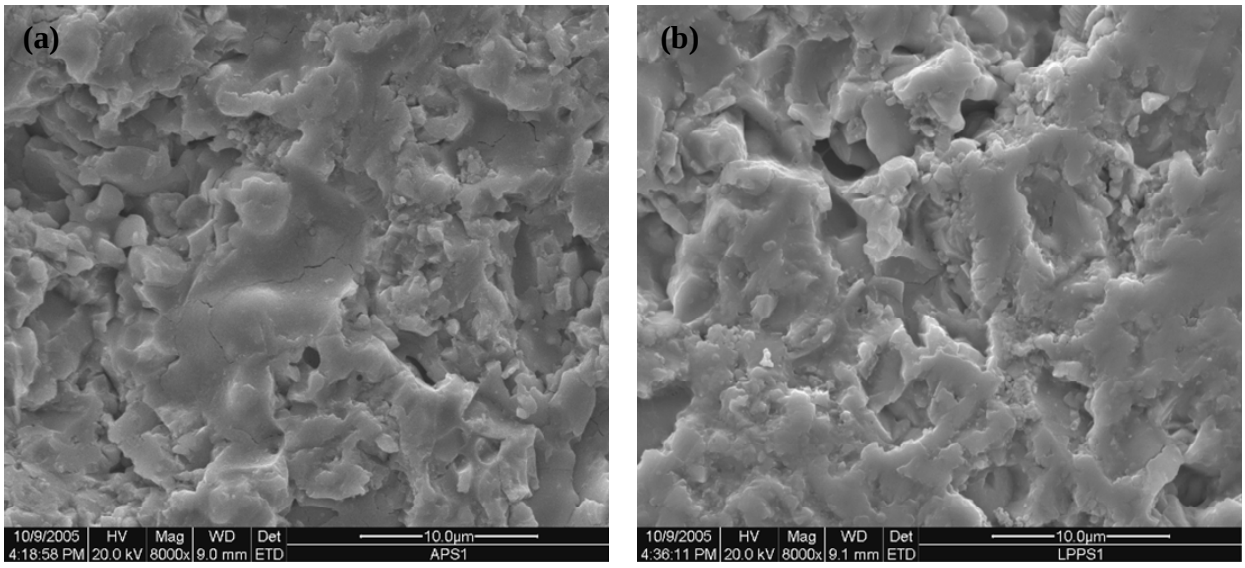

Figure 16: SEM surface morphology of YSZ coatings (a) APS, (b) LPPS.

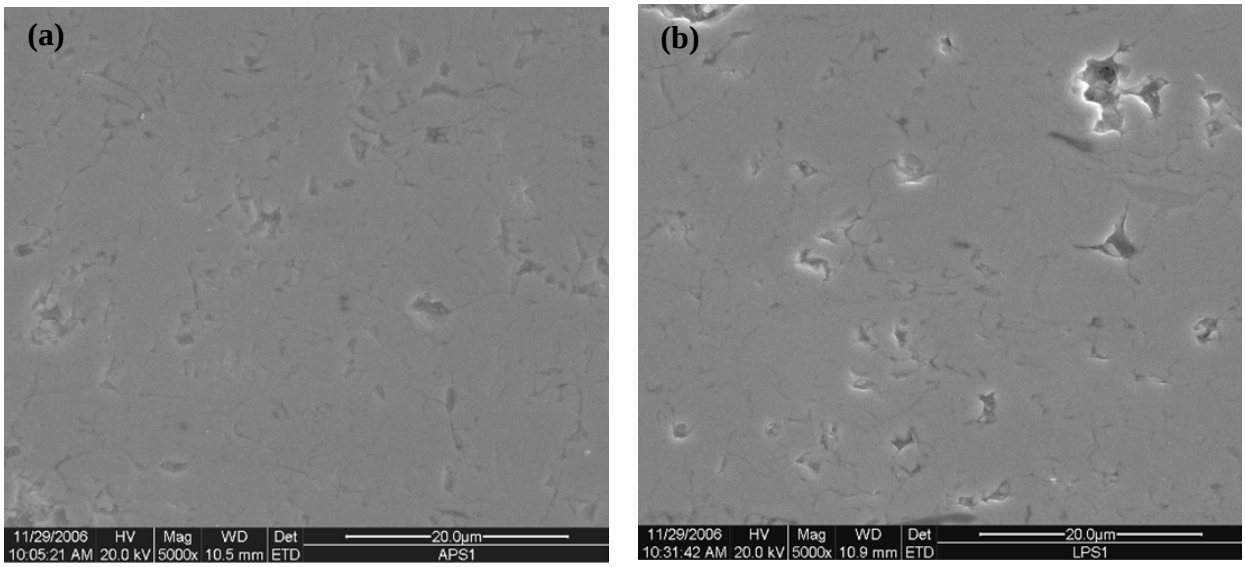

Figure 17: SEM polished cross-sectional microstructure of YSZ coatings (a) APS, (b) LPPS.

(4) Materials Composition

A 4.5 mol% yttria stabilized yttria (PSZ, Plasmatex 1086) powder was also used as feedstock in this study to examine the influence of quantity of dopant yttria on coating ionic conductivity. The powder has a size distribution of 10-40 μm. All the spraying conditions of PSZ coating are the same as the aforementioned APS YSZ coating. Figure 18 shows fractural cross-sectional microstructure of the as-sprayed PSZ coatings compared to YSZ coating (deposited with small size powder as shown in Figure 11(a)).

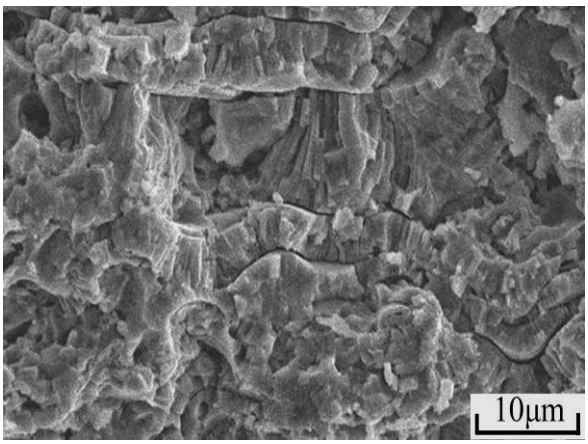

Figure 18: SEM fractual cross-sectional microstructure of PSZ coating.

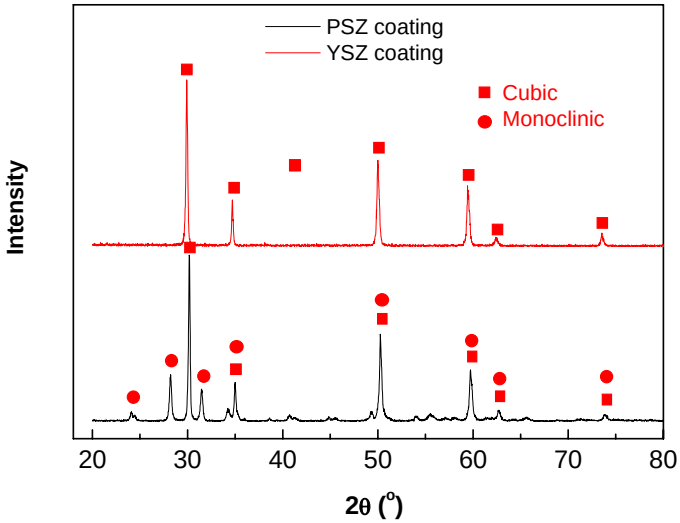

Figure 19: XRD pattern of PSZ coating as well as YSZ coating.

As well known, 4.5 mol% yttria stabilized zirconia is a partially stabilized zirconia. Cubic and monoclinic phases exist in the feedstock powder. An XRD pattern is used to examine the phase structure of the obtained coating. The patterns shown in Figure 19 indicate that the PSZ coatings consist of monoclinic and cubic zirconia phase. Meanwhile the YSZ coating presents single cubic coating.

2.4 Conclusions

In this chapter, the influences of powder size, spraying distance, hydrogen flow rate and helium flow rate on the velocity and surface temperature of in-flight YSZ particles were studied via applying DPV2000 diagnostics. The effect of particle velocity and surface temperature on coating microstructure was examined. The subsequent results were employed for the optimization of spraying parameters for YSZ electrolyte deposition. Main conclusions could be drawn as follow:

(1) The velocity and surface temperature of in-flight particle were strongly influenced by the particle size of feedstock. Small size powder was easier to reach a high particle temperature and a high particle velocity.

(2) The spraying distance (in the range of 80-110mm) has little effect on the surface temperature of YSZ particles and a more significant influence on particle velocity under the present spray condition. According to the results, the 100mm was an optimized spraying distance for YSZ coating in the present study.

(3) The surface temperature of in-flight particle increased with the increase of H_2 flow rate, when the small size powder was used. The results also show that the increase of H_2 flow rate has a slightly positive effect on the particle velocity.

(4) The particle velocity increaement contributed by increasing He flow rate from 0 to 50 l/min is about 40 m/s. Due to the opposite effect of plasma enthalpy increase and particle dwelling time reduction resulting from He addition, the particle temperature increases less significantly.

(5) Polished cross-sectional microstructure of YSZ coatings showed that the increase of both particle velocity and particle temperature has a positive effect on the increase of coating density. High velocity and high temperature of YSZ particle were essential to obtain dense YSZ electrolyte coating.

(6) Through examination from the coating surface and the fractural cross-sectional morphologies, the low pressure plasma-sprayed YSZ coating showed less vertical cracks and less width of non-bonded interface. However, no significant difference on coating porosity was found compared to the APS coating.

2.5 References

[1] T.P. Chen, J.D. Wright and K. Krist, in: U. Stimming, S.C. Singhal, H. Tagawa, W. Lehnert (Eds.), SOFC V, The electrochemical society, Pennington, NJ, 1997.

[2] B.C.H. Steele, Material science and engineering: The enabling technology for the commercialisation of fuel cell systems, *J. Mater. Sci.* **36**(5) (2001), p. 1053-1068.

[3] M. Lang, T. Franco, G. Schiller and N. Wanger, Electrochemical characterization of vacuum plasma sprayed thin-film solid oxide fuel cells (SOFC) for reduced operating temperatures, *J. Appl. Electrochem.* **32**(8) (2002), p. 871-874.

[4] C.-J. Li, C.-X. Li and X.-J. Ning, Performance of YSZ electrolyte layer deposited by atmospheric plasma spraying for cermet-supported tubular SOFC, *Vacuum* **73**(3-4) (2004), p. 699-703.

[5] C.-J. Li, X.-J. Ning and C.-X. Li, Effect of densification processes on the properties of plasma-sprayed YSZ electrolyte coatings for solid oxide fuel cells, *Surf. Coat. Technol.* **190**(1) (2005), p. 60- 64.

[6] A. Notomi and N. Histome, Application of plasma spraying to solid oxide fuel cell production, *Pure Appl. Chem.* **68**(5) (1996), p. 1101-1106.

[7] S. Rambert, A. J. McEvoy and K. Barthel, Composite ceramic fuel cell fabricated by vacuum plasma spraying, *J. Eur. Ceram. Soc.* **19**(6-7) (1999), p. 921-923.

[8] M. Lang, R. Henne, S. Schaper and G. Schiller, Development and characterization of vacuum plasma sprayed thin film solid oxide fuel cells, *J. Therm. Spray Techn.*, **10**(4) (2001), p. 618-625.

[9] J. Will, A. Mitterdorfer, C. Kleinlogel, D. Perednis and L.J. Gauckler, Fabrication of thin electrolytes for second-generation solid oxide fuel cells, *Solid State Ionics*, **131**(102) (2000), p. 79-96.

[10] S.C. Singhal, Advances in solid oxide fuel cell technology, *Solid State Ionics*, **135**(1-4) (2000), p. 305-313.

[11] A.A. Kulkarni, S. Sampth, A. Goland, H. Herman, A.J. Allen, J. Ilavsky, W. Gong and S. Gopalan, Plasma spray coatings for producing next-generation supported membranes, *Topics in catalysis* **32**(3-4), 2005, p.241-249.

[12] M. Kurumada, H. Hara and E. Iguchi, Oxygen vacancies contributing to intragranular electrical conduction of yttria-stabilized zirconia (YSZ) ceramics, *Acta Mater.* **53**(18) (2005), p. 4839-4846.

[13] X. Guo and R. Waser, Electrical properties of the grain boundaries of oxygen ion conductors: acceptor-doped zirconia and ceria, *Prog. Mater. Sci.* **51**(2) (2006), p. 151-210.

[14] C. T. Yang, W. J. Wei and A. Roosen, Electrical conductivity and microstructures of $La_{0.65}Sr_{0.3}MnO_3$-8 mol% yttria-stabilized zirconia, *Mater. Chem. Phys.* **81**(1) (2003), p. 134-142.

[15] X.-J. Ning, C.-X. Li, C.-J. Li and G.-J. Yang, Effect of powder structure on microstructure and electrical properties of plasma-sprayed 4.5 mol% YSZ coating, *Vacuum*, **80**(11-12) (2006), p. 1261-1265.

[16] X.-J. Ning, C.-X. Li, C.-J. Li and G.-J. Yang, Modification of microstructure and electrical conductivity of plasma-sprayed YSZ deposit through post-densification process, *Mater. Sci. Eng. A*, **428**(1-2) (2006), p. 98-105.

[17] X.-J. Ning, Study on the fabrication of zirconia based electrolyte for SOFC by atmospheric plasma spraying, Dissertation of Xi'an Jiaotong University, 2005, (in Chinese).

[18] www. tecnar.com.

[19] V. Rat, E. Bouyer and R.H. Henne, *Thermal Spray 2003: Advancing the Science and Applying the Technology*, B. R. Marple, C. Moreau, Ed., ASM International, Materials Park, OH, 2003, p. 1269-1278.

[20] S. Sodeoka, M. Suzuki, T. Inoue, Thermal Spray 2001: *New Surfaces for a New Millenium*, C.C. Berndt, K.A. Khor, E.F. Lugscheider, Ed., ASM International, Materials Park, OH, 2001, p. 737-741.

[21] Z. Salhi, S. Guessasma, P. Gougeon, D. Klein and C. Coddet, Diagnostic of YSZ in-flight particle characteristics under low pressure VPS conditions, *Aerosp. Sci. Technol.* **9**(3) (2005), p. 203-209.

[22] L. Zhao, K. Seemann, A. Fischer and E. Lugscheider, Study on atmospheric plasma spraying of Al_2O_3 using on-line particle monitoring, *Surf. Coat. Technol.* **168**(2-3) (2003), p. 186-190.

[23] M. Li and P. D.Christofides, Multi-scale modeling and analysis of an industrial HVOF thermal spray process, *Chem. Eng. Sci.* **60**(13) (2005), p. 3649-3669

[24] C.-J. Li, A. Ohmori, Relationship between the structure and properties of thermally sprayed coatings, *J. Therm. Spray Technol.* **11**(3) (2002), p. 365-374.

Chapter 3

Electrical Property of Plasma-sprayed YSZ Electrolyte (as-sprayed and microwave sintered coating)

In the first part, the ionic conductivity of APS YSZ coatings was measured. The feature and limitation of ionic conductivity of plasma-sprayed coatings were studied. In the second part, the temperature dependence of ionic conductivity of YSZ coatings was observed and discussed. The intragrain-intergrain conductivity model and dissociation-migration energy model were employed to discuss this phenomenon. In the third part, microwave sintering was used to sinter the as-sprayed coatings. The modification of microstructure and ionic conductivity of plasma-sprayed coatings was investigated.

3.1 Ionic Conductivity of Plasma-sprayed YSZ Coating

3.1.1 Measurement Set-up

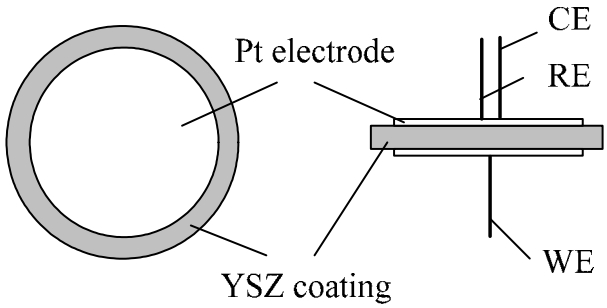

Figure 1: Scheme of the arrangement of a three-electrode assembly for the measurement of ionic conductivity along the perpendicular direction

The ionic conductivity of plasma-sprayed YSZ coatings along both perpendicular and parallel direction with respect to coating surface was evaluated with two different measuring methods. The ionic conductivity along the perpendicular direction was measured using a potentiostat/galvanostat based on a three-electrode assembly approach (Figure 1) [1]. The circular free-standing YSZ coatings with a diameter of 15 mm were prepared for the measurements. To ensure the measuring area of the circular planar sample, platinum glue was pasted on the both sides of the sample with a specific effective area of 1 cm^2 and a thickness of 600~800 μm.

The pasted sample was dried at 100°C for 30 min and then heated to 850°C with a heating rate of 5°C/min and kept at 850°C for 30 min. The reference electrode (referenced RE in Figure 1) and counter electrode (referenced CE in Figure 1) were connected to one side of the sample, while the working electrode (referenced WE in Figure 1) was connected to the other side of the sample. In this study, the measurement was conducted under isothermal condition. The data were collected after 20 minutes when the furnace temperature reached the prescribed point. According to the linear relation between current and potential difference, the resistivity and subsequently conductivity were determined [1].

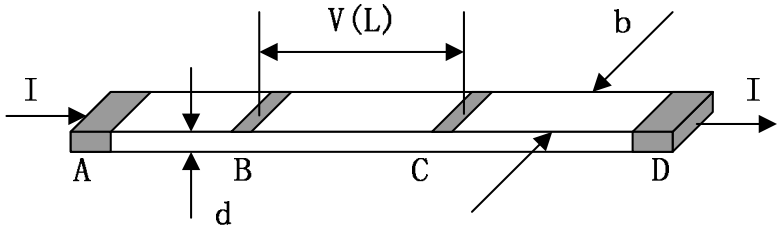

Figure 2: Scheme of the arrangement of four terminals for measurement of ionic conductivity along parallel direction

The ionic conductivity along parallel direction was evaluated by a simplified DC four-terminal method as shown in Figure 2 [1]. The ionic conductivity could be calculated by the following equation:

$$\sigma = \frac{1}{\rho} = \frac{I}{V} \cdot \frac{L}{b \cdot d}$$

Where I was the current of the circuit; V was the voltage between the two inner terminals; L was the distance between the outer terminals, b and d are the specific dimensions of the specimens. The free-standing specimens for this measurement had a size of 12 × 4 × 1 mm. The specimens were pasted with platinum glue in the four terminals and heated as in the case of circular specimens.

Alternative current (AC) impedance spectroscopy was used to examine the electrical properties of YSZ coating. McKubre [2] and Bauerle [3] reported that for a zirconia-based electrolyte with platinum electrodes, the individual polarizations of intragrain, intergrain, and electrode reaction interfaces could be distinguished in the impedance spectroscopy, as shown in Figure 3. Modeling of an equivalent circuit is important in AC analyses. This study adopted a series of R-C parallel circuits, which is generally employed [4,5]. The resistance values of the circuit elements were obtained from the intercepts on the x axis. Therefore, intragrain resistance (R_g) and intergrain / grain boundary resistance (R_{gb}) for each sample at prescribed test temperature could be gained easily. In this experiment, the impedance spectrum was

tested at temperatures from 600 to 1000°C at a frequency range of 0.1 Hz to 30 kHz, using a combined system of potentiostat/galvanostat and frequency response analyzer (FRA).

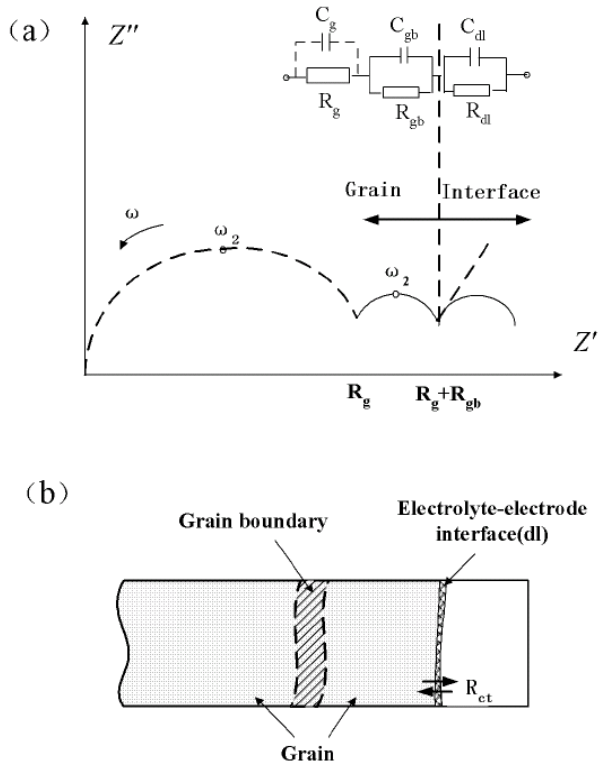

Figure 3: Schematic diagram of (a) AC impedance plot showing arcs due to three polarization processes and the adopted R-C equivalent circuit, (b) ion transport path in polycrystalline YSZ.

3.1.2 Ionic Conductivity of As-sprayed YSZ Coating

(1) Anisotropy of Ionic Conductivity

Figure 4 shows the ionic conductivity of YSZ coatings deposited with small size powder along both the parallel and perpendicular directions to coating surface, measured from 600 to 1000°C. The ionic conductivity increases with the increase of measurement temperatures. The ionic conductivity along perpendicular direction increases from 6.8×10^{-4} to 3.8×10^{-2} S/cm when the test temperature increases from 600 °C to 1000°C. Meanwhile, the ionic conductivity along the parallel direction

increases from 1.4×10^{-3} to 7.3×10^{-2} S/cm with the corresponding temperature increment, which is about twice higher than that along perpendicular direction.

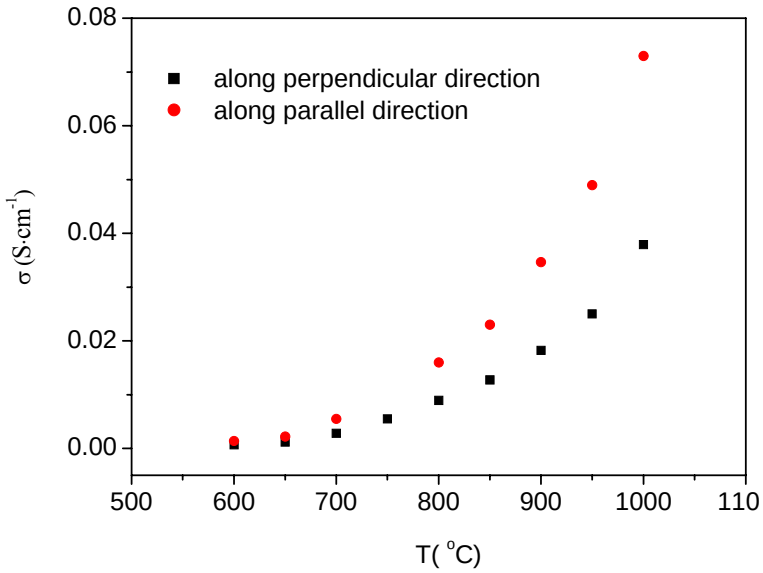

Figure 4: Effect of measuring direction on the ionic conductivity of the YSZ coating.

From the results reported by Yamamoto [6] and Ivers-Tiffee et al. [7], YSZ bulk shows an ionic conductivity of 0.16 S/cm at 1000°C. The previous investigations have shown that, in perpendicular direction, the electrical conductivity of LSM [8] and ionic conductivity of YSZ [9] coatings deposited by APS were one-fifth to one-third of corresponding bulk materials. Then, the result obtained in this study is consistent with the previous findings. This can be attributed to the poor contact between lamella. Due to poor interlamellar contacts, the bonding ratio between lamellae (defined as the ratio of bonded interface area to apparent total interface area) was found to be only 32% for plasma-sprayed ceramic coating [10,11]. This feature is the main reason for the reduced coating ionic conductivity along perpendicular direction compared to that of bulk materials prepared with sintering method. In the parallel direction, the ionic conductivity is still less than that of bulk materials. This can mainly be attributed to the vertical cracks appearing in plasma-sprayed YSZ coating.

(2) Influence of Composition on Ionic Conductivity

Figure 5 shows the ionic conductivity of the 4.5 mol% yttria stabilized zirconia

(PSZ) and 8 mol% yttria stabilized zirconia (YSZ) coatings at different temperatures along the perpendicular direction. The ionic conductivity of PSZ increases from 4.2×10^{-4} to 2.3×10^{-2} S/cm, which was much smaller than that of YSZ at the corresponding temperature. At the studied temperatures, the ionic conductivity of YSZ coating is about 50% higher than that of PSZ coating.

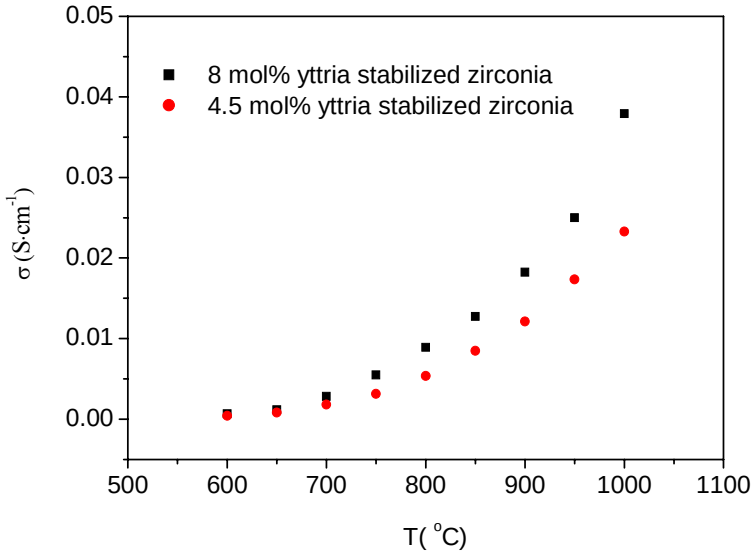

Figure 5: Effect of composition on the ionic conductivity of the YSZ coating.

(3) Influence of Powder Size on Ionic Conductivity

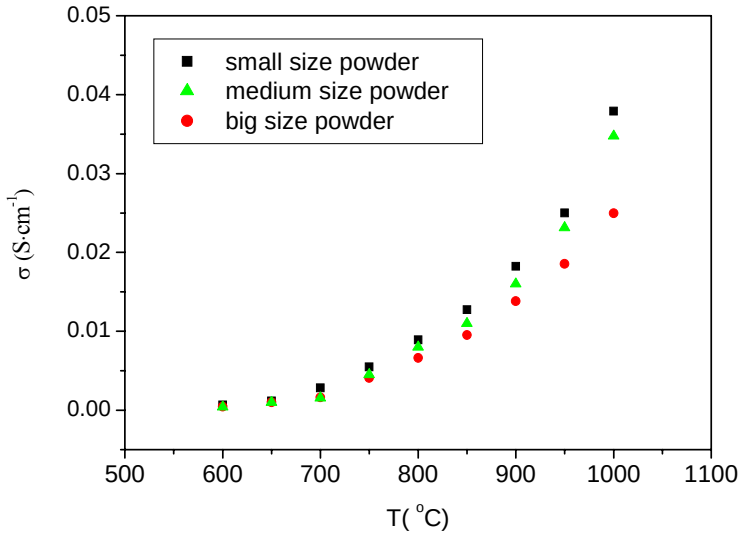

Figure 6: Effect of powder size on the ionic conductivity of the YSZ coating.

The ionic conductivity of coating deposited with different powders was measured. The ionic conductivity of the coating deposited with the small size powder shows the highest value at the measurement temperature range. For example, the ionic conductivity of the coating sprayed with the small powder at 1000°C is 0.038 S/cm. Meanwhile, the coating deposited with the big powder is only 0.022 S/cm and the coating deposited with the medium power is 0.034 S/cm. Considering the facts of these three pure YSZ powders, it could be deduced that the coating microstructure has a strong influence on ionic conductivity.

(4) Influence of Particle Temperature on Ionic Conductivity

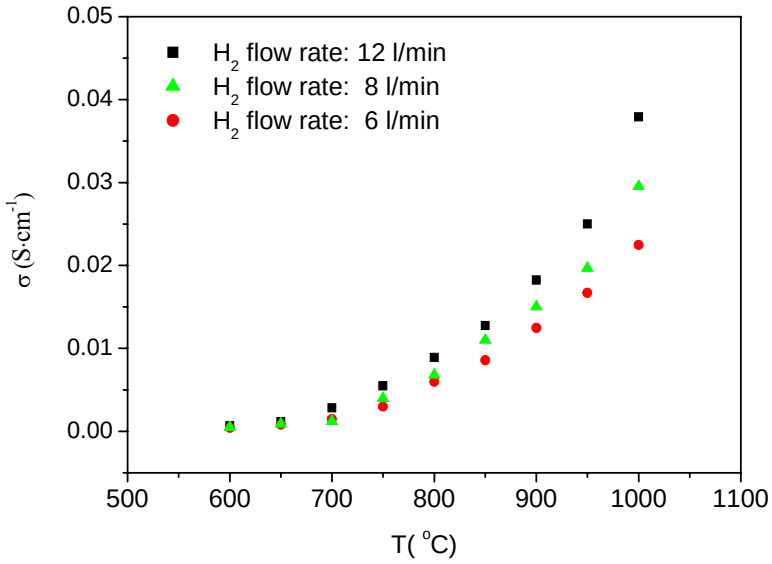

Figure 7: Effect of particle temperature on ionic conductivity of the YSZ coating.

The ionic conductivity of coatings deposited with different H_2 flow rates was measured. The Figure 7 shows that the coating deposited with the highest H_2 flow rate exhibits the highest ionic conductivity. The percentage of H_2 in the mixture being related to the thermal energy of the plasma jet, which means that coating deposited with high temperature particles shows high ionic conductivity. The difference of ionic conductivity could be ascribed to the difference of coating microstructure, which was discussed in section 2.3.2(2)-(ii).

(5) Influence of Particle Velocity on Ionic Conductivity

Figure 8 shows the ionic conductivity of the coatings deposited with different helium flows of 0 and 50 l/min, varying between 500 and 1000°C. The ionic conductivities of the two coatings are almost comparable. The ionic conductivity of 50 l/min He sample was 0.036 S/cm at temperature of 1000°C, while the value of coating without He was 0.035 S/cm at the same temperature. The similar ionic conductivity of the two coatings indicates that the in-flight particle velocity has little influence on the bonding condition of plasma-sprayed coating. However, it should be noted that the coating gas tightness is significantly influenced by in-flight particle velocity, which will be shown and discussed in the next chapter.

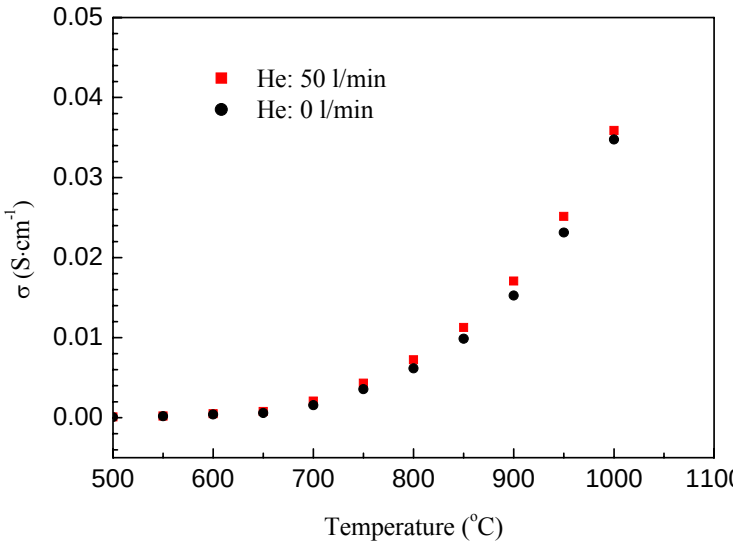

Figure 8: Effect of particle velocity on the electrical conductivity of the plasma-sprayed YSZ coating by DC approach.

(6) Ionic Conductivity of LPPS YSZ Coating

Figure 9 shows the evolution of the ionic conductivity of the LPPS and APS specimens versus temperature. The ionic conductivity of the LPPS coatings is a little higher than that of APS coatings. The ionic conductivity of LPPS sample is 0.043 S/cm at a temperature of 1000°C. The value of APS sample is 0.038 S/cm at the same

temperature. This fact indicates that the ionic conductivity of LPPS coating is improved by 20% at 1000°C compared with APS YSZ coatings. However, it should be noted that the LPPS coating was deposited on a pre-heated substrate, which was heated to 600°C before spraying. The work by Xing et al. [12] suggested that the temperature of substrate has a positive influence on coating ionic conductivity. If there is no pre-treatment for LPPS coating, the difference of APS and LPPS coatings may be even smaller. The LPPS YSZ coating shows the same lamellar structure to APS YSZ coating. The ionic conductivity of LPPS coating is also limited by the bonding characteristic between lamella as that of APS coating.

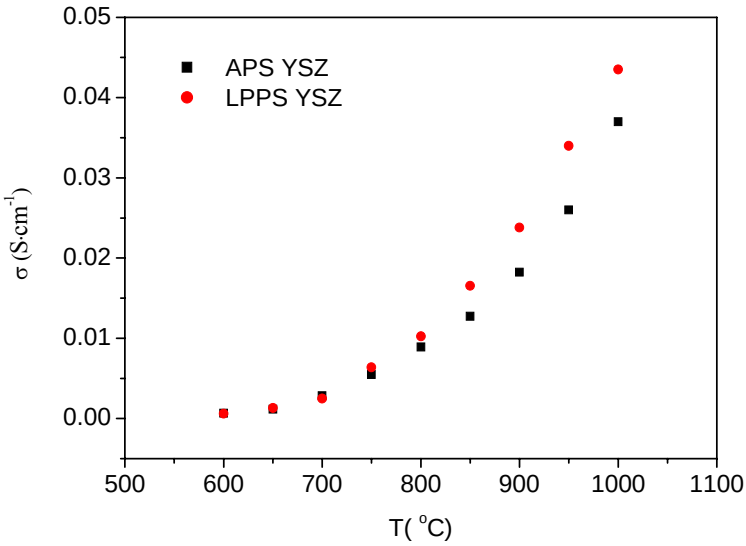

Figure 9: Ionic conductivity of LPPS YSZ compared to the APS YSZ coating.

3.2 Temperature Dependence

The temperature-dependence of the ionic conductivity of zirconia-based electrolytes has been investigated extensively. The traditional Arrhenius equation [13] is usually adopted to analyze the measured conductivity data,

$$\sigma = \frac{\sigma_0}{T}\exp\left(-\frac{E}{kT}\right) \qquad (1)$$

$$\ln \sigma T = \ln \sigma_0 - \frac{E}{kT} \qquad (2)$$

where E is the activation energy for ionic conduction, σ_0 is a material constant and k is Boltzmann constant. A linear relationship between $\log \sigma T$ and $\frac{1}{T}$, can be predicted by this equation.

Figure 10 shows the results of σT as a function of 1/T for the PSZ and YSZ electrolytes. It can be seen from Figure 10 that the Arrhenius plots shows curvatures at about 700°C and the activation energy at low temperature was greater than that at high temperature. A commonly accepted method to study the non-linear Arrhenius behavior is to fit the experimental data by two separate straight lines in both the low and the high temperature ranges.

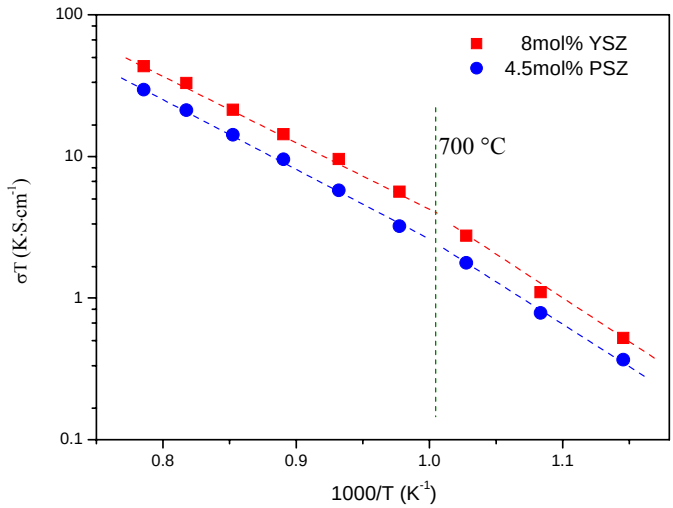

Figure 10: Arrhenius relation of σT and 1000/T for the 4.5 mol% PSZ and 8 mol% YSZ specimens, where σ was conductivity along the perpendicular direction.

Generally, there are two models to interpret the non-linear Arrhenius behavior of zirconia based electrolyte, referred to intragrain-intergrain conductivity model and dissociation-migration energy model in this paper.

As far as intragrain-intergrain conductivity model is concerned, the non-linear Arrhenius behavior is attributed to the change in ionic conductivity dominance from

intergrain conductivity at low temperature to intragrain conductivity at high temperatures [14]. At high temperature, the contribution of intergrain conductivity is less important in the total conductivity than the intragrain conductivity, whereas, the intergrain conductivity plays a key role in the ionic conductivity at a low temperature. Some investigators indicated [15-18] that the electrical performance of zirconia based electrolyte can be significantly improved at lower temperatures by the reduction of grain-boundary resistance, e.g., through controlling the impurity phase and the size of grain.

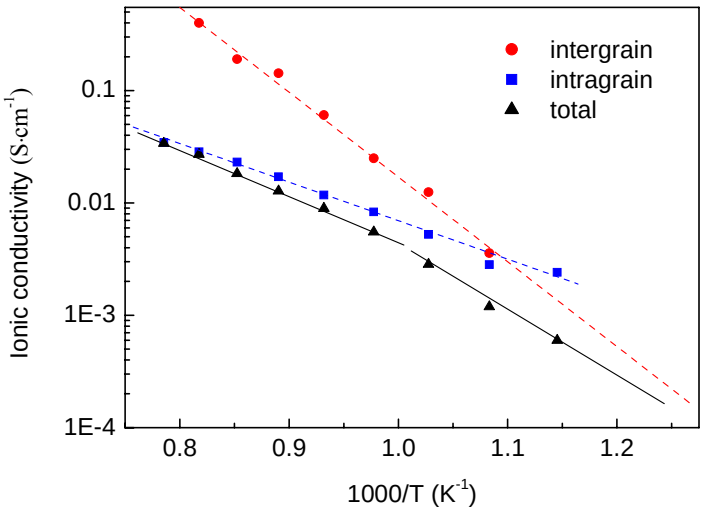

Figure 11: Temperature dependence of the intragrain conductivity and intergrain conductivity of YSZ along the perpendicular direction resolved by AC impedance technique. Solid line was the total conductivity (attributed to the sum of intragrain and intergrain resistance) determined by DC measurement.

In this study, the data of intergrain and intragrain conductivity are resolved from an AC impedance spectroscopy, as shown in Figure 11. It could be noticed that the total conductivity is close to the intragrain conductivity at high temperature and approaches to the intergrain conductivity at low temperature. Using the intragrain-intergrain conductivity model, this phenomenon could be explained by the change of the dominance of ionic conductivity. However, it is very interesting to point out that the non-linear Arrhenius behavior has also been observed in the monocrystalline YSZ electrolytes [19-22]. In these studies, the evolution of ionic

conductivity, as function of temperature, exhibits a curvature in slope around 650^{o}C for the monocrystalline YSZ electrolytes as in the case of polycrystalline YSZ electrolyte. According to the intragrain-intergrain conductivity model, for a monocrystal, without grain boundary, there should be no curvature in the slope. It seems that, in the case of monocrystalline YSZ electrolyte, the intragrain-intergrain conductivity model encounters great challenges for explaining its non-linear Arrhenius behavior.

It is well known that the doping of ZrO_2 with Y_2O_3 results in the substitution incorporation of Y^{3+} on the Zr^{4+} cation sublattice with the concomitant formation of oxygen vacancies as charge compensating defects. The defect formation reaction can be written in Kroger and Vink notation as:

$$Y_2O_3 + 2Zr_{Zr}^{\times} + O_o^{\times} \longrightarrow 2Y_{Zr}^{'} + V_o^{\bullet\bullet} + 2ZrO_2 \qquad (3)$$

Due to Coulombic and elastic attractive forces between $Y_{Zr}^{'}$ and $V_o^{\bullet\bullet}$, the formation of defects associates as:

$$Y_{Zr}^{'} + V_o^{\bullet\bullet} \longrightarrow (Y_{Zr}^{'}V_o^{\bullet\bullet}) \qquad (4)$$

and

$$2Y_{Zr}^{'} + V_o^{\bullet\bullet} \longrightarrow (2Y_{Zr}^{'}V_o^{\bullet\bullet}) \qquad (5)$$

The formation of defects associates binds some oxygen vacancies to yttrium ions, making the oxygen vacancies unavailable for conduction. Manning et al. [19] suggested that $Y_{Zr}^{'}V_o^{\bullet\bullet}$ was more likely to occur because of the expected random distribution of $Y_{Zr}^{'}$.

For the YSZ electrolyte, the oxygen vacancies exists as two ways: $Y_{Zr}^{'}V_o^{\bullet\bullet}$ and $V_o^{\bullet\bullet}$. As the thermal dissociation of $Y_{Zr}^{'}V_o^{\bullet\bullet}$ requires a supplemental energy to free

oxygen vacancies from the defect association $Y'_{Zr}V_o^{\bullet\bullet}$, the activation energy thus consists of disassociation energy E_a, and migration energy E_m. At a high temperature range, it is usually assumed that all the oxygen vacancies are free and the activation energy reflects only the migration energy E_m for the oxygen vacancies.

Table 1: Activation energy of YSZ electrolyte in different temperatures

	Activation energy E(eV)	
	600-700°C	700-1000 °C
YSZ	1.14	0.85
PSZ	1.05	0.89

Table 1 shows the activation energy of APS PSZ and YSZ electrolytes, respectively. Although the ionic conductivity of APS YSZ coating was about one-fourth of that of the bulk material, the experimental results showed that the activation energy is similar to those of bulk materials which would be discussed below. This suggests that the ionic transport mechanism of APS YSZ electrolyte coating is the same as that of the bulk materials.

For the YSZ, the activation energies are 1.14 and 0.85 eV, respectively, at the temperature ranges of both lower and higher than 700°C. These results are consistent with those obtained by Madani et al. [21] and Gong et al. [23]. Madani reported that the 9.5 mol% monocrystalline YSZ exhibited the activation energies of 1.08 and 0.87 eV, respectively, in the two temperature ranges. Similarly, Gong et al. found that increasing the temperature higher than 650°C, the activation energies of polycrystalline YSZ were decreased from 1.19 to 0.91 eV. The slight differences between the values of activation energy can be attributed to the different yttria contents and experimental errors. Moreover, in Filal's study [20], it was indicated that, for the poorly doped samples (<3 mol% Y_2O_3) and highly doped samples (>17.5 mol% Y_2O_3), the activation energy was not variable with the dopant concentration. For the higher concentration of Y_2O_3, the amount of oxygen vacancies and Y^{3+} ions on Z^{4+} sites are high enough to generate the formation of dopant-vacancy associations

over the whole temperature range and the activation energy was constant to the E_a+E_m. For the lower concentration of Y_2O_3, the amount of oxygen vacancies was not large enough for the concentration of complex defects to be significant and the activation energy was constant close to E_m. On the other hand, this result was another evidence to show the limitation of intragrain-intergrain conductivity model. With the assumption that the intragrain-intergrain model was reasonable, no matter what the concentration of the dopant Y_2O_3 was adopted in the electrolyte, the non-linear Arrhenius phenomenon should appear which was not emerged in the experiments.

The activation of YSZ electrolytes at high temperature range was similar to that of PSZ electrolyte in Table 1. As aforementioned, in the high temperature range, the activation energy reflects the migration energy E_m for the oxygen vacancies. As described in the literature [24], the migration energy, E_m, was the required energy for O^{2-} ion displace across a saddle point in a diffusion path. When the yttria concentration was above 10 mol% [25], the increase in the lattice parameter due to the increase of yttria content leads the increase of ionic spacing, which consequently interferes with the difficult migration of O^{2-}. As a result, E_m becomes large as the number of Y^{3+} ions increases. In the concentration range from 4 to 10 mol%, corresponding to this study, the lattice parameter was nearly independent of the yttria concentration [25]. As a result, it was reasonable to conclude that the E_m was similar for 4.5 mol% PSZ and 8 mol% YSZ coatings.

It can also be deduced from Table 1 that, the E_a was 0.29 eV for the YSZ electrolytes. This result was comparable to the theoretically one, which was 0.28 eV [26]. For PSZ electrolytes, however, the E_a was only 0.16 eV. This can be related to the smaller amount of oxygen vacancies. As a result, less $Y'_{Zr}V_o^{\bullet\bullet}$ was formed and led to a lower E_a for 4.5 mol% YSZ, in the lower temperature range.

3.3 Microwave Sintering of Plasma-sprayed YSZ Coating

Due to the lamellar structure and limited bonding characteristic between lamellae, as-sprayed coating always exhibits decreased electrical properties. The previous studies indicate that the ionic conductivity of APS and LPPS YSZ electrolyte coating are about one-fifth to one-fourth of the bulk YSZ electrolyte. In order to improve the coating electrical performance, some post-treatment techniques were developed by means of conventional heat sintering [27], chemical solution densification technique [9,28] and spark plasma sintering technique [29,30].

3.3.1 Introduction of Microwave Sintering

Microwave (MW) sintering is a relatively new technique employed for the sintering of ceramics. The most advantage of MW sintering is the volume heating and thereby, a uniform and rapid sintering is possible [31]. Additionally, compared with conventional sintering process in which heating begins from material surface, MW sintering lowers thermomechanical stresses in materials due to more uniform heat distribution [32]. For a given material, the power absorbed per unit volume could be calculated as follow [33]:

$$P = 2\pi f \xi_0 \xi'' |E|^2 = 2\pi f \xi_0 \xi_r' \tan\delta |E|^2 \qquad (6)$$

where E is the magnitude of the internal electrical field, ξ'' is the relative effective dielectric factor, ξ_0 is the permittivity of free space, f is the microwave frequency, ξ_r' is the relative dielectric constant, and $\tan\delta$ is the energy loss required to store a given quantity of energy. Product of $\xi_0\xi''$ (or $\xi_0\xi_r' \tan\delta$) is called dielectric loss factor. The dielectric loss factor determines the material coupling property, according to that materials can be classified into: transparent (low dielectric loss materials) - MW passes through with little, if any, attenuation; opaque (conductors) - MW is

reflected and does not penetrate; and, absorbing (high dielectric loss materials) - absorb MW energy is absorbed to a certain degree based on the value of dielectric loss factor [32].

In general term, most ceramics have a low dielectric loss factor or are transparent to MW radiation. When a low dielectric loss factor material is subject to MW radiation, it may be heated up slowly and this can lead to a plasma formation in the cavity [31]. One solution for this problem is to use a susceptor installed together with the low dielectric loss factor material in the MW cavity [31-34]. Correspondingly, the heating mechanism is a combination of microwave heating and conventional heating by the filled susceptor. $BaTiO_3$ is an ideal candidate material for MW susceptor because of its high loss factors. The thermal properties and dielectric loss factor of $BaTiO_3$ and ZrO_2 is shown in Table 2 [31]. It is clearly seen that $BaTiO_3$ is a good MW suspector candidate.

Table 2: Thermal properties of $BaTiO_3$ and ZrO_2

	Specific heat(J/g)	Thermal conductivity (W/m K)	Dielectric loss factor (2.45 GHz)	
	1000℃	1000℃	25℃	1000℃
$BaTiO_3$	0.59	2.2-3.2	180	>180
ZrO_2	0.64	2.2	0.0034	0.053

The investigations on MW sintering ceramic are very active in recent years. However, most of the previous efforts contribute to the sintering of bulk materials [35-37]. Microwave sintering of plasma-sprayed YSZ electrolyte coatings was not reported before. In this section, the feasibility of MW sintering on APS YSZ electrolyte coating is studied. Considering the low dielectric factor of YSZ, $BaTiO_3$ powders were incorporated into the YSZ powders to deposit composite coatings. $BaTiO_3$ was chosen as a MW suspector material due to its high dielectric loss factor and its excellent decomposition resistance as well. The later characteristic was very important for plasma spraying process in which the feedstock materials are subjected to a high temperature plasma flow. The as-sprayed YSZ and $BaTiO_3$-YSZ composite

coatings were sintered using a MW furnace, respectively. The influence of $BaTiO_3$ and its content on the sintering efficiency, coating structure and ionic conductivity were investigated.

3.3.2 Feedstock Materials and Coating Preparation

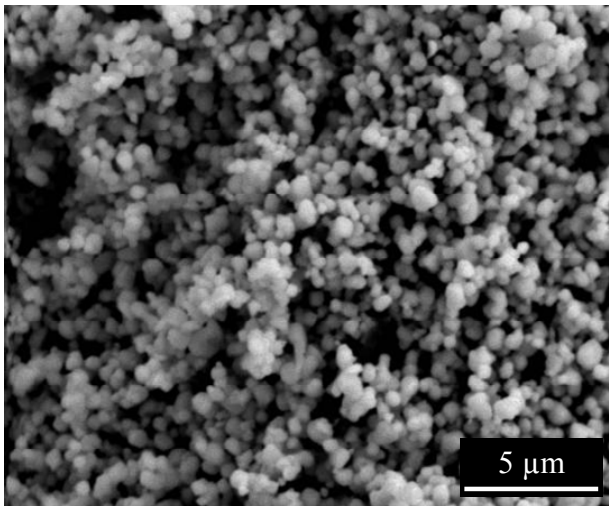

Figure 12: SEM powder morphologies of $BaTiO_3$.

Medium size YSZ and $BaTiO_3$ powder were used as feedstock materials for as-sprayed coatings. $BaTiO_3$ powders (Inframat, USA) had an average diameter of about 0.7 μm. The morphology of this powder is shown in Figure 12. Generally, only the powders with a diameter in the distribution of 5-100 μm could be used as feedstock for plasma spraying process. In order to increase the flowability of the fine powders, the small $BaTiO_3$ powders were agglomerated with 5% PVA solution and were finally meshed to get a diameter range under 50 μm. Then, the powders were dried in a furnace at 200°C for 2 hours. The obtained agglomerated $BaTiO_3$ powders were incorporated into the YSZ powders with 5% and 10% (weight ratio) contents, respectively. The mixed powders were mechanically blended in 20 minutes to get a homogenous mixture.

Three types of coatings, pure YSZ, 5wt.%$BaTiO_3$-YSZ and 10wt.%$BaTiO_3$-YSZ, were deposited. The square free-standing coatings were positioned in a microwave

sintering system (MW720, Püschner, Germany). The outline and inner structures of the microwave power system were shown in Figure 13. In this work, sintering process was performed under an ambient pressure in air. Three 2.45 GHz microwave generators were adopted simultaneously to get a homogenous microwave field in the cavity. Power of three generators was respectively 3000, 3000 and 1200 W. Coating surface temperature was measured by an infrared camera and was recorded dynamically to a computer.

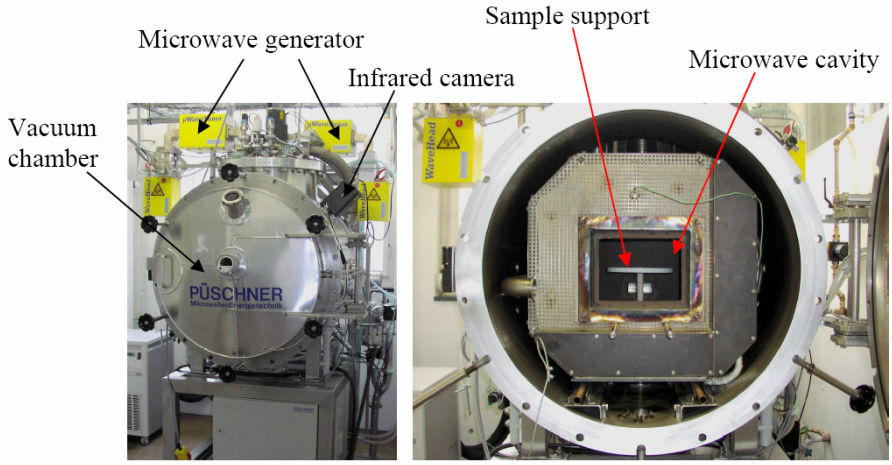

Figure 13: Outline and inner structures of the microwave sintering system.

3.3.3 Microstructure of As-sprayed Coating

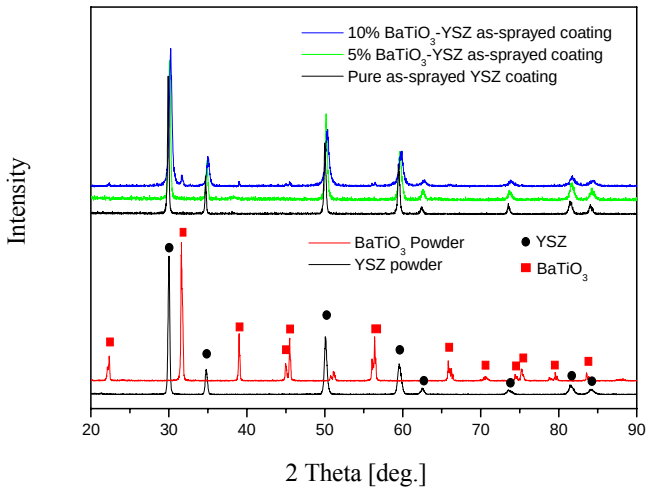

Figure 14: XRD patterns of pure YSZ, 5wt.%$BaTiO_3$-YSZ, 10wt.%$BaTiO_3$-YSZ as-sprayed coatings with YSZ and $BaTiO_3$ powders.

Figure 14 shows the XRD patterns of the as-sprayed coatings and the starting powder. Being consistent with the starting powder, YSZ coating consists of well-crystallized single cubic zirconia phase. For 5wt.% $BaTiO_3$-YSZ coating, no obvious $BaTiO_3$ peak was found. This maybe ascribed to the low content of $BaTiO_3$, since it is difficult to determine a low content phase (less than 5%) in composite materials. Comparatively, $BaTiO_3$ peaks are clearly shown in the XRD pattern of 10wt.% $BaTiO_3$-YSZ coating. Clearly, all the peaks in 10wt.% $BaTiO_3$-YSZ coating correspond to those in the $BaTiO_3$ and YSZ powders. This indicates that no phase transformation occurs during the plasma spraying process.

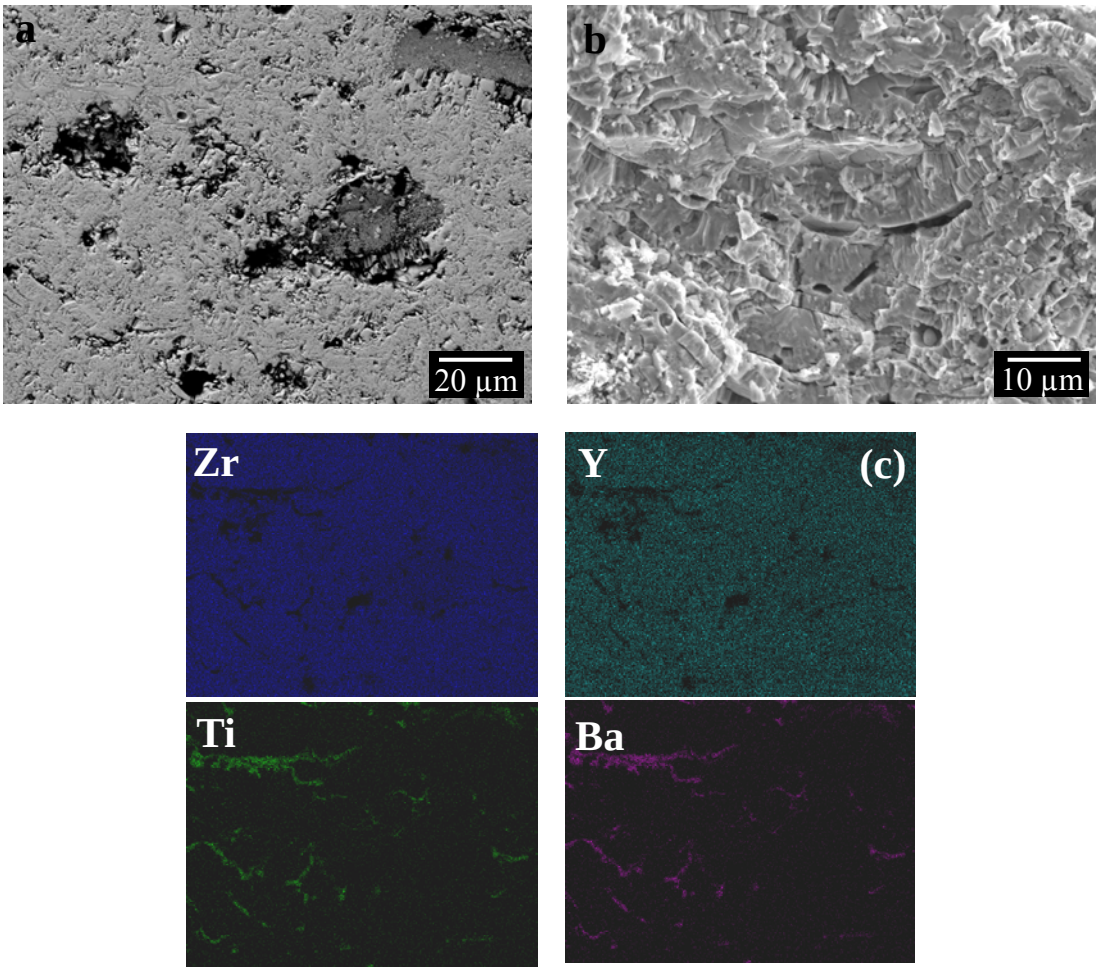

Figure 15: SEM polished cross-section microstructure (a), SEM fractured cross-section microstructure (b), polished surface EDS chemical mapping analysis(c).

Figure 15(a) and 15(b) show polished and fractured cross-sectional structures of

5wt.%$BaTiO_3$-YSZ as-sprayed coating. Being like the pure YSZ coating, the composite coating also has a lamellar microstructure. Figure 15(c) gives the distributions of the elements Zr, Y, Ti, Ba determined by the EDS chemical mapping analysis of the composite coating. The distribution of Ba shows that the $BaTiO_3$ was well melted and flatted during the spraying process.

3.3.4 MW Sintering

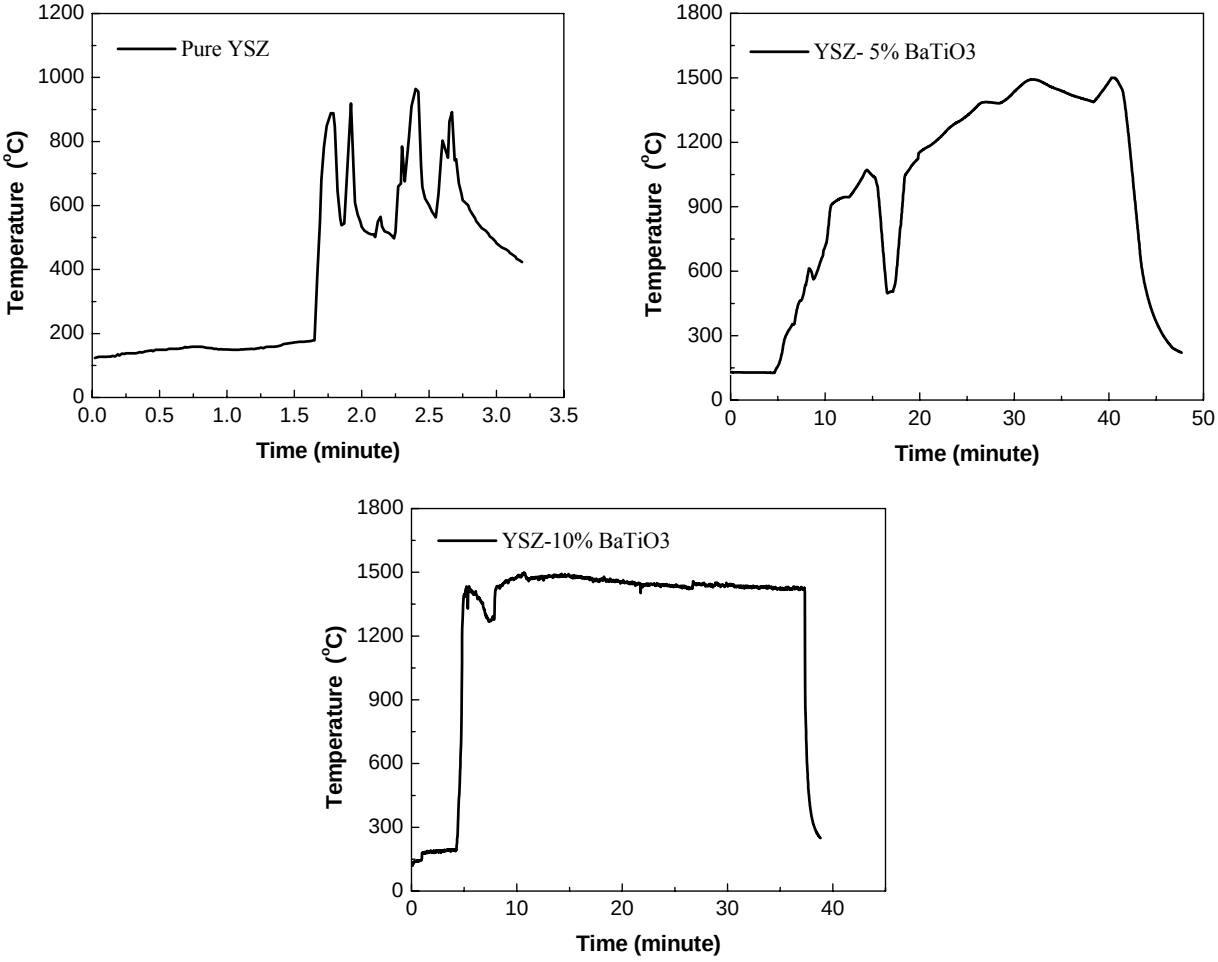

Figure 16: Temperature recording of pure YSZ (a), 5wt.%$BaTiO_3$-YSZ (b), 10wt.%$BaTiO_3$-YSZ (c) coating surfaces during MW heating.

The three types of free-standing coatings are sintered in the microwave sintering system. Figure 16(a) shows heating curve of pure YSZ coating during MW sintering. The pure YSZ coating can only be heated to less than 900°C. The limited heating

efficiency is attributed to the low dielectric loss factor of pure YSZ material. Regardless the significant increase of the dielectric loss factor when increasing temperature, even at a temperature of 1000°C, the factor of YSZ is still very low (0.053 [31]). During MW heating process, much MW energy was absorbed by the atmosphere instead of the YSZ sample. This results in a plasma formation in the cavity. Additionally, a heat transfer occurs between the sample and the environment. When the thermal energy loss by heat transfer becomes equal to the energy evolved in the sample through absorption of MW radiation, the coating temperature could not be further elevated.

Compared with pure YSZ coating, 5wt.%$BaTiO_3$-YSZ and 10wt.% $BaTiO_3$-YSZ coatings can be heated to 1450°C rapidly. As seen from the comparison between Figure 16(b) and 6(c), an increase in $BaTiO_3$ content leads to a higher heating efficiency of the coating. Moreover, as marked in Figure 16(b), a fluctuation is observed on the heating curve. This may be caused by plasma formation during the early stage of microwave sintering of 5wt.%$BaTiO_3$-YSZ coating. In high temperature region, there is no fluctuation found on the heating curve. As aforementioned, in the high temperature range, the composite coating has a higher dielectric loss factor and this may be the reason why no plasma formation exists in late stage.

For the composite coatings, the sintering of YSZ matrix can be considered as a hybrid heating: by traditional heat transfer and by MW radiation. During MW sintering process, $BaTiO_3$ phase is heated preferentially and presents a higher temperature than YSZ matrix. As a result, $BaTiO_3$ can be regarded as traditional thermal sources for the YSZ matrix and therefore heat transfer from the $BaTiO_3$ particles to the matrix occurs. If the heat exchange between the sample and the environment is not considered, the following equation can be obtained:

$$\frac{dT}{dt} = \frac{PV - Q_e}{\rho VC} = \frac{2\pi f \xi_0 \xi'' |E|^2 V - Q_e}{\rho VC} \qquad (7)$$

where Q_e is the heat transfer from the $BaTiO_3$ to YSZ materials by means of thermal conduction, heat radiation and convection; T is the temperature of $BaTiO_3$ and t is the time; ρ and C represent respectively the mass density and the heat capacity of $BaTiO_3$; V is the volume of $BaTiO_3$ phase.

3.3.5 Microstructure of MW-sintered Coatings

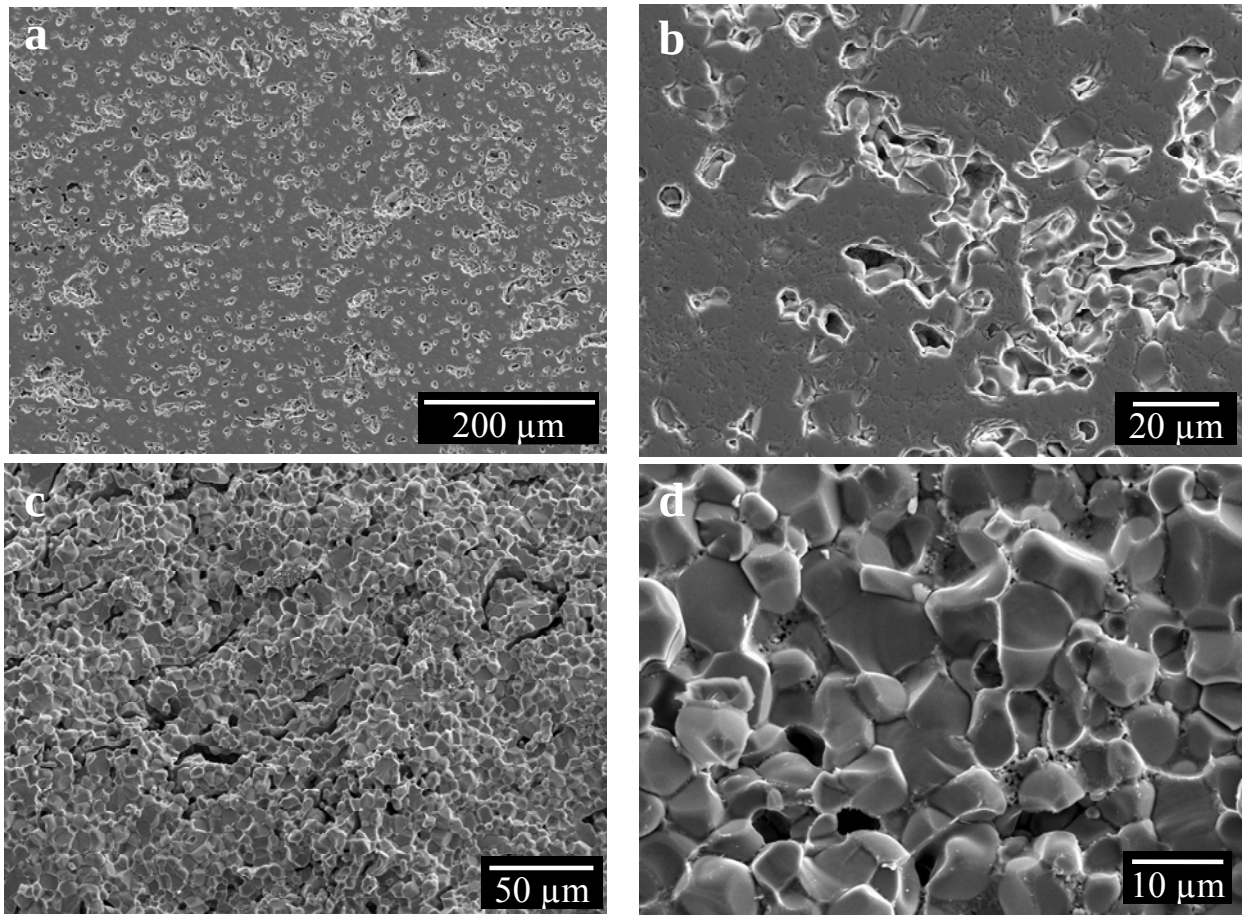

Figure 17: SEM polished cross-section (a-b) and fractured cross-section (c-d) microstructure of 5wt.%$BaTiO_3$-YSZ MW sintered coating.

Figure 17(a) and (b) show polished cross-sectional microstructure of MW-sintered 5wt.%$BaTiO_3$-YSZ composite coatings taken at a low and high magnifications. The sintered coating exhibits a distinct microstructure from that of the as-sprayed coating. Figure 17(c) and (d) show the fractured microstructure of the sintered coating. It is clearly observed that the sintered coating shows equiax crystal

structure, which is very different from the lamellar structure of the as-sprayed coating. Pores are apparent between the equiax crystals. After MW sintering, intrinsic features of as-sprayed YSZ coating, such as non-bonded interface and vertical (intralamellar) cracks, have disappeared. The structural modification has a significant effect on coating ionic conductivity. This will be discussed in another section.

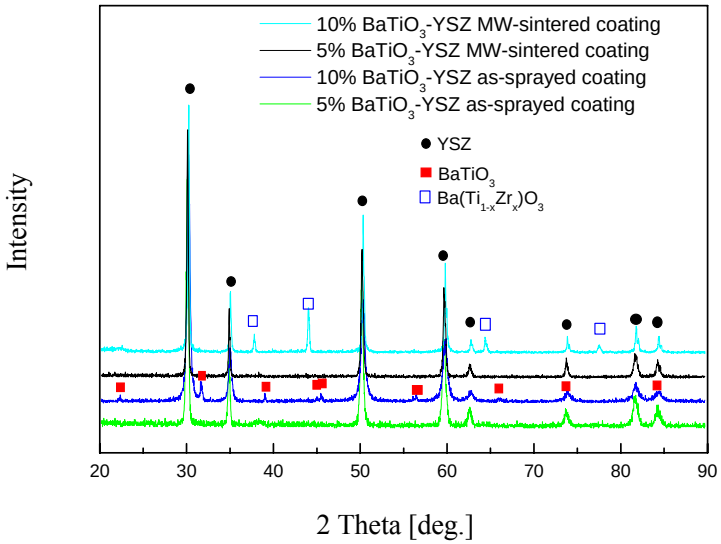

Figure 18: XRD patterns of 5wt.%$BaTiO_3$-YSZ and 10wt.%$BaTiO_3$-YSZ MW-sintered coatings with their as-sprayed coatings.

Figure 18 shows XRD patterns of MW-sintered 5wt.%$BaTiO_3$-YSZ and 10wt.%$BaTiO_3$-YSZ composite coatings compared with the as-sprayed coatings. Only YSZ phase was detected in the XRD patterns in both the as-sprayed and MW-sintered 5wt.%$BaTiO_3$-YSZ coatings due to the low $BaTiO_3$ content. With respect to the 10wt.% $BaTiO_3$-YSZ coatings, $BaTiO_3$ and YSZ phases are clearly noticed in the XRD patterns of the as-sprayed and sintered coatings. However, it should be noted that a new phase $Ba(Ti_{1-x}Zr_x)O_3$ is apparent in the MW sintered coating. The substitution of Ti^{4+} in $BaTiO_3$ with Zr^{4+} in YSZ is completed during sintering process, which is confirmed by XRD and Raman spectroscopy in other study [38].

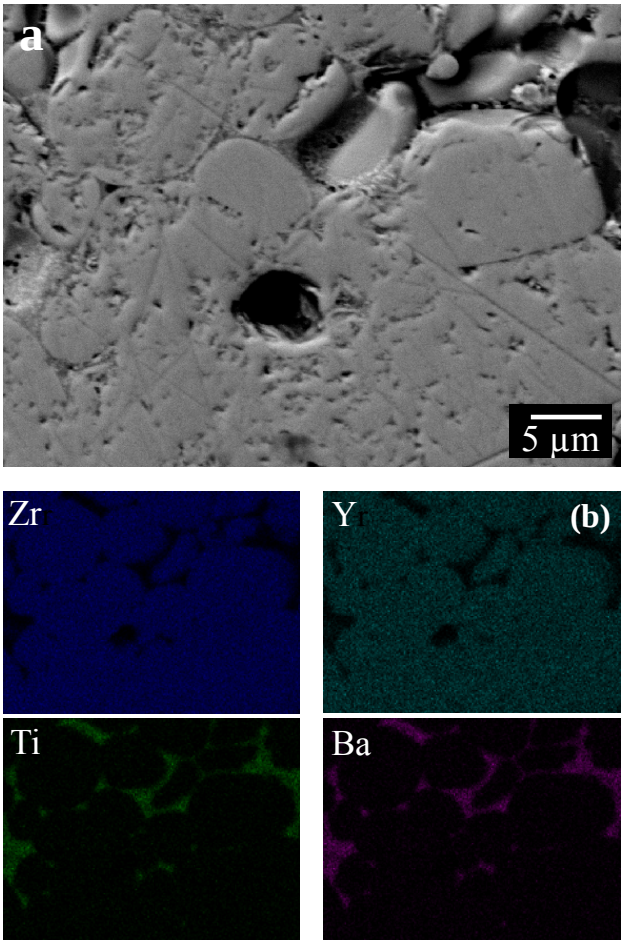

Figure 19: EDS chemical mapping analysis of polished cross-section surface of 5wt.%$BaTiO_3$-YSZ MW-sintered coating.

An EDS chemical mapping analysis of the MW-sintered 10wt.%$BaTiO_3$-YSZ coating is conducted as shown in Figure 19. Interestingly, compared with Fig.5(c), an aliquation of $BaTiO_3$ ($Ba(Ti_{1-x}Zr_x)O_3$) phase occurs and $BaTiO_3$ ($Ba(Ti_{1-x}Zr_x)O_3$) phase tends to assemble in the interface of equaix crystals. This can be attributed to the distinct difference of the melting points of the two materials (1640 and 2700^{o}C for $BaTiO_3$ and YSZ, respectively).

3.3.6 Modification of Ionic Conductivity

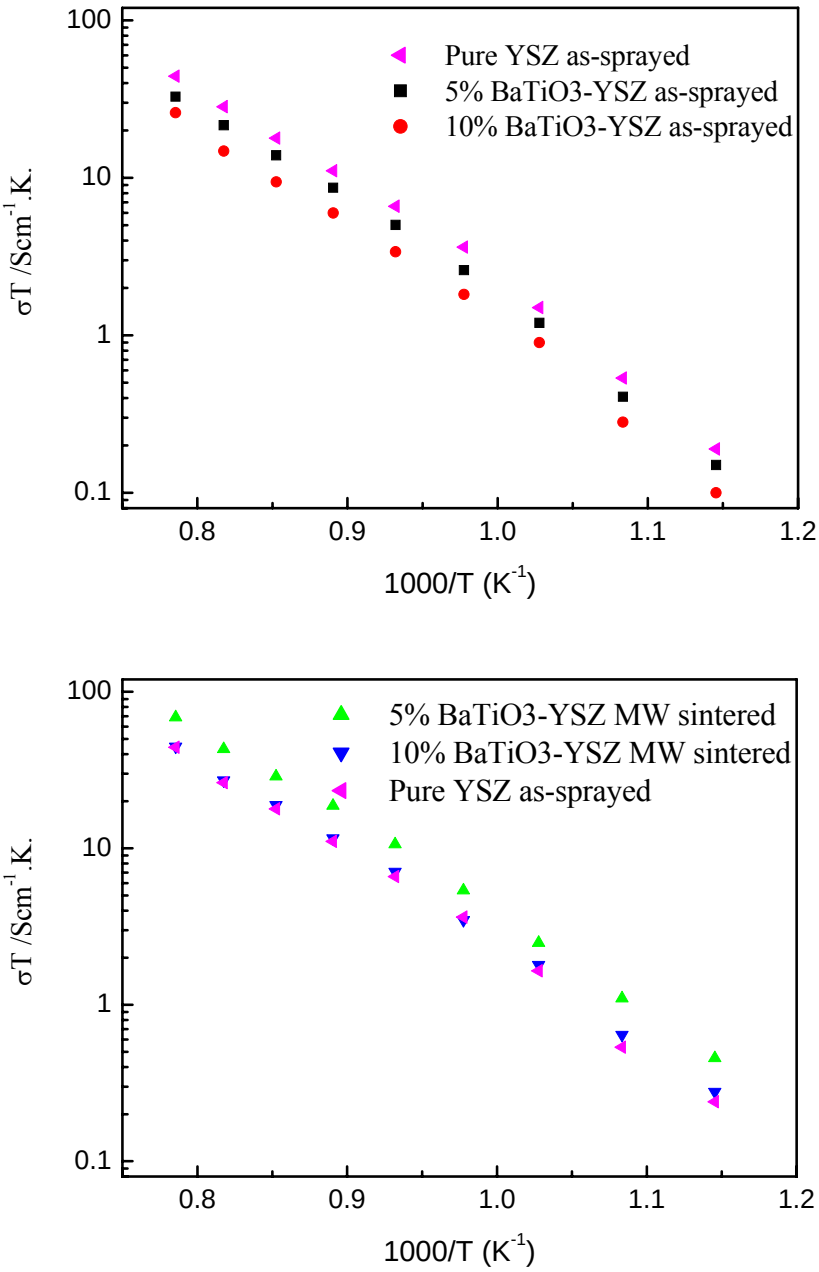

Figure 20: Arrhenius relation of σT and 1000 T^{-1} for the YSZ, 5wt.%$BaTiO_3$-YSZ and 10wt.%$BaTiO_3$-YSZ as-sprayed coatings and MW sintered coating.

Figure 20(a) shows the ionic conductivities of the three as-sprayed coatings measured from 600 to 1000°C. The ionic conductivity of pure YSZ as-sprayed sample is 0.035 Scm^{-1} at 1000°C. $BaTiO_3$, as an insulator in the composite coating, interrupts

the oxygen ionic conduction in YSZ matrix and consequently decreases the coating ionic conductivity. It can be found that ionic conductivity of the as-sprayed 5wt.%$BaTiO_3$-YSZ and 10wt.% $BaTiO_3$-YSZ samples were 0.0258 and 0.0203 scm^{-1} at 1000°C, respectively.

Figure 20(b) shows the ionic conductivity of MW-sintered 5wt.%$BaTiO_3$-YSZ and 10wt.%$BaTiO_3$-YSZ coatings compared to those of the as-sprayed pure YSZ coatings. After MW sintering, the ionic conductivities of the 5wt.%$BaTiO_3$-YSZ and 10wt.% $BaTiO_3$-YSZ coatings are enhanced to 0.054 and 0.035 Scm^{-1} at 1000^oC, respectively. These values are about one time higher than those of as-sprayed coatings. Compared with the pure YSZ coating, the MW-sintered 5wt.%$BaTiO_3$-YSZ coating exhibits a higher ionic conductivity by about 60%. The improvement of ionic conductivity is related to the structural modification after MW heating. After MW sintering, the lamellar microstructure is modified to equiax crystal. The bonding ratio between the lamellae is significantly improved and thus the ionic conductivity is increased. However, for the MW-sintered 10wt.%$BaTiO_3$-YSZ coating, the ionic conductivity is only comparable to the as-sprayed pure YSZ coating. As aforementioned, too much $BaTiO_3$ content can interrupt ionic conduction in YSZ matrix and restrict the improvement of ionic conductivity of composite coating.

3.4 Conclusions

For APS YSZ electrolytes, the ionic conductivity was determined by material composition and coating microstructure. The lamellar features of plasma-sprayed coating with limited lamellar interface bonding and vertical cracks led to the anisotropy of coating properties and the reduction of ionic conductivity. The ionic conductivity of all the as-sprayed YSZ coatings along the perpendicular direction was about one-fourth to the corresponding bulk electrolyte. The ionic conductivity in the parallel direction was about twice higher than that in perpendicular direction, which

can be attributed to lamellar microstructural feature of APS YSZ coatings.

The examination of the temperature dependence of ionic conductivity of APS YSZ electrolyte yielded non-linear Arrhenius behavior. The two frequently used models, intragrain-intergrain conductivity and the dissociation-migration energy model, were examined for explaining the non-linear characteristic. On the basis of the data reported in literature, the limitation of intragrain-intergrain conductivity model was evidenced. It is more reasonable to employ the dissociation-migration energy model to explain the temperature dependence of the obtained ionic conductivity of APS YSZ electrolyte.

The feasibility of MW sintering on APS YSZ coatings, with $BaTiO_3$ as MW susceptor, was investigated. APS YSZ coating can only be heated to less than 900℃ in the MW cavity due to its low dielectric loss factor, whereas the $BaTiO_3$-YSZ composite coating could be easily heated to 1450°C. For the $BaTiO_3$-YSZ composite coating, the $BaTiO_3$ particles were regarded as distributed heat sources in YSZ matrix. The lamellar structure of the as-sprayed $BaTiO_3$-YSZ composite coatings is modified to equiax crystal in MW-sintered coatings. $BaTiO_3$ is transformed to $Ba(Ti_{1-x}Zr_x)O_3$ during MW sintering process and assembled to the interface after MW sintering. Ionic conductivity of MW-sintered composite coatings was about one time higher than that of as-sprayed coatings. Compared with ionic conductivity of the pure YSZ coating, the MW-sintered 5wt.%$BaTiO_3$-YSZ coating presented a 60% higher conductivity.

3.5 Reference

[1] X.-J. Ning, Study on the fabrication of zirconia based electrolyte for SOFC by atmospheric plasma spraying, Dissertation of Xi'an Jiaotong University, 2005 (in Chinese).

[2] M.C.H. Mckubre, in: J.R. Macdonald (Ed.), Impedance Spectroscopy, Wiley-Interscience, New York, 1987.

[3] J.B. Bauerle, Study of solid electrolyte polarization by a complex admittance method, *J. Phys. Chem. Solids*, **30**(12) (1969), p. 2657-2670.

[4] H.S. Maiti and R.N. Basu, Complex-plane impedance analysis for semiconducting barium titanate, *Mater. Res. Bull*., **21**(9) (1986), p. 1107-1114.

[5] S. Kim, M.C. Chun, K.T. Lee, H.L. Lee, Oxygen-ion conductivity of BaO- and MgO-doped LaGaO3 electrolytes, *J. Power Sour.* **93**(1-2) (2001), p. 279-284.

[6] O. Yamamoto, Solid oxide fuel cells: fundamental aspects and prospects, *Electrochim. Acta*, **45**(15-16) (2000), p. 2423-2435

[7] E. Ivers-Tiffee, A. Weber, D. Herbstritt, Materials and technologies for SOFC-components, *J. Eur. Ceram. Soc*, **21**(10-11) (2001), p. 1805-1811.

[8] C.-J. Li, C.-X. Li and M. Wang, Effect of spray parameters on the electrical conductivity of plasma-sprayed $La_{1-x}Sr_xMnO_3$ coating for the cathode of SOFCs, *Surf. Coat. Techol*, **198**(1-3) (2005), p. 278-282.

[9] C.-J. Li, X.-J. Ning and C.-X. Li, Effect of densification processes on the properties of plasma-sprayed YSZ electrolyte coatings for solid oxide fuel cells, *Surf. Coat. Technol.* **190**(1) (2005), p. 60-64.

[10] A. Ohmori, C.-J. Li and Y. Arata, Influence of plasma spray conditions on the structure of Al_2O_3 coatings, *Trans. Jpn. Weld. Res. Inst.* **19** (1990), p. 259-270.

[11] A. Ohmori and C.-J. Li, Quantitative characterization of the structure of plasma sprayed Al_2O_3 coating by using copper electroplating, *Thin Solid Films* **201** (1991), p. 241-252.

[12] Y.-Z. Xing, C.-J. Li, C.-X. Li and G.-J. Yang, Influence of through-lamella grain growth on ionic conductivity of plasma-sprayed yttria-stabilized zirconia as an

electrolyte in solid oxide fuel cells, *J. Power Sources*, **176**(1) (2008), p. 31-38.

[13] Z.-X. Lin, Z.-K. Gun and C.-W. Sun, Rapid ion conductor-foundation, materials, application, Shanghai science technology press, Shanghai, 1983, p. 46-87 (in Chinese).

[13] I. Kosacki, H. U. Anderson, Y. Mizutani and K. Ukai, Nonstoichiometry and electrical transport in Sc-doped zirconia, *Solid State Ionics* **152-153** (2002), p. 431-438.

[14] R. Chiba, T. Ishiil and F. Yoshimura, Temperature dependence of ionic conductivity in (1-x)ZrO_2−(x-y)Sc_2O_3−yYb_2O_3 electrolyte material, *Solid State Ionics* **91**(3-4) (1996), p. 249-256.

[15] M. Aoki, Y.M. Chiang, I. Kosacki, L.J. Lee, H.L. Tuller and Y. Liu, Solute Segregation and Grain-Boundary Impedance in High-Purity Stabilized Zirconia, *J. Am. Ceram. Soc.* **79**(5) (1996), p. 1169-1180.

[16] W. Puin, S. Rodewald, R. Ramlau, P. Heitjans and J. Maier, Local and overall ionic conductivity in nanocrystalline CaF_2, *Solid State Ionics* **131** (2000), p. 159-164.

[17] N. Sata, K. Eberman, K. Eberl, J. Maier, Mesoscopic fast ion conduction in nanometre-scale planar heterostructures, *Nature* **408** (2000), p. 946-949.

[18] A. Cheikh, A. Madani, A. Touati, H. Boussetta and C. Monty, Ionic conductivity of zirconia based ceramics from single crystals to nanostructured polycrystals, *J. Eur. Ceram. Soc*. **21**(10-11) (2001), p. 1837-1841.

[19] P.S. Manning, J.D. Sirman, R.A. De Souza, J.A. Kilner, The kinetics of oxygen transport in 9.5 mol % single crystal yttria stabilised zirconia , *Solid State Ionics* **100**(1-2) (1997), p. 1-10.

[20] M. Filal, C. Petot, M. Mokchah, C. Chateau and J.L. Carpentier, Ionic conductivity of yttrium-doped zirconia and the “composite effect”,*Solid State Ionics* **80**(1-2) (1995), p. 27-35.

[21] A. Madani, A. Cheikh-Amdouni, A. Touati, M. Labidi, H. Boussetta and C. Monty, Ionic conductivity of 4 mol%, 9.5 mol% YSZ nanomaterials and (9.5 mol% YSZ)$_{0.98}$–(Al_2O_3)$_{0.02}$ nanocomposites, *Sens. Actuators B* 109(1) (2005),

p. 107–111.

[22] D. Vladikova, J.A. Kilner, S.J. Skinner, G. Raikova and Z. Stoynov, Differential impedance analysis of single crystal and polycrystalline yttria stabilized zirconia, *Electrochimi. Acta* **51**(8-9) (2006), p. 1611–1621.

[23] J.H. Gong, Y. Li, Z.L. Tang, Y.S. Xie and Z.T. Zhang, Temperature-dependence of the lattice conductivity of mixed calcia/yttria-stabilized zirconia, *Mater. Chem. Phys.* **76**(2) (2002), p. 212–216.

[24] M. Kurumada, H. Hara, F. Munakata and E. Iguchi, Electric conductions in $La_{0.9}Sr_{0.1}GaO_{3-\delta}$ and $La_{0.9}Sr_{0.1}Ga_{0.9}Mg_{0.1}O_{3-\delta}$, *Solid State Ionics* **176**(3-4) (2005), p. 245-251.

[25] D.W. Strickler and W.G. Carlson, Electrical Conductivity in the ZrO_2-Rich Region of Several M_2O_3-ZrO_2 Systems, *J. Am. Ceram. Soc.* **48**(6) (1965), p. 286-289.

[26] V. Butler, C.R.A. Catlow, B.E.F. Fender, The defect structure of anion deficient ZrO_2, *Solid State Ionics* **5** (1984), p. 539-542.

[27] K. Okumura, Y. Aihara, S. Ito and S. Kawasaki, Development of thermal spraying-sintering technology for solid oxide fuel cells, *J. Therm. Spray Technol.*, **9**(3) (2000), p. 354-359.

[28]X.-J. Ning, C.-X. Li, C.-J. Li, and G.-J.Yang, Modification of microstructure and electrical conductivity of plasma-sprayed YSZ deposit through post-densification process, *Mater. Sci. Eng., A*, **428**(1-2) (2006), p. 98-105.

[29]K.A. Khor, X.J. Chen, S.H. Chan and L.G. Yu, Microstructure-property modifications in plasma sprayed 20 wt.% yttria stabilized zirconia electrolyte by spark plasma sintering (SPS) technique, *Mater. Sci. Eng., A*, **366**(1) (2004), p. 120-126.

[30] K.A. Khor, L.-G. Yu, S.H. Chan and X.J. Chen, Densification of plasma sprayed YSZ electrolytes by spark plasma sintering (SPS), *J. Eur. Ceram. Soc.*, **23** (11) (2003), p. 1855-1863.

[31]C. Zhao, J. Vleugels, G. Groffils, P.J. Luypaert and O. Van Der Biest, Hybrid sintering with a tubular susceptor in a cylindrical single-mode microwave furnace,

Acta Mater., **48**(14) (2000), p. 3795-3801.

[32] M. Mizuno, S. Obata, S. Takayama, S. Ito, N. Kato, T. Hirai and M. Sato, Sintering of alumina by 2.45 GHz microwave heating, *J. Eur. Ceram. Soc*., **24**(2) (2004), p. 387-391.

[33] W.H. Sutton, Microwave Processing of Ceramic Materials, *Am. Ceram, Soc. Bull.*, **68**(2) (1989), p. 376-386.

[34] G. Zhang, S. Leparoux, H. Liao, and C. Coddet, Microwave sintering of poly-ether-ether-ketone (PEEK) based coatings deposited on metallic substrate, *Scrip. Mater.*, **55**(7) (2006), p. 621-624.

[35] S.G. Huang, L. Li, O. Van der Biest and J. Vleugels, Microwave sintering of CeO_2 and Y_2O_3 co-stabilised ZrO_2 from stabiliser-coated nanopowders, *J. Eur. Ceram. Soc*., **27**(2-3) (2007), p. 689-693.

[36] J. Binner, K. Annapoorani, A. Paul, I. Santacruz and B. Vaidhyanathan, Dense nanostructured zirconia by two stage conventional/hybrid microwave sintering, *J. Eur. Ceram. Soc*., **5**(28) (2008), p. 973-977.

[37] D. D. Upadhyaya, A. Ghosh, K. R. Gurumurthy and R. Prasad, Microwave sintering of cubic zirconia, *Ceram. Inter.*, **27**(4) (2001), p. 415-418.

[38] X.Q. Liu and X.M. Chen, Microstructures and mechanical properties of 8Y-FSZ ceramics with $BaTiO_3$ additive, *Ceram. Inter.*, **30**(8) (2004), p. 2269-2275.

Chapter 4

Gas Tightness of Plasma-sprayed YSZ Coating and Gas Permeation Behavior through Coating

In this chapter, the gas tightness of APS YSZ coatings was evaluated via measuring coating gas permeability. The gas permeability of the APS coatings was estimated by oxygen, nitrogen or hydrogen. The effect of powder size, particle temperature and velocity on coating gas tightness was studied. Gas permeation behaviour through APS YSZ coatings was examined based on the gas permeation theory through porous materials. The bottle-neck to improve the tightness of APS coating was pointed out and a method to improve gas-tightness was proposed.

As aforementioned Chapter 1, SOFC electrolyte layer should be adequately dense and it is exerted to prevent H_2 or O_2 from permeating through electrolyte layer to meet each other. However, as well known, the plasma-sprayed coating exhibits unavoidable defects and does not show totally gas-tightness. The performance (or output power density) of the cell fabricated with APS electrolyte is decreased due to gas permeation. [1-4]. Therefore, to improve the gas tightness of electrolyte is an important challenge for APS YSZ electrolyte used in SOFC operation. In this chapter, the gas tightness of APS YSZ was evaluated by measuring the coating gas permeability.

4.1 Measurement of Gas Permeability

In this work, three YSZ powders of different size (a small size, medium size and large size powder) were used as feedstock for atmospheric plasma spraying under different spraying conditions to obtain coatings with diverse microstructures. In-flight particle velocity and surface temperature were measured by the DPV2000 system, which made it possible to examine the influence of particle characteristics on gas-tightness of APS YSZ coatings.

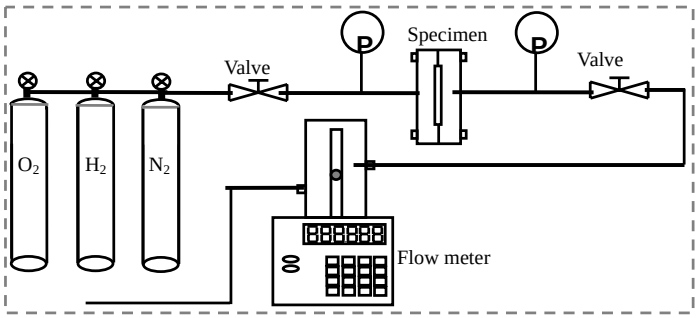

Figure 1: Scheme of the experimental set-up for gas permeability measurement.

The gas permeability was estimated using home-made equipment which was schematically shown in Figure 1. During the measurements, 900 μm thick free-standing

plasma-sprayed YSZ specimens with an effective surface of 1 cm^2 were set in a mould and then sealed with epoxy resin. Pure oxygen, nitrogen or hydrogen was supplied from gas cylinder at a constant pressure. The gas pressure was measured using two manometers. Once the steady pressure was reached, gas permeation volume rate through YSZ coating could be measured by an electromagnetic flow-meter (Drycall Ml-500, USA). The gas specific permeability was calculated based on the volume flow rate using Darcy's Law

$$k = K \cdot \nu = \frac{q \cdot \delta}{A \cdot \Delta p} \cdot \nu \qquad (1)$$

where q is the gas leakage flux; δ is the thickness of the layer; A is the area of the layer, Δp is the pressure difference, ν is the dynamic viscosity of the used gas, K is the gas permeability of the layer, k is the gas specific permeability. All units of the parameters were listed in the Glossary of this chapter.

4.2 Gas Tightness of Plasma-sprayed YSZ Coating

4.2.1 Influence of Powder Size on Coating Gas tightness

The polished cross-sections of APS YSZ coatings were observed by SEM with BEI mode as depicted in Figure 2. It can be clearly seen that the coatings deposited with the small size powders present a dense microstructure, while the coatings deposited by the large size powders show a high porosity level. Coating porosity was measured with the assistance of image analyzing technique. Porosity levels of 5.8, 10.5 and 22.5 % were estimated for the three coatings as shown in Table 1. In Figure 1(b), it can be observed that the size of pores in the coating existed in two scales [5]: global pores in the size-range 1-10 μm and small pores (cracks and non-bonded interface [6]) <0.1 μm. The latter type of pores is more predominant than global pores in YSZ dense coating.

Table 1: Porosity of three YSZ coatings.

Powders for coating	Small size powder	Medium size powder	Large size powder
Porosity	5.8%±0.6%	10.5±1.9%	22.5±3.1%

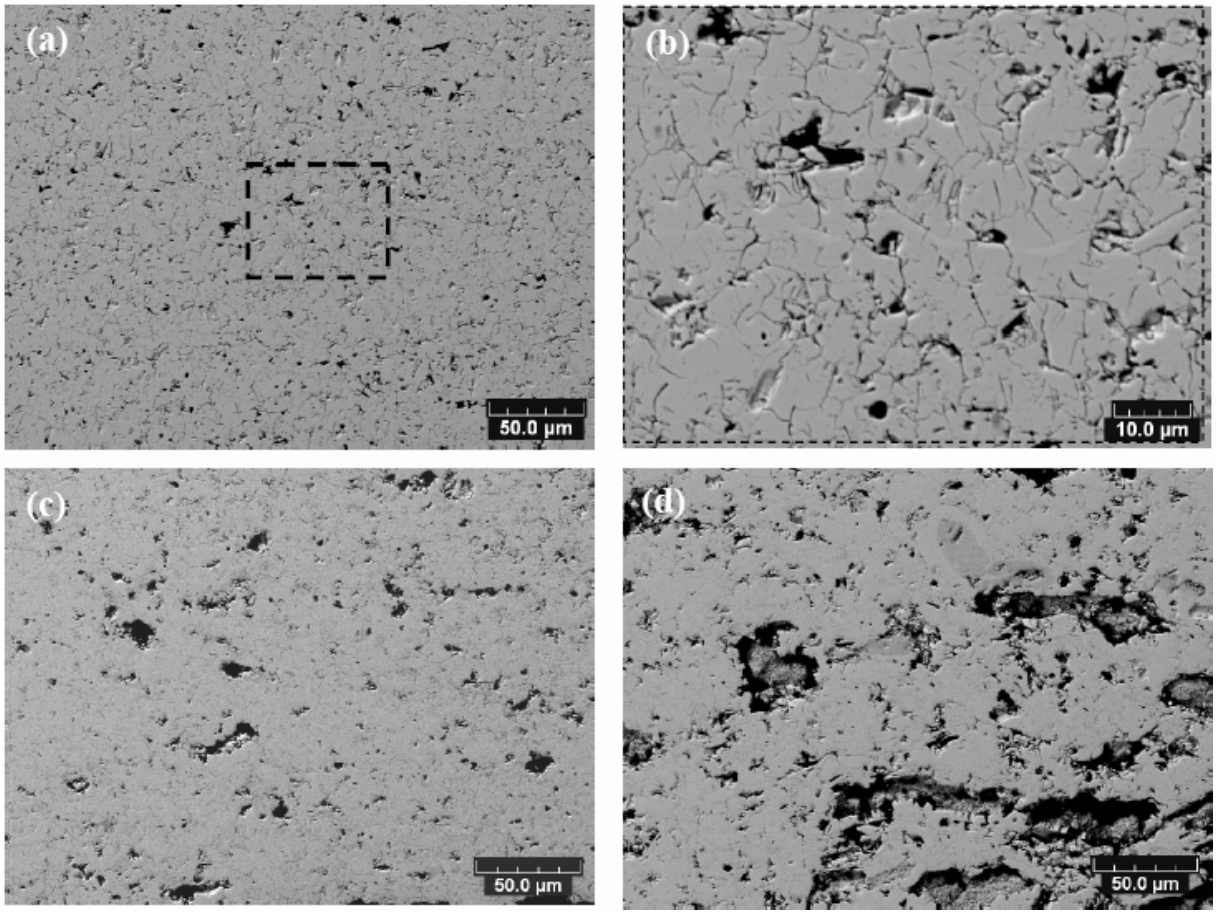

Figure 2: SEM polished cross-section microstructure of YSZ coatings. (a) the small size powder coating, (b) the small size powder coating in high magnification, (c) the medium size powder coating, (d) the large size powder coating.

Table 2: Gas specific permeability of three YSZ coatings.

Powders for coating	Small size	Medium size	Large size
Gas specific permeability	$4.80\times10^{-17}m^2$	$1.36\times10^{-16}m^2$	$1.93\times10^{-16}m^2$

Table 2 shows the gas specific permeability of the three coatings measured with H_2. The permeability of coatings ranged from $4.8\times10^{-17}m^2$ to $1.93\times10^{-16}\ m^2$. Fox et al. [2] reported the gas specific permeability from 6×10^{-17} to $1.8\times10^{-16}\ m^2$ for APS 4.9 mol% Y_2O_3-stabilized ZrO_2 coating. It seems that the results are reasonable compared with those reported by Fox et al. From the present results, the powder size has a significant influence on the gas permeability of plasma-sprayed YSZ coatings. The permeability of YSZ coatings deposited by the small size powder is less important than that sprayed by the medium size powder and is almost one fifth of that of the coating deposited by the large size powder.

4.2.2 Influence of Particle Temperature on Coating Gas Tightness

Table 3: Porosity of YSZ coatings deposited with different H_2 flow rate.

H_2 (l/min)	6	8	10	12
Porosity	5.8%±0.6%	6.6±0.5%	8.5±0.7%	10.3±1.0%

The effect of H_2 flow rate on particle temperature and coating microstructure was discussed in the section 2.3.1(3) and 2.3.2(3). The results showed that the particle temperature increased with the increase of H_2 flow rate. The porosity of the four YSZ coatings was listed in Table 3. The porosity of coatings decreases when the H_2 flow rate increases. As aforementioned, the pores in the plasma-sprayed coating exist in two levels: global pores (1-10 μm) and small pores (<0.1 μm, cracks and non-bonded interface). It should be noted that the main difference among the coating porosity is due to the variation of global pores, especially for the coating deposited with 8, 10 and 12l/min.

Table 4: Gas specific permeability of YSZ coatings deposited with different H_2 flow rate.

H_2 (l/min)	6	8	10	12
Gas specific permeability (m^2)	1.28×10^{-16}	5.71×10^{-17}	5.10×10^{-17}	4.80×10^{-17}

The gas specific permeability of the four coatings measured with H_2 was shown in

Table 4. The permeability of the coatings changed from $4.8\times10^{-17}m^2$ to 1.28×10^{-16} m^2 when H_2 flow rate changed from 12 to 6 l/min. The results showed that the H_2 flow rate had a positive effect on the gas tightness of plasma-sprayed YSZ coatings. This means that high temperature particles are favorable to produce gas-tight coatings. Further to examine the permeability of these coatings, it could be found that the difference among the coatings deposited with 8, 10 and 12 l/min was insignificant. Considering the data of coating porosity levels, although the coating porosity was an indication of coating gas-tightness, it could be pointed out that there is no direct relationship between the gas tightness and the porosity. The coating gas-tightness was related with the interconnect pores through the coating. In plasma-sprayed YSZ coating, the interconnected pores were composed of global pores, the vertical cracks and non-bonded interfaces in series. The dimension of global pores was much bigger than that of the vertical cracks and non-bonded interface. As a result, the dimension of the vertical crack and non-bonded interface determined the permeation flux through interconnect pores. In conclusion, the coating gas-tightness was determined by the dimension of non-bonded interface and vertical cracks.

4.2.3 Influence of Particle Velocity on Coating Gas Tightness

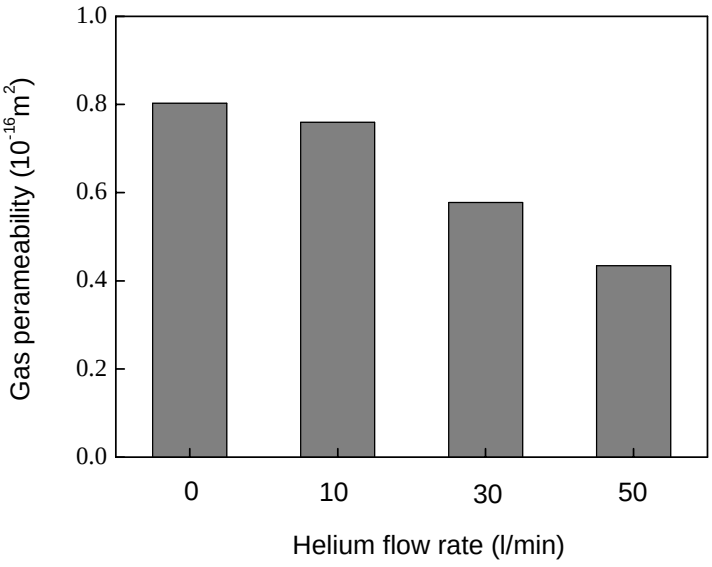

Figure 3: Effect of particle velocity (He flow rate) on the measured gas specific permeability of YSZ coatings.

Figure 3 shows the effect of particle velocity (directly related to He flow rate) on gas specific permeability of APS YSZ coatings measured with N_2 (Feedstock: the medium size powder; Current: 600A; Ar: 35l/min; H_2: 12l/min; He:0-50 l/min). It could be observed that the gas specific permeability almost decreases when He flow rate increases. The permeability of YSZ coatings obtained with the two extreme values of helium flow rate, 0 l/min and 50 l/min, are 0.81×10^{-16} and 0.43×10^{-16} m^2, respectively. This suggests that the gas specific permeability of APS YSZ coating could be decreased through the increasing in-flight particle velocity.

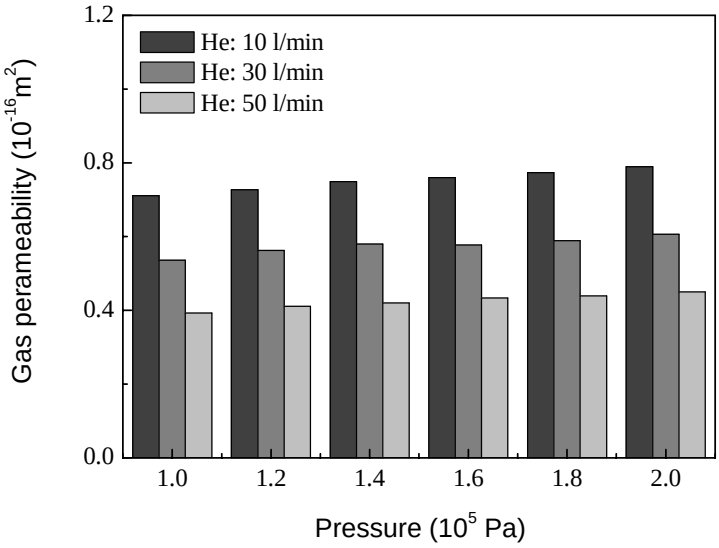

Figure 4: Effect of pressure difference on the measured specific permeability of plasma sprayed YSZ coatings with three different helium flow rates (10, 30 and 50 l/min).

According to equation (1), it can be pointed out that the gas specific permeability of coatings was independent on measuring gas pressure difference. However, it could be observed from Figure 4 that the gas specific permeability slightly increased when the gas pressure difference increased. As well known, the defects in terms of pores, non-bonded interface and vertical cracks are inherent to plasma-sprayed ceramic coatings [7]. Under high pressure difference condition, the free-standing coating could have a slight deformation, and the size of defects, especially vertical cracks, may be increased, which will result in an increase of gas specific permeability.

In chapter 3, the results showed that the particle velocity has little effect on the ionic conductivity of APS YSZ coatings. It was demonstrated that the ionic conductivity was determined by the lamellar microstructure and bonding ratio between lamella. The similar ionic conductivity of the coatings deposited with different particle velocity indicated that the particle velocity had little influence on the bonding condition of plasma-sprayed coatings. On the other hand, considering gas permeability improvement, it seemed that raising the particle velocity influences the morphologies of gas pathway. In the study of Fantassi et al. [9], they investigated the effect of YSZ particle velocity on spreading and cooling processes on a smooth steel substrate. They concluded that increasing particle velocity will decrease the flattening time and increase the flattening degree of splat. In plasma-sprayed ceramic coating, the pathway for leakage gas was composed of the pores, non-bonded interface and vertical cracks. When YSZ coatings are deposited with high particle velocity, the coating was built up with splats of high flattening degree. This means that the coating was constituted with more splats in the direction perpendicular to coating surface and as a result, it increases the length of gas leakage pathway. On the other hand, when the spray particles impact at high velocity, the high particle kinetic energy will decrease the cross-sectional area of leakage pathway via reducing the opening of non-bonded interface. This could be the reason that the increase in particle velocity leads to diminish the coating gas permeability.

4.3 Gas Permeation Theory

When isothermal conditions are assumed, gas permeation can occur by means of viscous flow, Knudsen flow and/or surface diffusion in the porous medium [10,11]. A transport of adsorbed molecules or atoms on solid surfaces, called surface diffusion, could be neglected in this study. The Knudsen number [12], the ratio of the mean free path of the gas to the pore diameter ($Kn = \lambda / d$, the symbols used are listed in the Appendix) determines the gas permeation behaviour through a porous medium. When the mean free

path of gas is small compared to the pore diameter (Kn<<1), gas molecule-molecule collisions predominate over molecule-wall, it is called viscous flow region. Whereas, if the mean free path of gas is large relative to the pore diameter (Kn>1), gas molecule-wall collisions will become significant, which was named Knudsen flow region.

4.3.1 Viscous Flow

In viscous region, single gas permeation through porous medium occurs only by a pressure gradient $\frac{\Delta P}{\Delta z}$. Gas specific permeability through the porous medium can be described by Darcy's law.

$$k_{vis} = \frac{q \cdot \Delta z}{A \cdot \Delta p} \cdot \mu \quad (2)$$

The gas mole flow rate can be calculated due to the pressure gradient,

$$J_{vis} = \frac{k}{\mu} \cdot \frac{P}{RT} \cdot \frac{\Delta P}{\Delta z} \quad (3)$$

For a given porous medium, gas specific permeability only depends on the pore structure. Under consideration of an ideal gas, the integration gives,

$$J_{vis} = \frac{k}{\mu} \cdot \frac{\overline{P}}{RT} \cdot \frac{\Delta P}{\Delta z} \quad (4) \quad \text{with} \quad \overline{P} = \frac{P_{in} + P_{out}}{2} \quad (5)$$

In the viscous region, gas mole flow rate through porous medium can be assumed as a laminar flow. Under this condition, Darcy's law has the same form as the Poiseuille's law. For simplicity, Poiseuille's law for laminar flow in a cylindrical tube has been adopted in this study. The following expression of gas flow rate through the porous medium can be found by applying Poiseuille's law.

$$J_{vis} = \frac{\varepsilon r^2}{8 \mu RT \tau \Delta z} \cdot \overline{P} \cdot \Delta P \quad (6)$$

where r describes a mean pore diameter and ε is the porosity, which takes into account the volume of pores that goes from one face of the porous medium through the other. The tortuosity factor τ takes into account the additional drag by the irregular shape and the actual length of the pores in the comparison with a bundle of straight parallel capillaries with constant diameter. From the Poiseuille's law and Darcy's law, the following relation of the permeability to the pore diameter can be found:

$$k_{vis} = \frac{\varepsilon r^2}{8\tau} \quad (7)$$

4.3.2 Knudsen Flow

In Knudsen region (k>1), the single gas permeation through porous medium occurs due to free molecule flow [12]:

$$J_{kn} = \frac{4\sqrt{2}}{3} \frac{\varepsilon r}{\Delta z \tau \sqrt{RT\pi M}} \cdot \Delta P \quad (8)$$

where ε describes the porosity and τ factor is tortuosity factor. It is possible to introduce a Knudsen coefficient D_{kn}:

$$J_{kn} = \frac{D_{kn}}{RT} \frac{\Delta P}{\Delta z} \quad (9)$$

With $D_{kn} = \frac{4\sqrt{2}}{3} \cdot \frac{\varepsilon r}{\tau} \cdot \sqrt{\frac{RT}{\pi M}}$ (10)

4.3.3 Transition Region

In the transition region (0.01 <Kn <1), gas permeation through the porous medium can be described as the sum of the fluxes due to viscous flow and due to Knudsen flow. With the equation (5), (7) and (10),

$$J_{tot} = J_{vis} + J_{kn} = \left(\frac{k}{\mu} \overline{P} + D_{kn} \right) \frac{1}{RT} \frac{\Delta P}{\Delta z} \qquad (11)$$

From analysis and evaluation of the measurement, a total permeability K_{tot} could be introduced,

$$J_{tot} = \frac{k_{tot}}{\mu} \cdot \frac{\overline{P}}{RT} \cdot \frac{\Delta P}{\Delta z} \qquad (12)$$

Where $k_{tot} = k + \frac{D_{kn} \cdot \mu}{\overline{P}} = \frac{\varepsilon r^2}{8\tau} + \frac{4\sqrt{2}}{3} \frac{\varepsilon r}{\tau} \sqrt{\frac{RT}{\pi M}} \frac{\mu}{\overline{P}}$ (13)

When using different types of gas to measure the permeability under a constant average pressure, the equation (13) can be written as:

$$k_{tot} = a + bx \quad (14)$$

Where $a = \frac{\varepsilon r^2}{8\tau}$ (15)

$$b = \frac{4\sqrt{2}}{3} \frac{\varepsilon r}{\tau \overline{P}} \sqrt{\frac{RT}{\pi}} \quad (16)$$

$$x = \frac{\mu}{\sqrt{M}} \quad (17)$$

4.4 Gas Permeation through Plasma-sprayed Coating

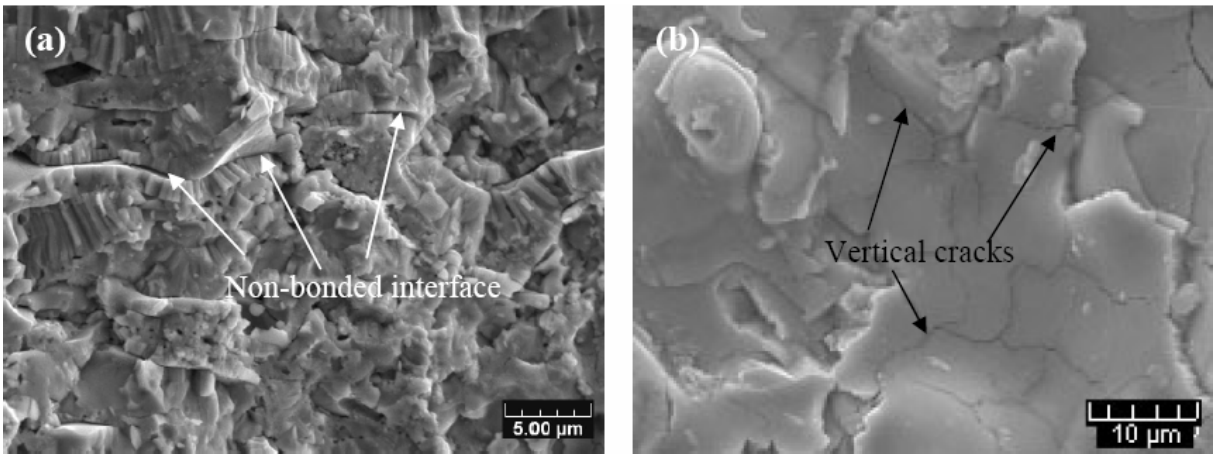

Figure 5: Non-bonded interfaces and vertical cracks in the plasma-sprayed YSZ coatings.

Plasma-sprayed coating is formed by a stream of molten or partially molten droplets impacting on a substrate. The individual molten droplets spread to thin lamellae, which constitute the deposit. As a result, a plasma-sprayed deposit is generally of lamellar structure. Pores are always present in the obtained coatings, especially for ceramic coatings. As aforementioned, these pores could be divided into two types according to size: large pores (1-10 µm) and small pores (<0.1 µm). With regard to the small pores, they could be also classified as two types: non-bonded interface and vertical cracks as shown in Figure 5. A more detailed study on the size distribution of non-bonded interface in plasma-sprayed YSZ coating was investigated by analyzing the distribution of an alumina tracer filling the voids of the coating [13]. The results showed that the width of non-bonded interfaces was less than 0.5µm or less than 1 µm under different spraying distances [13]. The width of vertical cracks was about 0.1 µm [14,15]. The size distribution and Knudsen number for different types of pores are summarized in Table 5. The average free path of H2, N2 and O2 is 0.113, 0.0559 and 0.0647 µm (25°C, 1 atm). Then, the Knudsen number could be calculated with the equation $Kn = \lambda / d$. For three types of pores, the Knudsen number has different values. This result indicates that gas

permeation through plasma-sprayed coating could be in the domain of transition region (connection in series with two regions).

Table 5: Size distribution and Knudsen number for three types of pores.

	Size distribution	K_n (H_2 at 25°C=0.113 μm)
Global pore	1-10 μm	>10
Non-bonded interface	<0.1 μm	<1
Vertical crack	about 0.1 μm	about 1

Table 6: Mean free path and $\frac{\mu}{\sqrt{M}}$ values for O_2, N_2, and H_2.

	H_2	O_2	N_2
μ [Pa s]	0.88×10^{-5}	1.92×10^{-5}	1.66×10^{-5}
M [g/mol]	2	32	28
$\frac{\mu}{\sqrt{M}}$ [mol/(g s Pa)]	0.622×10^{-5}	0.3392×10^{-5}	0.3137×10^{-5}

Figure 6 shows the gas specific permeability of the three coatings using different gases. The results showed that the gas permeability of a coating deposited with small powders was less than that of the coating deposited by large powders. This tendency was consistent with the coating porosity values obtained by image analysis (IA) technique. It seems that the porosity level in the coating appears to be an indicator of gas permeability of coating.

The gas specific permeability for three coatings was measured using nitrogen, oxygen and hydrogen as testing gas. The permeability data was fitted using lines according to equation (12) and the fitting equations were shown in Figure 6. The dynamic viscosity, molecular weight and x ($\frac{\mu}{\sqrt{M}}$) values for the three gases were summarized in Table 6. For all three coatings, the values of gas permeability obtained by hydrogen were much larger

than those estimated by oxygen and nitrogen. According to equation (12), if the gas permeation through plasma-sprayed YSZ coating was viscous flow, the value of the gas specific permeability was only dependant on coating microstructure. There will be no difference in the permeability using different measuring gases. This difference confirms that Knudsen flow exists for gas permeation through these three YSZ coatings. Furthermore, it could be found that Y intercepts of fitting lines were not zero, and the values were 0.888, 0.329 and 0.077 respectively. This fact showed that viscous flow was also present in the gas permeation for these coatings. One could conclude that the transition flow behaviour could be applied for gas permeation through plasma-sprayed YSZ coatings.

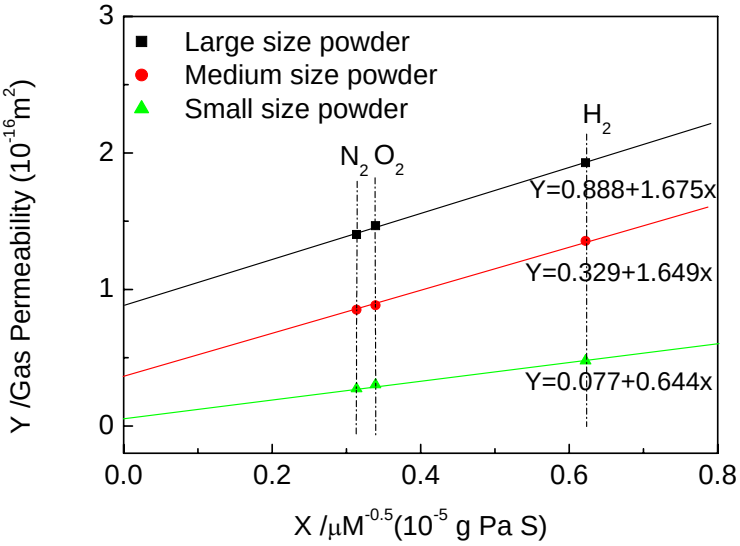

Figure 6: Gas permeability of different coatings measured by N_2, O_2 and H_2. (25°C).

By observing the data shown in Figure 6, it could be found that the Y intercepts of fitting line of coating deposited with the small size powders were less than that of coating deposited with large size powder. This phenomenon shows that the effect of viscous flow will become insignificant when the size of powder decreases. It could be deduced that the gas permeation through viscous flow may disappear in coating when further decreasing the size distribution of powders. The coating gas permeation behaviour will transfer to

Knudsen flow with smaller powders. However, in plasma spraying, it will become difficult to feed the powders when the particle is less than 5 μm. On the other hand, it could be also found that the slope of the fitting line for the coating deposited by small powders was smaller compared to that by large powders. From equation (14), it could be found that the slope of the fitting line was determined by porosity ε and pore diameter r. Both the porosity and pore size of coatings deposited with small powders were smaller than those deposited with large powder. Then, it is reasonable to find that the slope of the fitting line for dense coatings was smaller than that of porous coating.

4.5 Conclusions

In this chapter, the gas specific permeability of APS YSZ coatings was measured. The effect of particle temperature (H_2 flow rate), velocity (He flow rate) and particle size on the gas specific permeability of APS YSZ coatings was studied. The gas permeation behavior through APS YSZ coatings were investigated for the coatings with diverse microstructures. Then the following conclusions could be drawn:

(1) The results showed that the small size powder was favourable to deposited YSZ coatings with low gas permeability. The gas specific permeability was respectively $4.80\times10^{-17}\,m^2$, $1.36\times10^{-16}\,m^2$ and $1.93\times10^{-16}m^2$ for the coatings deposited with the small, the medium and the large powder.

(2) When H_2 flow rate decreased, the particle temperature was also decreased. The coating deposited with low H_2 flow rate shows high porosity level, especially the global pores. Although the coating porosity was an indication of coating gas permeability, it was found that there is no direct relationship between the gas permeability and porosity. The dimension of vertical cracks and non-bonded interface determines the coating gas permeability.

(3) The particle velocity has a positive effect on coating permeability. Adding helium

in the plasma gas increases the particle velocity and improves the coating gas-tightness. When helium changed from 0 to 50 l/min, the gas permeability of YSZ coatings was reduced from 0.81×10^{-16} to 0.43×10^{-16} m^2, correspondingly.

(4) The same gas permeation behaviour, - transition behaviour, was exhibited for all the three YSZ coatings. However, the proportion of viscous flow and Knudsen flow was different depending on coating microstructure. The results showed that the effect of viscous flow will become low and the effect of Knudsen flow will be significant for plasma-sprayed YSZ coating when the size of sprayed powder decreases.

4.6 References

[1] C.-J. Li, C.-X. Li and X.-J. Ning, Performance of YSZ electrolyte layer deposited by atmospheric plasma spraying for cermet-supported tubular SOFC, *Vacuum* **73**(3-4) (2004), p. 699-703.

[2] A. C. Fox and T. W. Clyne, Oxygen transport by gas permeation through the zirconia layer in plasma sprayed thermal barrier coatings, *Surf. Coat. Technol.* **184**(2-3) (2004), p. 311-321.

[3] J. Ilavsky, C.C. Berndt and J. Karthikeyan, Mercury intrusion porosimetry of plasma-sprayed ceramic, *J. Mater. Sci.* **32**(15) (1997), p.3925-32.

[4] M. Fukumoto, T. Ueda and I. Okane, Gas permeability of plasma sprayed MoSi[2] coating, *J. Mater. Sci. Let.* **13**(9) (1994), p. 656-657.

[5] K.A. Khor, L.-G. Yu, S.H. Chan and X.J. Chen, Densification of plasma sprayed YSZ electrolytes by spark plasma sintering (SPS), *J. Eur. Ceram. Soc.* **23**(11) (2003), p. 1855-1863.

[6] C.-J. Li and A. Ohmori, Relationships between the microstructure and properties of thermally sprayed deposits, *J. Therm. Spray Technol.* **11**(3) (2002), p. 365-374.

[7] R. Vaßen, D. Hathiramani, J. Mertens, V.A.C. Haanappel and I.C. Vinke, Manufacturing of high performance solid oxide fuel cells (SOFCs) with atmospheric plasma spraying (APS), *Surf. Coat. Technol.* **202**(3) (2007), p. 499-508.

[8] R. McPherson, A review of microstructure and properties of plasma sprayed ceramic coatings. *Surf. Coat. Technol.* **39-40** (1989), p. 173-181.

[9] S. Fantassi, M. Vardelle, A. Vardelle, P. Fauchais, Influence of the velocity of plasma-sprayed particles on splat formation, *J. Therm. Spray Technol.* **2**(4) (1993), p. 379-384.

[10] E.A. Mason and A.P. Malinauskas, *Gas Transport in Porous Media: The Dusty Gas Model*, Elsevier, Amsterdam, 1983.

[11] J.O. Hirschfelder, C.F. Curtiss, R.B. Bird, *Molecular theory of gases and liquids*, Wiley, New York, 1954.

[12] R.B. Bird, W.E. Stewart, E. N. Lightfoot, *Transport Phenomena*, Wiley, New York, p. 1976.

[13] C.-J. Li and W.-Z. Wang, Quantitative characterization of lamellar microstructure of plasma-sprayed ceramic coatings through visualization of void distribution, *Mater. Sci. Eng. A* **386**(1-2) (2004), p. 10-19.

[14] A.C. Fox and T.W. Clyne, Oxygen transport through the zirconia top coat in thermal barrier coating systems, *Meeting the Challenges of the 21st Century*, C.Coddet (Ed.), ASM International, Nice, France (1998), p.1589-1594.

[15] W.-Z. Wang, Ph.D. Dissertation, Quantitative characterization of lamellar microstructure of plasma sprayed coatings and relationship between lamellar microstructure and properties of coatings, Xi'an Jiaotong University, 2004 (in Chinese).

Appendix-Glossary

Symbols

K_n:	*Knudsen number*
λ:	*mean free path [m]*
ΔP:	*pressure difference [Pa]*
Δz:	*thickness [m]*
k:	*gas specific permeability [m^2]*
μ:	*dynamic viscosity [Pa s]*
q:	*volume flux [m^3/s]*
A:	*surface area [m^2]*
R:	*gas constant [R=8.314510J/(mol K)]*
T:	*temperature [K]*
J:	*Molar flow rate [mol/(m^2 s)]*
ε:	*Porosity*
Δz:	*pore diameter [m]*
τ:	*tortuosity factor*
M:	*molecular weight [g/mol]*

Subscripts

Kn:	*knudsen flow*
Vis:	*viscous flow*
Tot:	*Total*

Chapter 5

Integrated Thermal Spraying Process and Electrical Performance of Tubular Solid Oxide Fuel Cells

In this chapter, tubular Ni-YSZ/YSZ/LSM ($La_{0.8}Sr_{0.2}MnO_3$) solid oxide fuel cells were prepared by the integrated thermal spray process. The fabrication process and microstructure of the cell components were depicted. The as-sprayed cells were post-treated with a densification process to improve the gas-tightness of electrolyte and to enhance the performance of the cell. The output circuit voltage and power density of the cells were measured.

5.1 Cell Structure Design

5.1.1 Introduction

SOFC structure design must face the potential restrictions of the employed materials and the desired properties for each component. Cell structure design must also take into account the physical, chemical, electrical, electrochemical and mechanical requirements of the stack at the operating temperatures. Another consideration in cell design is how to control the porosity of different components in order to ensure proper gas transport to the electrodes and gas-tightness of electrolyte. There are three basic SOFC structure designs as aforementioned in the Chapter 1: segmented-cell-in-series, tubular and planar structures [1].

High-temperature solid oxide fuel cells (SOFCs) receive considerable interest nowadays, because they promise greater conversion efficiency than those obtained by a conventional heat engine or other types of low temperature fuel cells. Furthermore, because of their high operation temperature (800-1000°C), some hydrocarbon fuels such as natural gas can be reformed within the cell eliminating the need for an expensive, external reformer.

For high-temperature SOFCs, the most used structure design is tubular design. The tubular design was proposed in the 1980s and is sometimes referred to as "Westinghouse design", as the research done at Westinghouse Ltd. which turned this design from a proposal to a working stack [2]. The most interesting advantage of the tubular design is its seal-less. The tubes are bundled in pairs and electrical connections are made in series to each parallel bundle. The extrusion and colloidal spray techniques have been used for the majority of the components. The electrolyte and interconnector are sometimes made using EVD, which increases the cell costs [2]. The disadvantages of this design are a long current path leading to low power density.

In this thesis, a tubular cell made up of integrated plasma-sprayed electrolyte and two electrode layers on a flame-sprayed cermet support tube with one close-end design was elaborated. The strength of cermet (Ni/Al_2O_3)-supported tube is better than the conventional ceramic supported tube. The sufficient Ni content in the cermet-substrate provides a high electrical conductivity of a substrate and plays the role as a current

collector. As a result, it would avoid the problem of long current path in the classic tubular cell. The electrical output performance was tested in the thermal spray laboratory of Xi'an Jiaotong University.

5.1.2 Cell Structure

Figure 1 shows the scheme of cell structure prepared by the integrated thermal spray process. Table 1 lists the materials and processes used for different components. The detail of process parameters will be presented in the next Section.

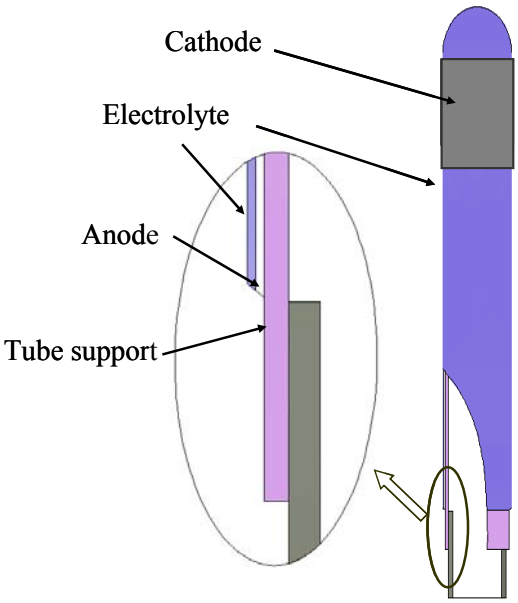

Figure 1: Scheme of cell structure prepared by the integrated thermal spray process.

Table 1: Materials and processes used for the components of the cell.

	Materials	Processes
Tube support	Ni/Al_2O_3+NiO/Al_2O_3	Flame spraying process
Anode	Ni-YSZ	APS process
Electrolyte	YSZ	APS and LPPS process
Cathode	LSM	APS process

5.2 Cell Fabrication Process

5.2.1 Cermet-Supported Tube

Table2: Powders used in the step of fabricating supported tube

	Particle size distribution
NiO	8-10 μm
Al_2O_3	5~45 μm
Ni/Al_2O_3	60~120 μm

The porous cermet substrate supported tube was prepared with Ni/Al_2O_3 by flame spraying technique using Ni coated Al_2O_3, NiO and Al_2O_3 as feedstock materials. The morphology of NiO and Ni coated Al_2O_3 powders were shown in Figure 2. The size distributions of the powders were shown in Table 2. NiO, Al_2O_3 and Ni/Al_2O_3 powders were mechanically mixed for 20 minutes and used as feedstock for flame spraying. Casto Dyn® 8000 flame spraying gun mounted on an ABB Robot (ABB, Sweden) was used to deposit coating on the stainless steel tube. The powders were fed by a Twin-System 10 Distributor (Plasma-Technik AG, Switzerland). The tube was fixed on a rotary worktable at a given rotational speed. Prior to spraying cermet powder, the stainless steel tube was deposited with a flame-sprayed NaCl coating, which would be dissolved in the water and used to remove the cermet tube from the stainless tube.

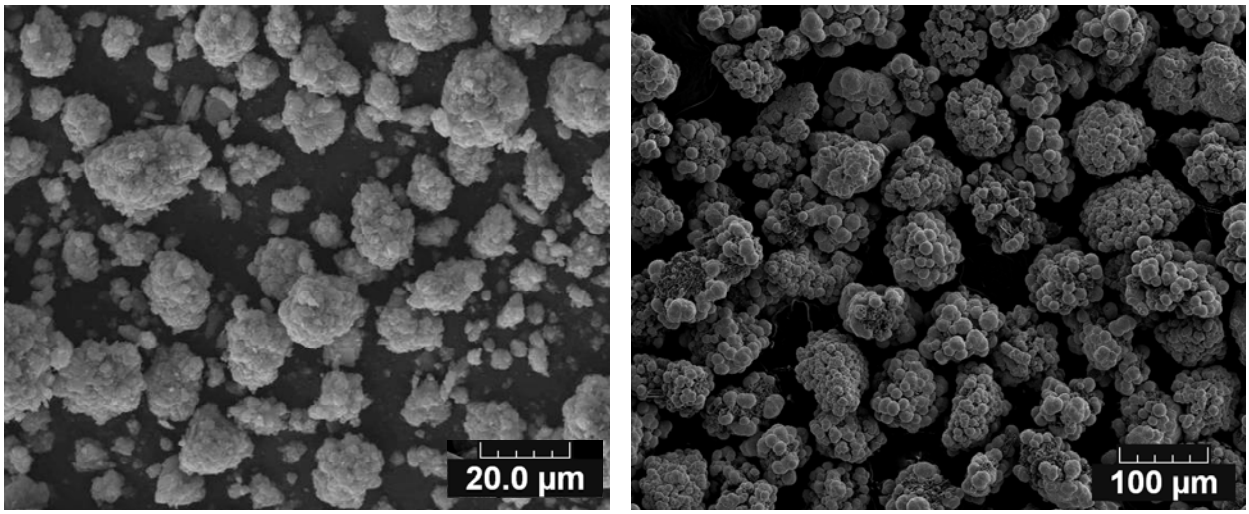

Figure 2: SEM morphology of NiO and Ni/Al_2O_3

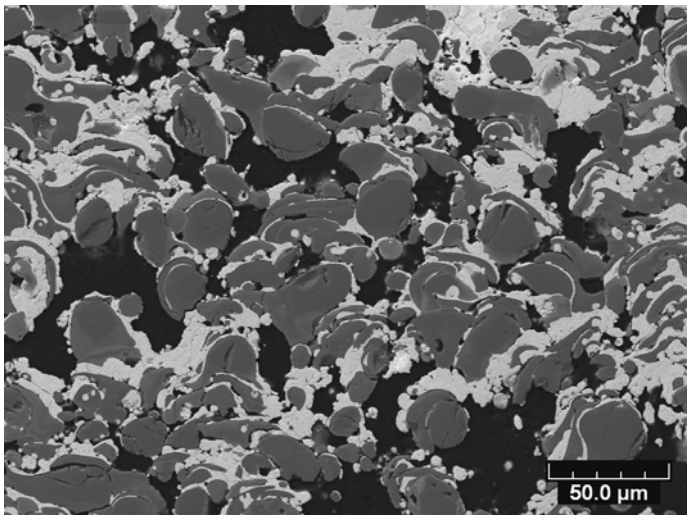

Figure 3: Polished cross-sectional surface of flame-sprayed cermet-supported coating

Figure 3 shows the polished cross-sectional surface of flame-sprayed cermet coating. The region in a deep grey contrast in the coating was Al_2O_3 and nickel oxide, and the region with a bright contrast was nickel. The results showed that the obtained coating had a porosity of about 30%. When the coating is reduced in the H_2 atmosphere at high temperature, nickel oxide will be reduced to nickel and an additional amount of porosity will be produced. That is to say, the porosity of the coating after H_2 reduction was more than 30%, which would be necessary for H_2 to pass through to anode in the practice operation.

5.2.2 Anode

Ni/YSZ was adopted as anode materials. In order to ensure that there would be adequate Ni to form the consecutive electrical conductor, the weight ratio of NiO to YSZ was set to 127: 100 in this study. The small size YSZ and NiO powders were mechanically blended for 20 minutes. After this step, the powders were mixed with 5% PVA to form large particles (60-100 µm) to get a homogeneous composition. At last, the powder was meshed to control size distribution and dried in the furnace at 200°C for 2 hours. However, the SEM morphology of obtained powders as shown in Figure 4 shows that the YSZ powder was too large to agglomerate with NiO, and there is only some

agglomeration formed with NiO powders.

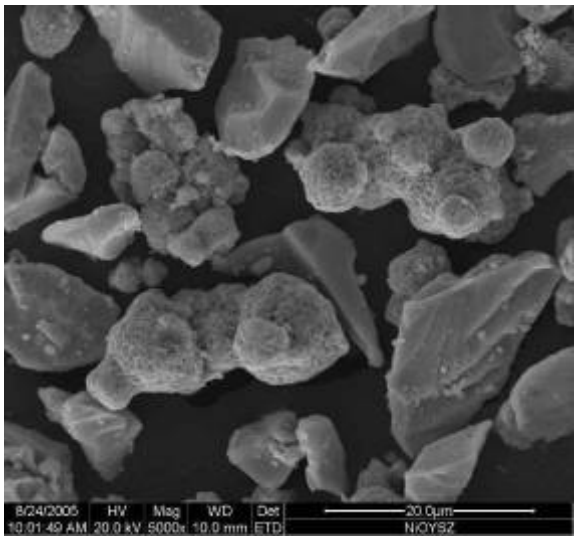

Figure 4: SEM of NiO/YSZ powder

APS with F4MB torch was used to deposit NiO/YSZ coating. During spraying, compressed air was applied around the torch to cool the tube. The other spraying parameters are listed in Table 3.

Table 3: The spray parameters to prepare the anode coating.

Current [A]		580
Gas flow [l/min]	Primary gas [Ar]	35
	Secondary gas [H_2]	6
Spray distance[cm]		11
Gun traverse speed [mm/s]		50

Figure 5(a) shows the polished cross-sectional microstructures of the as-sprayed anode coating. Being alike to the classical plasma-sprayed coating, the anode coating has a lamellar microstructure too. Figure 5(b) and (c) give the distributions of the elements Ni and Zr determined by the EDS chemical mapping analysis of the corresponding polished surface. The results showed that the NiO and YSZ homogeneously existed in the as-sprayed anode coating. Although the porosity was less than 30% in the as-sprayed anode coating, the value will increase when the NiO was reduced to Ni in the high temperature H_2 atmosphere.

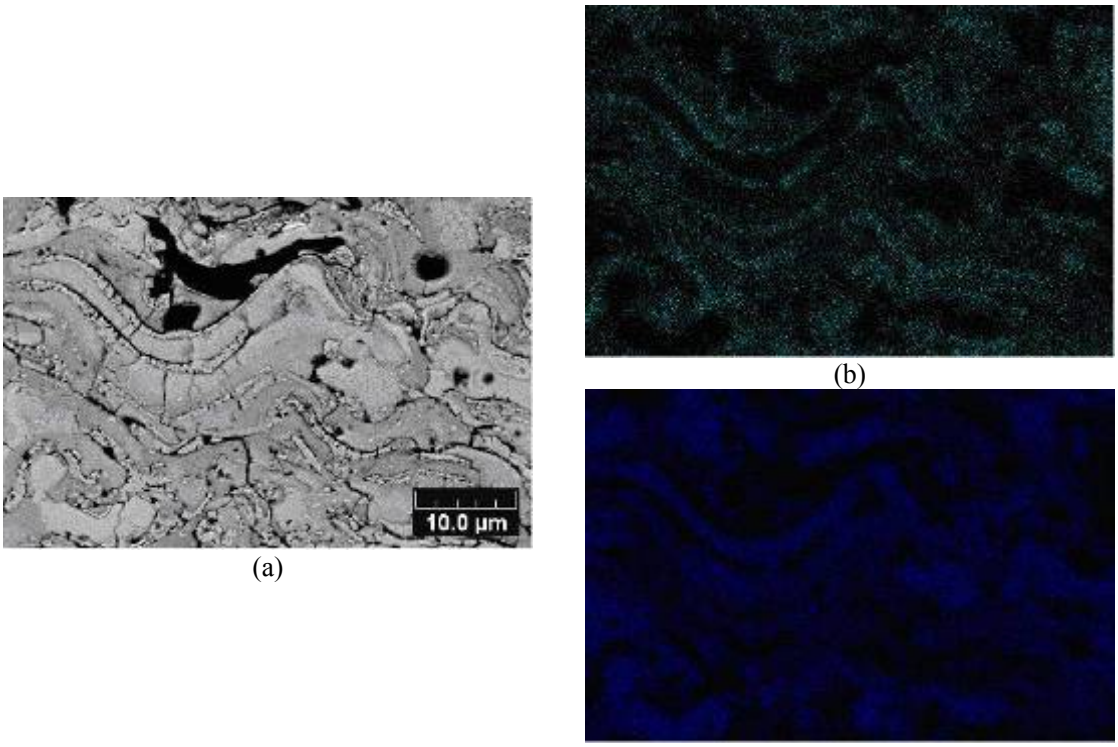

(a)

(b)

(c)

Figure 5: (a) SEM polished cross-section microstructure of the anode coating and EDS chemical mapping analysis of Ni(b) and Zr(c) elements in the corresponding surface.

5.2.3 Electrolyte

In chapter 3 and 4, the results showed that the small size powder was the best choice for YSZ electrolyte deposition. APS was employed to prepare YSZ electrolyte layer with the medium size and the small size powders. APS was carried out in an ambient atmosphere and YSZ coating was deposited on the pre-deposited anode coating. APS parameters were listed in Table 4.

Table 4: Spraying parameters used for APS YSZ layer

Current [A]	600
Primary gas [Ar, l/min]	35
Secondary gas [H_2, l/min]	12
Carrier gas [Ar, l/min]	3.5
Spraying distance [mm/s]	100
Gun traverse speed [mm/s]	400

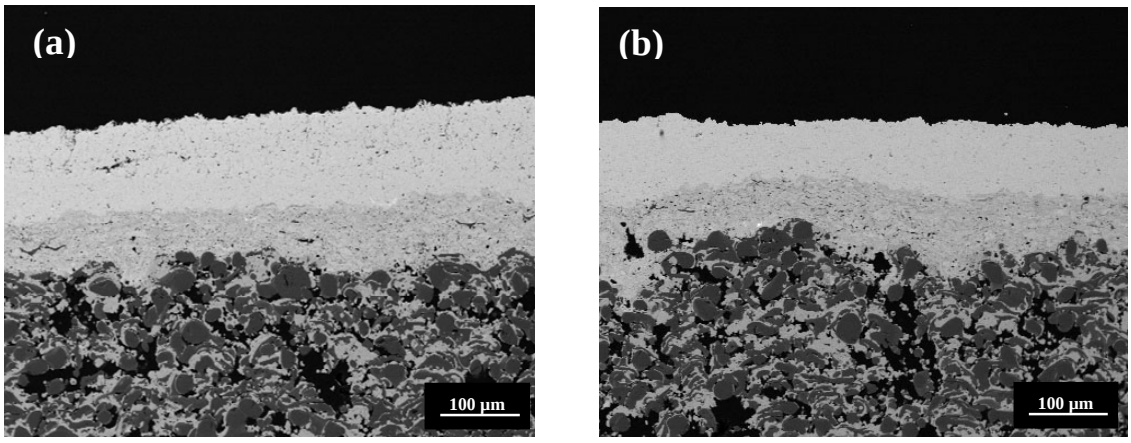

Figure 6: Microstructure of cermet-supported cells with (a): 100 µm YSZ electrolyte deposited with the medium size powder, (b) 80 µm YSZ electrolyte deposited with the small size powder.

In this thesis, 100 and 80 µm thick YSZ coatings were prepared by APS with the medium size and the small size powder on the pre-deposited tubes which were already deposited by the supported cermet and anode coating. In this study, the supported cermet and the anode coatings were prepared with the optimized parameters.

LPPS (low pressure plasma spraying) with F4VB plasma torch (Sulzer Metco AG, Switzerland) was also used to prepare YSZ layer. LPPS was carried out in an argon atmosphere under a pressure of 200 mbar (0.02 MPa). Spray conditions are listed in Table 5. The preheating of the tube to 700°C was also performed using plasma arc just before deposition. The small size powder was also used to deposit an 80 µm thick LPPS YSZ layer on the pre-deposited anode layer.

Table 5: Spraying parameters used for LPPS YSZ layer

Current [A]	700
Plasma power [kW]	45
Chamber pressure [MPa]	0.02
Standoff distance [mm]	260
Argon [$l \cdot min^{-1}$]	45
Hydrogen [$l \cdot min^{-1}$]	14
Argon powder carrier gas [$l \cdot min^{-1}$]	3.7

5.2.4 Densification of Electrolyte

Although many works have been carried out to improve the gas-tightness of plasma-sprayed YSZ coating, the results showed that the as-sprayed cell could not be used in a real operation due to the low gas-tightness of the electrolyte layer. As a result, a post-spray densification process should be done on as-sprayed fuel cell to improve its gas-tightness. In this study, a chemical solution densification was employed [3,4,5]. This process was developed for plasma-sprayed YSZ electrolytes by repeated infiltration of the zirconium and yttrium nitrate solutions followed by a baking process at 400°C for complete decomposition of the nitrates. This process is an effective and patented process which was developed by Xi'an Jiaotong University. The detail and mechanism of this process could be found elsewhere [3,4].

Table 6: Output circuit voltage of the cell before and after the densification.

	600°C	700°C	800°C
As-sprayed (V)	0.84	0.82	0.79
After Densification (V)	1.09	1.07	1.05

In this study, the as-sprayed cells were infiltrated by the chemical solution for 20 times. Table 6 shows the OCV (output circuit voltage) of the cell deposited with 80 μm APS YSZ electrolyte before and after the post-spray densification process at a temperature from 600 to 800°C. It could be found that the OCV was significantly improved by the post-spray densification process. The OCV of the as-sprayed cell was only 0.79V at 800^{o}C. After 20 times infiltration, the OCV reaches 1.05 V at the same temperature.

5.2.5 Cathode

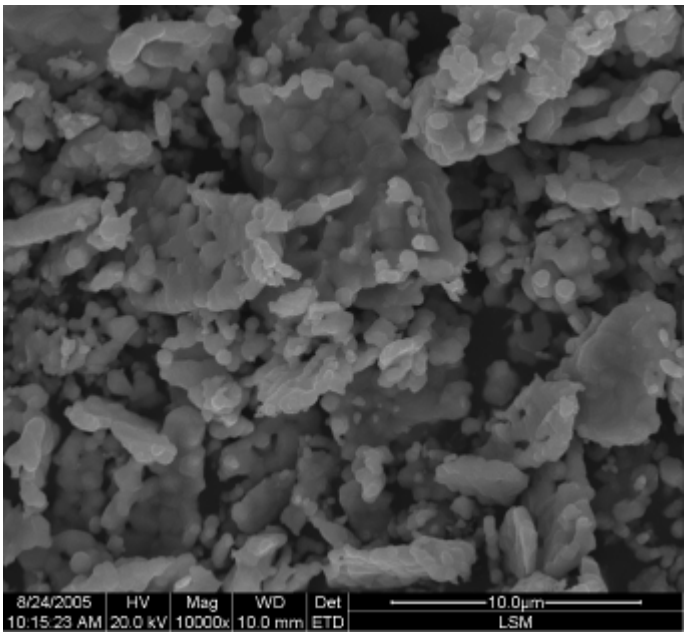

Figure 7: Morphology of the LSM cathode powder.

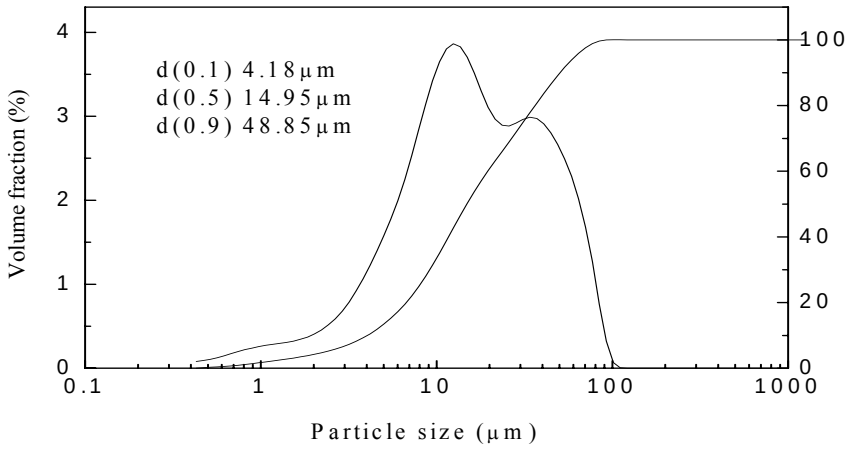

Figure 8: Size distribution of the LSM cathode powder.

To enable the cathode reaction $O_2+4e^-\rightarrow 2O^{2-}$, oxygen gas, electrons and a medium to transport the oxygen ions are necessary. For high temperature SOFCs, LSM ($La_{0.8}Sr_{0.2}MnO_3$) is often used as cathode material. Commercially $La_{0.8}Sr_{0.2}MnO_3$ (Inframat Advanced Materials, USA) powders were used as feedstock materials in this study. The morphology of LSM powders is shown in Figure 7. The powder size distribution was measured with a laser particle size analyzer (Mastersizer 2000, Malvern Instruments, UK) as shown in Figure 8. LSM coatings were sprayed by commercial

plasma spraying system (GDP-80, 80 kW class, Jiujiang, China) in Xi'an Jiatong University. Argon and hydrogen were operated at 0.8 and 0.4 MPa, respectively. The flow rate of argon was fixed to 47 l/min. The other spraying parameters were listed in Table 7. In order to ensure gas transport through the cathode layer, a thin 15 µm thick LSM coating was deposited on the electrolyte layer. In order to better observe the microstructure and the phase structure of the LSM coating, a 500 µm thick LSM coating was deposited on aluminum substrate with the same spraying parameters as the cathode layer. The phase constitutions of both the starting powders and deposited coating were characterized by X-ray diffraction analysis (D/max2400, RIGAKU, Japan) using CuK$_\alpha$ radiation. A 2θ scanning rate of 10°C min^{-1} was used during test.

Table 7: Spraying parameters used for deposition of YSZ coating.

	Value
Current [A]	600
Voltage [V]	50
Gun traverse speed [mm/s]	50

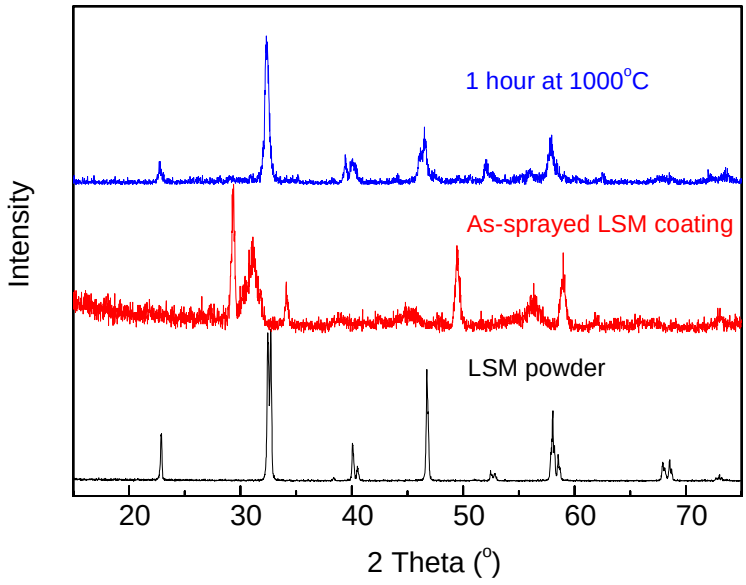

Figure 9: XRD patterns of the as-sprayed and heat-treated LSM coatings as well as the feedstock powders.

Figure 9 shows the XRD patterns of the APS as-sprayed and heat-treated LSM coatings in comparison with the starting powder. XRD pattern indicated that the powder consisted of well-crystallized perovskite LSM. In the as-sprayed coating, the LSM perovskite phase was very weak. As well known, a thermal sprayed coating is generally deposited through the rapid splat cooling process. The high cooling rate over 10^5 K/s usually results in the formation of metastable phases in the as-sprayed coating [6]. The broadening of the XRD peaks of the perovskite LSM phase implies that the fine crystalline grains and in-flight decomposition existed in the as-sprayed LSM coating.

After a heat treatment at 1000^{o}C for 1hour, the LSM perovskite phase became more pronounced due to the recrystallization. The broadening of the perovskite peaks of the heat-treated LSM coating implies that the fine crystalline grains were presented in the in the heat-treated coating.

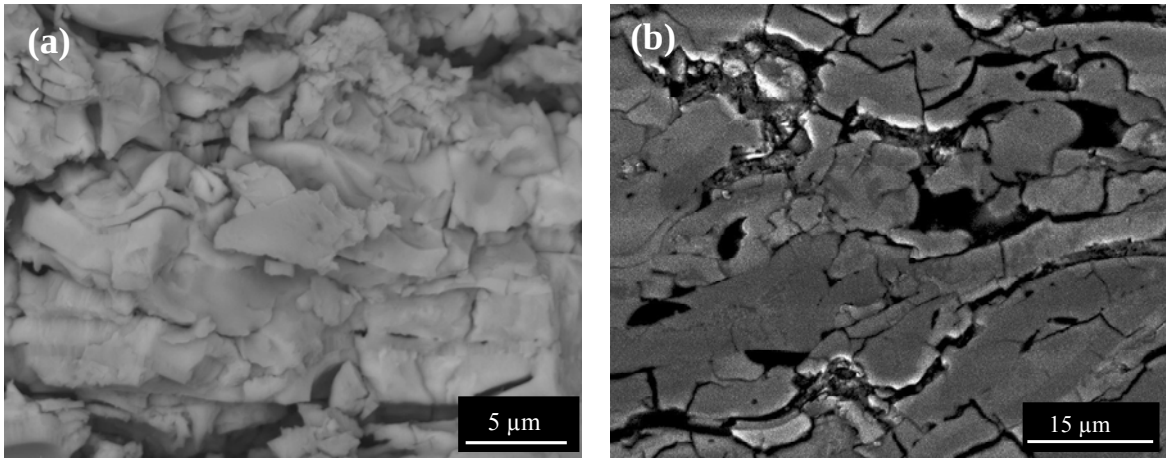

Figure 10: Fractured and polished cross-sectional surface of as-sprayed LSM coating.

The examination of the morphology of a fractured coating and polished cross-sectional microstructure clearly showed that a lamellar microstructure was presented in the LSM coating as shown in Figure 10. This fact means that the coating was deposited by sufficiently molten spray particles. It can be observed that there are lamellar interface cracks and vertical cracks in the polished cross section surface, which was the inherent characteristic of APS ceramic coating. The limited porosity in the LSM coating suggested that the cathode should not be too thick. Otherwise, the concentration polarization will occur in the cathode side during SOFC test due to a shortage of oxygen in the TPBs (three-phase boundaries) in cathode side.

5.3 Cell Output Performance

According to the process aforementioned, tubular cermet supported fuel cells were successfully prepared. Figure 11 shows the obtained fuel cells (without cathode layer). After the cathode layer was sprayed, the electrical performance of the cell was tested in a furnace at the temperature range from 800 to 1000°C. Figure 12 shows the scheme of the experimental setup. The impedance of the cell was also measured by the AC impedance spectroscopy. Figure 13 shows the photo of the measuring instrument.

During the test, hydrogen is used as fuel gas while oxygen is used as oxiding gas. The testing gas flow rates were listed in Table 8. The effective testing area of the cell was 3-4 cm^2. The platinum (Pt) threads were attached to the cathode layer and the copper leads were attached to the supported tube outside the furnace to collect current.

Figure 11: Photo of the thermal-sprayed solid oxide fuel cells (after H_2 reduction and without cathode layer).

Table 8: Gas flow rates used for test.

	Flow rate
H_2	0.8 l/min
O_2	0.8 l/min

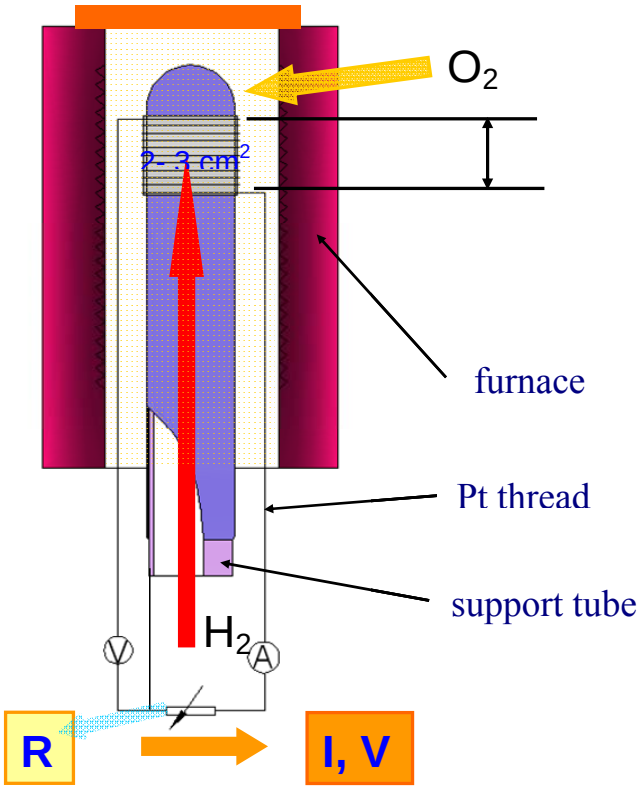

Figure 12: Scheme of the experimental setup of the measuring system.

Figure 13: Photo of the measuring experimental set-up [7].

Figure 14 and Table 9 show the electrical output performance of the cell with 100 µm thick YSZ electrolyte deposited with the medium size powder at the temperature measured from 800 to 1000°C. The results showed that the OCV decreases when the

temperature increases. This could be ascribed to the decrease of ideal standard potential when the temperature increases [8]. As well established:

$$\Delta G = -nFE^{o} \quad (1)$$

Where ΔG is the change in (Gibbs) free energy; E° is the ideal potential of the cell; F is Faraday's constant; n is the number of electrons participating in the reaction. In the condition of standard temperature, ΔG was 235.8 kJ/mol and the E° was 1.229V. When the temperature increases to 1000°C, the value of ΔG reduces to 177.4 kJ/mol, and the E° was reduced to 0.92 V. In the real operation, the OCV was also influenced by the gas pressure besides the temperature, so the real potential (OCV) could be calculated through the Nernst equation:

$$E = E^{o} + \left(RT/2F\right)\ln\left(\frac{P_{H_2} \bullet P_{O_2}^{\ 0.5}}{P_{H_2 o}}\right) \quad (2)$$

The results showed that the cell power density increases with the increase of testing temperature. The maximum power density of 0.20 W/cm^2 was obtained at a current density of 0.43 A/cm^2 at 1000°C, and the maximum power density of 0.05 W/cm^2 was obtained at a current density of 0.08A/cm^2 at 800°C. The maximum output powder density increased about 3 times when the temperature increased from 800 to 1000°C. Moreover, it could be observed that the cell voltage dropped rapidly as the current density increased.

Table 9: OCV of the cell with 100 μm thick APS YSZ electrolyte at different temperatures.

Temperature (°C)	800	850	900	950	1000
OCV (V)	1.02	1.01	1.00	1.00	0.98

Table 10: OCV of the cell with 80 μm thick APS YSZ electrolyte at different temperatures.

Temperature(°C)	800	850	900	950	1000
OCV (V)	1.07	1.06	1.05	1.03	1.03

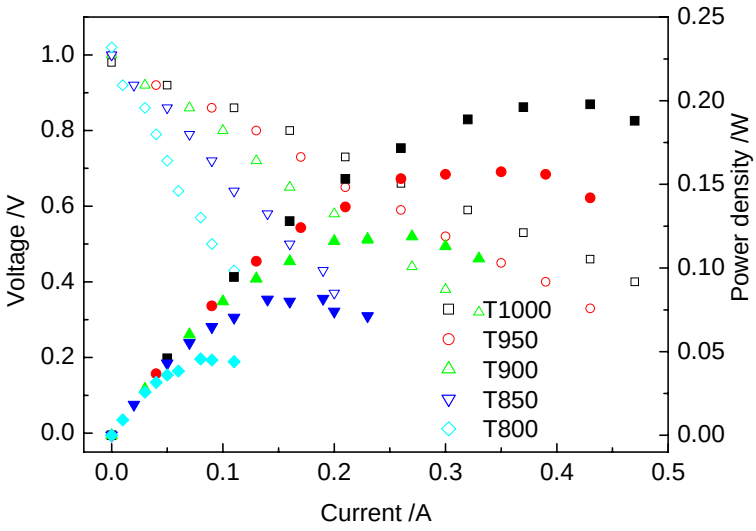

Figure 14: Power density of the cell with 100 µm thick APS YSZ electrolyte.

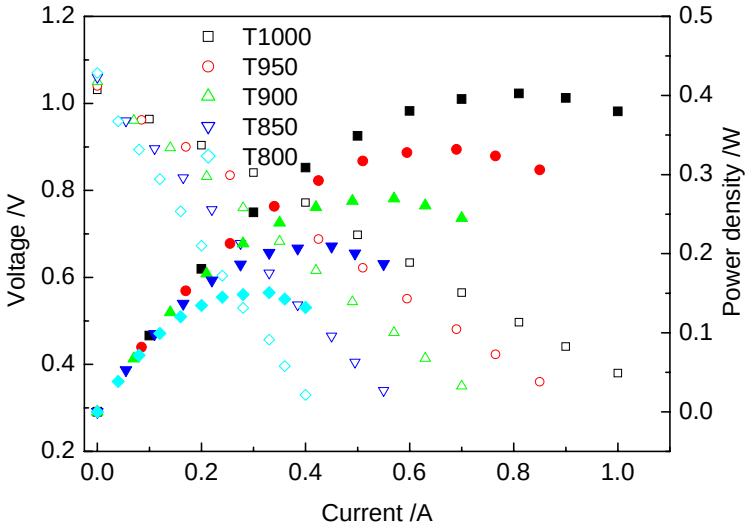

Figure 15: Power density of the cell with 80 µm thick APS YSZ electrolyte.

Figure 15 and Table 10 show the electrical output performance of the fuel cell with 80 µm thick YSZ electrolyte deposited with the small size powder at a temperature from 800 to 1000°C. The results of the OCV and the power density showed the same tendency when temperature increases as the cell with 100 µm thick YSZ electrolyte. However, the improvement of the OCV and power density could be clearly observed when the thin and dense coating was used. The OCV reaches 1.03V at 1000°C and the power density was

0.40 W/cm^2 at 1000°C, which is significantly improved compared to the cell with 100 μm YSZ cell.

Table 11: OCV of the cell with 80 μm thick LPPS YSZ electrolyte at different temperatures.

Temperature (°C)	600°C	700°C	800°C
Before densification (V)	0.90	0.88	0.85
After densification(V)	1.10	1.09	1.08

Table 11 shows the OCV of the cell with 80 μm thick LPPS YSZ electrolyte before and after the 20 times densification. Compared to the results in Table 6, it could be found that the OCV of the as-sprayed cell with LPPS electrolyte was higher than that of cell with APS electrolyte. For example, the OCV of the as-sprayed cell with APS electrolyte was 0.84V and the value of cell with LPPS electrolyte was 0.90V at 600°C. However, the OCV values in Table 10 indicated that the LPPS YSZ electrolyte was not sufficiently dense to be directly used for SOFC operation.

Although LPPS has been used to deposit the as-sprayed YSZ electrolyte for SOFC operation in the literature for a long time and many good results were obtained [9], LPPS electrolyte could not be directly used for SOFC operation in the present study. The reason maybe due to the fact that the particle velocity was not high enough to produce enough dense YSZ coating or the pre-heated temperature of the pre-deposited tube was not high enough in the present study.

The as-sprayed cell with LPPS YSZ electrolyte was also post treated by 20 times densification process. Figure 16 shows the power density of the cell with 80 μm thick LPPS YSZ electrolyte after 20 time densification process. The maximum power density of 0.42 W/cm^2 was obtained at a current density of 0.83 A/cm^2 at 1000°C. After densification process, the power density of the cell with LPPS electrolyte was only a little higher than that of cell with the APS electrolyte. Some further works still need to be carried out in the future to improve the performance of the cell with LPPS YSZ electrolyte and to get high performance cell even without post densification process.

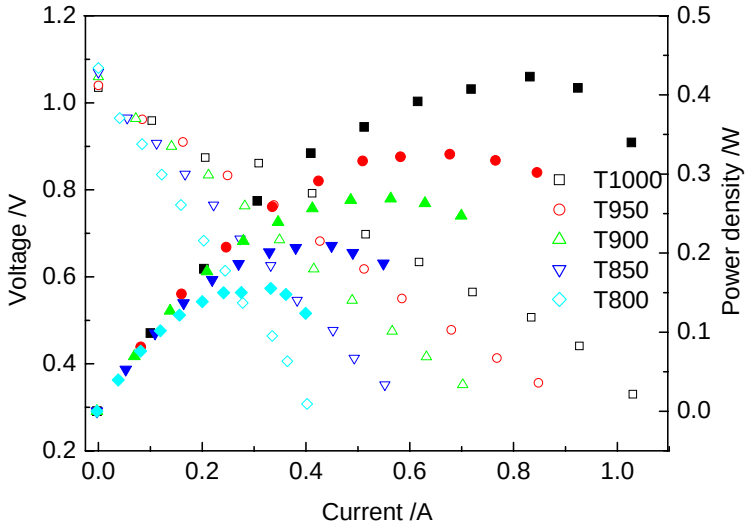

Figure 16: Power density of the cell with 80 μm thick LPPS YSZ electrolyte.

Figure 17 shows AC impedance spectroscopy of the cell (with 80 μm YSZ) at different temperatures. It could be found that the impedance of the cell reduces rapidly when temperature increases. The resistance of the cell was 2.7 Ω at 800°C and 0.7 Ω at 1000°C. As well known, all the cell components were electronically conductive materials except ironically conductive YSZ electrolyte. The conductivity of the electrical conductor decreases with the increase of temperature whereas the conductivity of ionic conductor increases with the temperature. Therefore, the reduction of the resistance should be ascribed to the elevation of ionic conductivity (reduction of resistance) of the YSZ electrolyte. This result indicates that the resistance of the YSZ electrolyte was still a bottle-neck to further improve the performance of the cell in future study.

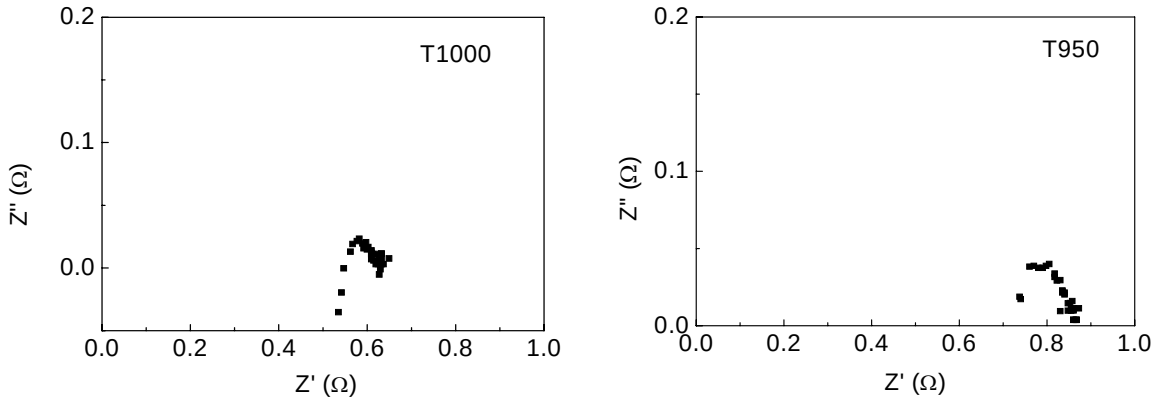

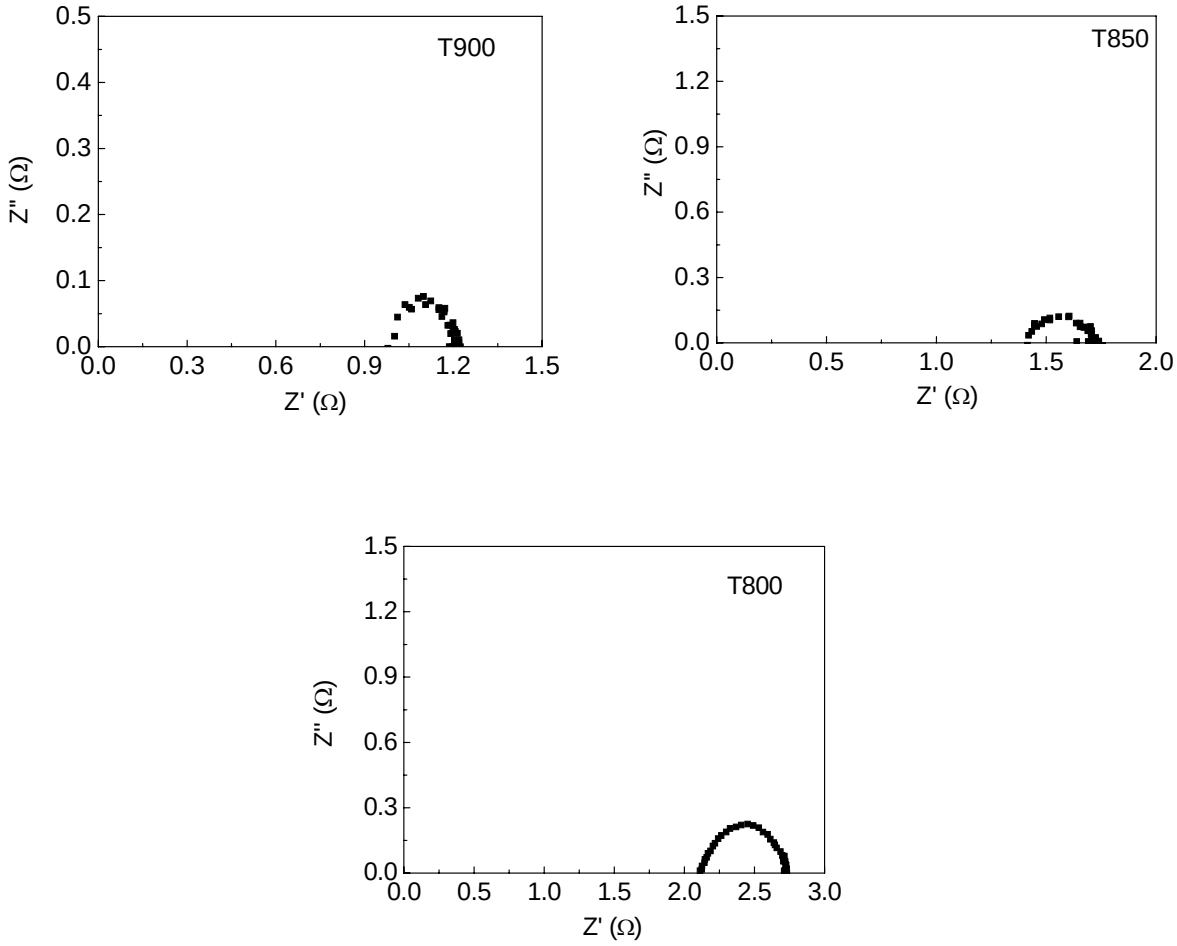

Figure 17: AC Impedance Spectroscopy of the cell (80μm YSZ) at different temperatures.

5.4 Conclusion

In this chapter, tubular solid oxide fuel cells were prepared by the integrated thermal spray process. The output circuit voltage and power density of the cells were measured from 800 to 1000°C. The work in this chapter could be concluded as follows:

(1) Ni-Al_2O_3 porous cermet substrate supported tube could be deposited by flame spraying. Ni-YSZ/YSZ/LSM cells were prepared successfully by plasma spraying on the cermet substrate supported tube.

(2) The electrolyte in the as-sprayed cells was post treated by a densification process to get sufficient gas-tightness. The results showed that the OCV of cell was obviously

improved after densification.

(3) The OCV and maximum power density showed that the performance was significantly influenced by the microstructure of YSZ electrolyte. The maximum cell power density was obviously improved when a thin and dense electrolyte was used.

(4) The LPPS process was also used to deposit YSZ electrolyte for SOFC cell. Although LPPS has been used to fabricate electrolyte for SOFC operation, there is no significant advantage found compared to APS electrolyte in the present study. The OCV results showed that the LPPS as-sprayed electrolyte was not sufficiently gas-tightness for SOFC operation.

5.5 References

[1] S.C. Singhal, Solid oxide fuel cells for stationary, mobile, and military applications, *Solid State Ionics*, **152-153** (2002), p. 405-410.

[2] S.C. Singhal, Advances in solid oxide fuel cell technology, *Solid State Ionics*, **135**(1-4) (2000), p. 305-313.

[3]. X.-J. Ning, Study on the fabrication of zirconia based electrolyte for SOFC by atmospheric plasma spraying, Ph.D. Thesis, Xi'an Jiaotong University, 2005 (in Chinese).

[4] C.-J. Li, X.-J. Ning, C.-X. Li, Effect of densification processes on the properties of plasma-sprayed YSZ electrolyte coatings for solid oxide fuel cells, *Surf. Coat. Technol.*, **190** (2005), p. 60-64.

[5] X.-J. Ning, Cheng-Xin Li, Chang-Jiu Li and Guan-Jun Yang, Modification of microstructure and electrical conductivity of plasma-sprayed YSZ deposit through post-densification process, *Mater. Sci. Eng. A*, **428**(1-2)(2006), p. 98-105.

[6] R. McPherson, The Enthalpy of Formation of Aluminium Titanate, *J. Mater. Sci.*, **8**(1973) p 851-858.

[7] C. -X. Li, Ph.D. Thesis, Study on the fabrication of cermet supported tubular SOFC by thermal spray and effect of cell component microstructure on its performance, Xi'an Jiaotong University, 2005 (in Chinese).

[8] Mark C. Williams, Fuel Cell Handbook (Sixth Edition), Nov. 2002.

[9] R. Henne, Solid oxide fuel cells: a challenge for plasma deposition processes, *J. Therm. Spray Technol.* **16**(3) (2007), p. 381-483.

General Conclusions and Perspectives

The main part of this thesis is organized in four chapters dealing with parameter optimization of the plasma spraying YSZ (8 mol% yttria stabilized zirconia) process (chapter 2), ionic conductivity of diverse plasma-sprayed YSZ coatings as well as the enhancement of ionic conductivity by microwave sintering (chapter 3), gas tightness and gas permeation behavior through plasma-sprayed YSZ coating (chapter 4), fabrication process and electrical performance of tubular cermet support Ni-YSZ/YSZ/LSM solid oxide fuel cell (chapter 5). These four chapters aim to design and investigate the microstructure and performance of the plasma-sprayed YSZ coating and the prepared solid oxide fuel cell. Hence, in this general conclusion, we will summarize and evaluate the four aspects, optimization of spraying parameters, coating ionic conductivity, coating gas permeation and cell performance.

(1) The plasma spraying parameters for YSZ electrolyte coating were optimized via applying DPV2000 diagnostics analyzer. The parameters of powder size, spraying distance, hydrogen and helium flow rates on the velocity and surface temperature of in-flight YSZ particles were studied. The effect of particle velocity and surface temperature on coating microstructure was observed.

The results showed that the particle velocity and surface temperature were strongly influenced by the powder size. Small size powder was easily to get a high particle temperature and a high particle velocity. The spraying distance (in the range of 80-110mm) has little effect on the particle surface temperature. However, a significant influence on particle velocity was observed when the spraying distance changed. 100mm was an

optimized spraying distance in the present study. The particle surface temperature increases when the H_2 flow rate was enhanced when the small size powder was used as feedstock. The results also showed that the increase of H_2 flow rate has a slightly positive effect on the particle velocity. As concerning to He flow rate, the particle velocity increased with the increases in He flow rate. However, the highest particle velocity obtained in the present study is still lower than that in the LPPS process. Due to He opposite effect of plasma's enthalpy increase and particle's dwelling time reduce, the particle temperature only slightly increases.

The microstructure of YSZ coatings showed that the increase of both particle velocity and particle temperature has positive effect on coating microstructure. High velocity and high temperature of YSZ particle were essential to obtain dense YSZ electrolyte coating. Observing from the coating surface and the fractal cross-sectional surface, the low pressure plasma-sprayed YSZ coating showed less vertical cracks and less width of non-bonded interface. However, no significant difference on LPPS (low pressure plasma spraying) coating porosity was found compared to the APS (atmospheric plasma spraying) coating.

(2) For APS yttria stabilized zirconia electrolytes, the ionic conductivity was determined by material composition and coating microstructure. The lamellar features of plasma-sprayed coating with limited lamellar bonding interface and vertical cracks led to the anisotropy of coating properties and the reduction of ionic conductivity. The ionic conductivity of all the as-sprayed YSZ coatings along the perpendicular direction was about one-fourth to the corresponding bulk electrolyte. The ionic conductivity in the parallel direction was about twice higher than that in perpendicular direction, which can be attributed to lamellar microstructural feature of plasma-sprayed ceramic coatings.

The examination of the temperature dependence of ionic conductivity of YSZ electrolyte yielded non-linear Arrhenius behavior. The two frequently used models, intragrain-intergrain conductivity and the dissociation-migration energy model, were examined for explaining the non-linear characteristic. On the basis of the data reported in literature, the limitation of intragrain-intergrain conductivity model was evidenced. It is more reasonable to employ the dissociation-migration energy model to explain the temperature dependence of the obtained ionic conductivity of APS YSZ electrolyte.

The feasibility of MW sintering on plasma-sprayed YSZ coatings, with $BaTiO_3$ as MW susceptor, was investigated. The plasma-sprayed pure YSZ coating can only be heated to less than 900°C in the MW cavity due to its low dielectric loss factor, whereas the $BaTiO_3$-YSZ composite coating could be easily heated to 1450°C. For the $BaTiO_3$-YSZ composite coating, the $BaTiO_3$ particles were regarded as distributed heat sources in YSZ matrix. The lamellar structure of the as-sprayed $BaTiO_3$-YSZ composite coatings is modified to equiax crystal in MW-sintered coatings. $BaTiO_3$ transformed to $Ba(Ti_{1-x}Zr_x)O_3$ during MW sintering process and assembled to the interface after MW sintering. Ionic conductivity of MW-sintered composite coatings was about one time higher than that of as-sprayed coatings. Compared with ionic conductivity of the pure YSZ coating, the MW-sintered 5wt.%$BaTiO_3$-YSZ coating presented a 60% higher conductivity.

(3) The gas specific permeability of APS YSZ coatings was measured with a home-made instrument. The effect of particle temperature (H_2 flow rate), velocity (He flow rate) and particle size on the gas specific permeability of APS YSZ coatings was studied. The gas permeation behavior through APS YSZ coatings were investigated for coatings with diverse microstructures.

The results showed that the small size powder was favourable to deposited YSZ coatings with high gas tightness. The gas specific permeability changed from 4.80×10^{-17} to 1.93×10^{-16} m^2 for the coatings deposited with different size powder. When H_2 flow rate decreased, the particle temperature was also decreased. The coating deposited with low H_2 flow rate shows more porosity, especially the global pores than that sprayed with high H_2 flow rate. Although the coating porosity was an indication of coating gas permeability, it was found that there is no direct relationship between the gas permeability and porosity. The dimension of vertical cracks and non-bonded interface determines the coating gas permeability. The particle velocity has a positive effect on coating permeability. Adding helium in the plasma gas increases the particle velocity and improves the coating gas-tightness. When the helium changed from 0 to 50 l/min, the gas permeability of YSZ coatings deposited with medium powder was reduced from 0.81×10^{-16} to 0.43×10^{-16} m^2, correspondingly.

The same gas permeation behaviour- transition behaviour was exhibited for all YSZ coatings. However, the proportion of viscous flow and Knudsen flow was different

depending on coating microstructure. The results showed that the effect of viscous flow will become low and the effect of Knudsen flow will be significant for plasma-sprayed YSZ coating when the size of sprayed powder size decreases.

(4) In the last part of this thesis, tubular solid oxide fuel cells were prepared by the integrated thermal spraying process. Ni-Al_2O_3 porous cermet substrate supported tube could be deposited by flame spraying. Ni-YSZ/YSZ/LSM cells were prepared successfully by APS on the cermet substrate supported tube. The as-sprayed cells were post-treated by an electrolyte densification process to get sufficient gas-tightness. The results showed that the OCV (output circuit voltage) of cell was obviously improved after densification.

The output circuit voltage and power density of the cells were measured from 800 to 1000°C. The OCV and maximum power density showed that the performance was significantly improved when the thin and dense YSZ electrolyte was used. The maximum power density of cell was about 0.4 W/cm^2 when the thin and dense electrolyte was used.

The LPPS process was also used to deposit YSZ coating as SOFC (solid oxide fuel cell) electrolyte layer. Although LPPS has been used to fabricate electrolyte for SOFC operation in literature, there is no significant advantage found compared to APS electrolyte in the present study. The OCV results showed that the LPPS as-sprayed electrolyte was not sufficiently gas-tightness for SOFC operation.

At the end, the results have illustrated that it is, in principle, possible to obtain high performance YSZ electrolyte by atmospheric plasma spraying. Whereas almost all the APS YSZ electrolyte layers was not totally gas-tightness, a post-spray densification was indispensable for SOFC operation in this study. The results showed that the particle characteristics, especially particle velocity should be further enhanced to decrease the coating gas permeability. This could be conducted when an advanced commercial plasma spraying system is available in the laboratory. In the other part, a better YSZ electrolyte layer also could be prepared by a low pressure plasma spraying system which was already installed in the laboratory, although the deposition efficiency and the deposition velocity is still very low at present compared to the conventional atmospheric plasma spraying.

The aforementioned experiments in this thesis are an excellent starting point for the

following further investigations:

(1) Some new electrolyte materials with high ionic conductivity should be adopted to decrease the electrolyte resistance and to improve the cell performance.

(2) Provided using an advanced spraying system and ensuring the coating gas-tightness, the thickness of the electrolyte should be further lowered to decrease the electrolyte resistance.

(2) The gas permeation through plasma-sprayed YSZ electrolyte in high temperature should be investigated. In SOFC operational temperature, gas viscosity, gas mean free path and Knudsen number will change and will have a strong influence on the gas-tightness of electrolyte layer.

Abstract

Fuel cells have been widely investigated as an environmentally-friendly alternative to conventional fossil fuels. By oxidizing hydrogen, the only direct by-product of their energy generation is water, which means they could significantly reduce pollution and man-made greenhouse gases. SOFC (solid oxide fuel cell) is one promising type of the fuel cell, which can eliminate corrosion or leakage problems common to the other liquid electrolyte fuel cells. SOFC operating temperatures are typically in the range of 800-1000°C, which leads to several advantages, such as internal reforming, the use of carbon monoxide as a fuel, the possibility of realizing combined heat and power plant solutions. At present, the commercialization efforts on SOFC systems are oriented to the cost reduction effort, in order to compete more effectively with other traditional power generating methods. In such a context, electrolyte deposition attracts particular attention. Plasma spraying process is a promising technique, providing such advantages as high deposition rate and easy masking for deposition of patterned structures, compared with other film formation processes.
The objective of this work is thus to optimize the plasma-sprayed electrolyte coating and investigate the coating electrical and gas-tight performance as well as the finally tubular SOFC fabrication and performance test. With regard to this aim, four following aspects of work have been carried out. Firstly, the optimization of spraying parameters and coating microstructure was done via measuring in-flight particle features. Secondly, the ionic conductivity of YSZ coatings was measured and the temperature dependence of ionic conductivity of YSZ coatings was discussed. In this part, the modification of microstructure and ionic conductivity of plasma-sprayed coatings by microwave sintering was also investigated. Thirdly, the gas tightness of YSZ coatings was evaluated via measuring coating gas permeability and the gas permeation behavior through YSZ coatings was examined based on the gas permeation theory in porous materials. Finally, the tubular Ni-YSZ/YSZ/LSM ($La_{0.8}Sr_{0.2}MnO_3$) solid oxide fuel cells are fabricated by the integrated thermal spray process and the output circuit voltage and power density of the cells are performed.

Keywords : Plasma spraying, coating, Particle temperature, Particle velocity, Yttria stabilized zirconia, electrolyte, Ionic conductivity, Gas permeability, Solid oxide fuel cell.

Résumé

Les piles à combustible ont été largement étudiées comme une alternative aux combustibles fossiles traditionnels plus respectueuses de l'environnement. Le seul sous-produit direct de l'oxydation de l'hydrogène pour la production d'énergie est l'eau, ce qui signifie qu'elles pourraient réduire sensiblement la pollution et les produits de gaz à effet de serre. Les SOFCs (piles à combustible à oxyde solide) sont un type de pile à combustible prometteur, qui peut éliminer les problèmes de corrosion ou de fuite communs aux autres piles à combustible à électrolyte liquide. Les températures de fonctionnement des SOFCs sont typiquement de l'ordre de 800-1000°C, pouvant conduire à plusieurs avantages, tels le réformage interne, l'utilisation du monoxyde de carbone comme combustible et la possibilité de réaliser la production combinée de chaleur et d'électricité. Depuis plusieurs années, les efforts de commercialisation sur les systèmes SOFC sont orientés vers la recherche de la réduction des coûts, afin de rivaliser plus efficacement avec d'autres méthodes de production d'énergie traditionnelles. Dans un tel contexte, les dépôts électrolytiques attire particulièrement l'attention. La projection plasma est un procédé prometteur, offrant des avantages tels que des rendements élevés des dépôts et la possibilité de masquer les dépôts.
L'objectif de ces travaux est donc d'optimiser la projection plasma de revêtements électrolytiques, d'étudier les performances électriques et l'étanchéité aux gaz des revêtements. Dans ce contexte, quatre aspects ont été abordés. Dans un premier temps, l'optimisation des paramètres de la projection et la microstructure de revêtements a été réalisée par la mesure de particules en vol. D'autre part, la conductivité ionique des revêtements YSZ en fonction de la température a été examinée. La modification de la microstructure et de la conductivité ionique de revêtements projetés par frittage micro-ondes a également été étudiée. Enfin, l'étanchéité des revêtements YSZ ainsi que les mécanismes de perméation des gaz ont été étudiés par la mesure de la perméabilité . Finalement, les piles à combustible à oxyde solide tubulaires Ni-YSZ/YSZ/ LSM($La_{0.8}Sr_{0.2}MnO_3$) ont été fabriqués grâce au procédé de projection thermique intégrée. En outre, les mesures de tension du circuit de sortie et de la densité de puissance des piles ont été effectuées.

Mots clés : Projection plasma; revêtement ; Température de particule, Vitesse de particule, Zircone stabilisée à l'yttrium, Electrolyte, Conductivité ionique, Perméabilité de gaz, Pile à combustible à oxyde solide.